8-2014

Fabrication and Characterization of Cu-Co Alloy Nanoparticles via Pulsed Laser Dewetting

Shaofang Fu
University of Tennessee - Knoxville, sfu1@utk.edu

To the Graduate Council:

I am submitting herewith a thesis written by Shaofang Fu entitled "Fabrication and Characterization of Cu-Co Alloy Nanoparticles via Pulsed Laser Dewetting." I have examined the final electronic copy of this thesis for form and content and recommend that it be accepted in partial fulfillment of the requirements for the degree of Master of Science, with a major in Materials Science and Engineering.

Philip D. Rack, Major Professor

We have read this thesis and recommend its acceptance:

David C. Joy, Thomas T. Meek

Accepted for the Council:
Carolyn R. Hodges

Vice Provost and Dean of the Graduate School

(Original signatures are on file with official student records.)

Fabrication and Characterization of Cu-Co Alloy Nanoparticles via Pulsed Laser Dewetting

A Thesis Presented for the
Master of Science
Degree
The University of Tennessee, Knoxville

Shaofang Fu
August 2014

DEDICATION

Dedicated to my dear parents and fiancé

ACKNOWLEDGEMENTS

First, I would like to thank Dr. Philip Rack for his insight, patience, and guidance over my work. I would also like to thank all my families and friends for their consistent help and support. Finally, I really appreciate Dr. David Joy and Dr. Thomas Meek to serve on my thesis committee.

ABSTRACT

The fabrication and characterization of Cu[Copper]-Co[Cobalt] alloy nanoparticles are addressed in this thesis. First, Cu-Co alloy thin films with total thickness of ~10 nm [nanometer] were deposited on both 100 nm SiO_2 [silicon dioxide] coated silicon wafers and quartz substrates using RF magnetron sputtering system. Three structures were studied in this work: (1) ~10 nm co-sputtered Cu-Co alloy thin film. (2) ~5 nm (at center) Cu thin film covered by ~5 nm (at center) Co thin film. (3) ~5 nm (at center) Co thin film covered by ~5 nm (at center) Cu thin film. In addition, ~10 nm pure Cu and Co thin films were also prepared on the three substrates described above for comparison with the alloy. EDS, Filmetrics F20-UV thin film analyzer, and Cary 5000 (Varian Inc.) were used for thin films composition and optical properties analysis. After that, thin films were irradiated in air by Nd:YAG [neodymium-doped yttrium aluminum garnet] laser to form Cu-Co particles. The particles morphology was then characterized by SEM [Scanning Electron Microscope]. Composition and optical properties were also studies on particles.

The analysis results demonstrate that the dewetting evolution is tunable by adjusting the alloy composition or thin film structure. Particles size distribution is also affected by composition and structure. The optical measurement reveals that particles at Cu-rich edge on Co top Cu bottom sample show an obvious Surface Plasmon Resonance phenomenon.

TABLE OF CONTENTS

LIST OF TABLES

LIST OF FIGURES

CHAPTER 1 INTRODUCTION

1.1 Self-assembly of nanoparticles

Nano-patterns with characteristic length scales have become an active area of research. For example, pattern formation by ion irradiation has been used to modify surface topography. Rippling under ion irradiation is due to an instability resulting from the competition between ion erosion and smoothening caused by surface diffusion [1]. Another example for thin film pattern formation is hydrodynamic instabilities such as spinodal dewetting [2-8]. In this case, the nano-patterns have characteristic length scales and timescales which depend on the thermophysical material properties such as melting temperature, surface tension, fluid velocity and intermolecular forces such as van der Waals forces. Under certain conditions, thin films will break up into holes resulting from spontaneous film thickness fluctuations. These holes then grow and the rims ahead of the holes eventually merge to form cellular-like structures. The resulting rims/filamets are unstable and decay into droplets [9]. For instance, Figure 1.1 shows a typical dewetting process of co-sputtered Cu-Co alloy.

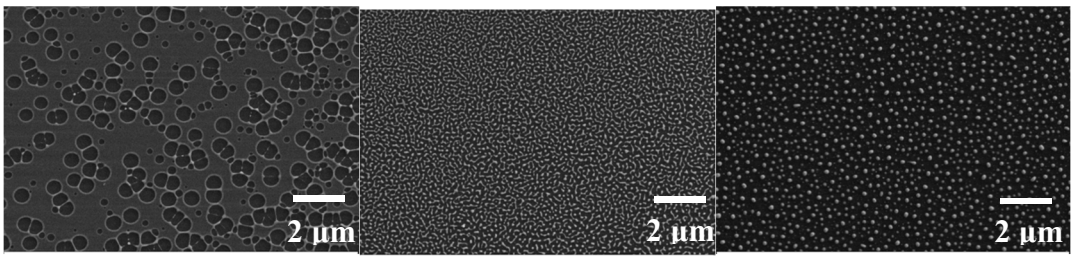

Figure 1.1 Dewetting evolution of 10 nm thick Cu-Co alloy thin film on SiO_2/Si substrate with nanosecond laser irradiation (increasing liquid lifetime from left to right)

1.1.1 Spinodal theory

There are two leading theories which explain the classical dewetting instability [10-12]. One is called spinodal theory. More than forty years ago, Anton Vrij hypothesized that extremely thin liquid films are unstable via the amplification of surface waves [9]. This instability in thin films can be interpreted as a competition between the stabilizing effect of interfacial tension and the attractive intermolecular forces between the film-substrate and film-vacuum interfaces mediated by the film materials. The intermolecular forces, van der Waals forces, play an important role in this theory. The van der Waals forces are weak in liquids compared with other intermolecular forces. Additionally, there are always small perturbations or thermal vibrations in liquids which can develop as spinodal wave. The amplitude of the disturbance grows with time and leads to dewetting if the growth in the amplitude

lowers the energy of the system. Otherwise, the perturbation is damped and the film remains continuous. For very thin films (less than 100nm), van der Waals forces become significant and overcome the interfacial tension. Under such conditions, film thickness fluctuations are spontaneously amplified and eventually dewet [6, 9, 13, 14]. The computed result [9] of variation in height h(x,t) of the film at different position x and time t are as shown in the Figure 1.2. This diagram clearly indicates the emergence of spines at the early stage of spinodal dewetting.

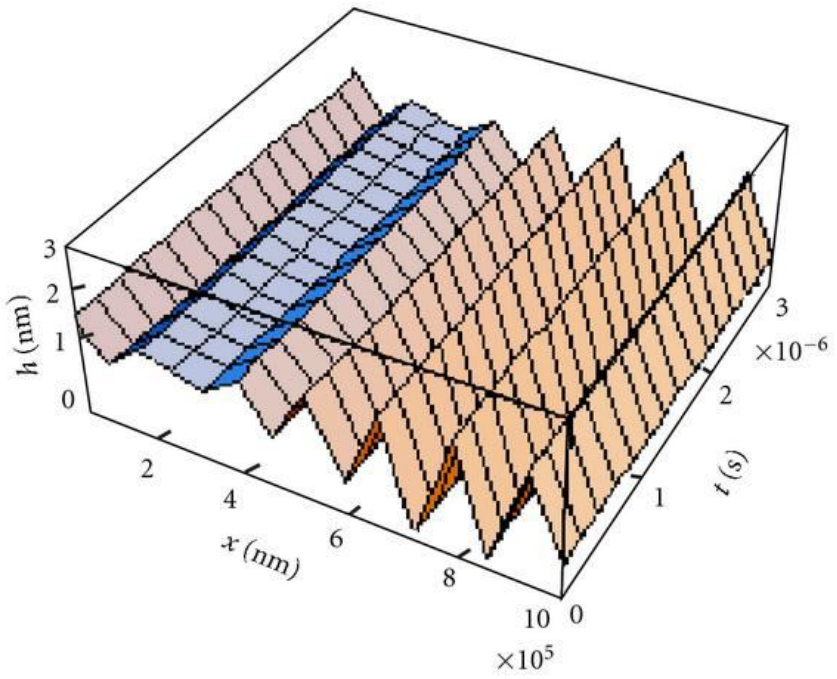

Figure 1.2 A 3D graph representing time evolution of surface waves at early stages of spinodal dewetting
"Singh, S.P., Spinodal Theory: A Common Rupturing Mechanism in Spinodal Dewetting and Surface Directed Phase Separation (Some Technological Aspects: Spatial Correlations and the Significance of Dipole-Quadrupole Interaction in Spinodal Dewetting). Advances in Condensed Matter Physics, 2011."

However, the interfacial tension cannot allow intermolecular forces to prevail the dewetting process when the films are too thick. Another mechanism that can lead to dewetting is nucleation. Both homogeneous and heterogeneous nucleation can be operative. For homogeneous nucleation and growth, holes appear spontaneously at random locations and times on the surface, and thus there is no characteristic length scale. Heterogeneous nucleation occurs much more often compared to homogeneous nucleation. It forms at preferential sites such as phase boundaries or impurities like dust and requires less energy than homogeneous nucleation [15].

1.1.2 Characteristic wavelength and timescale

The length and time scale of dewetting patterns due to spinodal instability can be explained by lubrication analysis. Lubrication theory provides a relationship between mass flux and the effective pressure gradient resulting from perturbations and disjoining pressure due to intermolecular forces such as van der Waals forces. For a thin film on substrate, the disjoining pressure [16-19] is:

$$\Pi = \frac{A}{6\pi h'^3} \tag{1.1}$$

Here, h is the thin film thickness. And A is the Hamaker constant which can be defined for a van der Waals body-body interaction:

$$A = \pi^2 \times C \times \rho_1 \times \rho_2 \tag{1.2}$$

Where ρ1,ρ2 are the number of atoms per unit volume in two interacting bodies and C is the coefficient in the particle-particle pair interaction. The Hamaker constant is used to determine the interaction parameter C from the van der Waals pair potential which is expressed as $\omega(r) = -C/r^6$ for two atoms with interval distance of r. According to the above expressions, a characteristic wavelength Λ can be evaluated as a function of film thickness:

$$\Lambda(h) = \sqrt{\frac{16\pi^3\gamma}{A}}h^2 \tag{1.3}$$

whereγis the surface tension of the metal. Similarly, from the linear thin film hydrodynamic theory, the dewetting instability time scale τ_D associated with the growth of perturbations with wavelength Λ is:

$$\tau_D(h) = \frac{96\pi^2\gamma\eta}{A^2}h^5 \tag{1.4}$$

where ηis the viscosity of liquid materials at their melting points [1]. After the formation of holes, the thin films will retract from the hole-center with a velocity (ignoring viscous loss) known as the Taylor-Culick velocity:

$$v = \sqrt{\frac{2\gamma}{\rho h}} \tag{1.5}$$

where γ is the liquid thin film surface tension, ρ is the liquid density, h is the thickness of thin film.

1.1.3 Rayleigh-Plateau theory

The Rayleigh-Plateau phenomenon is easily observed in daily life. Examples of this instability include uniform water beads forming on a spider web during the night, water dripping from a faucet, and the use of ink-jet printing. Due to surface tension, liquids tend to break up into droplets instead of remaining in cylindrical form [20-26]. The driving force of this process is system energy minimization.

Tiny perturbations exist in the stream no matter how smooth the stream is. Assuming the perturbations are resolved into sinusoidal components, some of them grow with time while others decay with time.

The future shape formation can be explained by Young-Laplace equation:

$$\Delta p = \frac{2\gamma}{R} \tag{1.6}$$

where Δp is the pressure difference across the fluid interface, γ is the surface tension, and R is the radius of curvature. At the trough, the radius of the stream is smaller than that at the peak. Hence the pressure at the trough is higher. We can expect that the higher pressure in the trough would squeeze liquid into the lower pressure region in the peak. Then the wave growing in amplitude over time is obtained. Furthermore, it is found that the component that grows the fastest is the one whose wave number satisfies the equation:

$$kR \cong 0.697 \tag{1.7}$$

Here, k is the wave vector, and R is the radius of curvature.

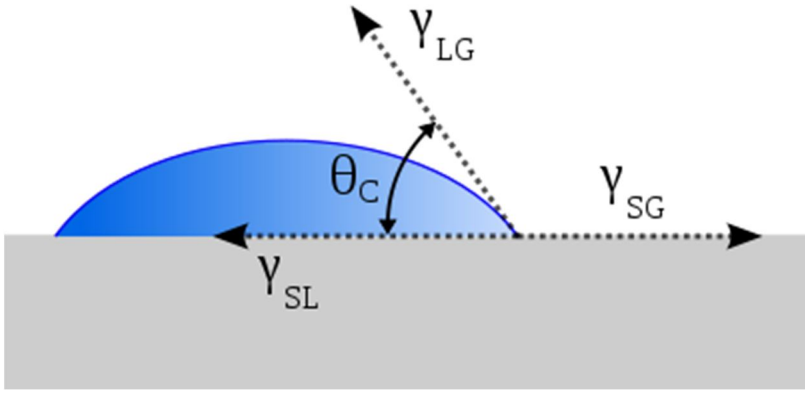

Figure 1.3 Interfacial tensions working on a macroscopic drop at a substrate. γ_{LG}, γ_{SL}, γ_{SG} are interfacial tensions between liquid-gas medium, solid-liquid medium and solid-gas medium. θ_C is contact angle.
"From Wikipedia"

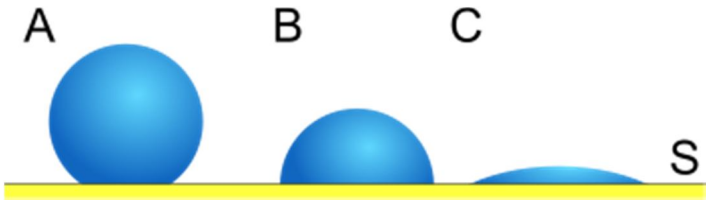

Figure 1.4 Shows different contact angles. A has a large contact angle while C has a small contact angle.
"From Wikipedia"

When droplets form, there is a contact angle depending on the wettability of the liquid. Figure 1.3 shows interfacial tensions between different medium. In this case, the equilibrium contact angle can be expressed as:

$$\gamma_{SG} = \gamma_{SL} + \gamma_{LG}\cos\theta_C \tag{1.8}$$

Figure 1.4 schematically show the different contact angle which depends on the wettability of liquid.

1.2 Cu-Co system

Synthesis, characterization and property evaluation of core/shell nanostructures has attracted profound interest because of their potential applications in various fields such as magnetism, optics and catalysis [27]. The Cu-Co system, combines a strong magnet (Co) with a good conductor (Cu) in an immiscible system, is of special interest due to plethora of applications [28-37]. So far, Co-Cu alloys have been mainly used in recording media and sensors owning to their giant magneto resistance (GMR) effects [38-48]. The microstructural features in the Cu-Co alloy system controlling the magnetization and GMR effect are expected to be grain size, distribution shape, and the volume fraction of magnetic phase embedded in the non-magnetic matrix [30]. Cu-Co granular materials are also employed as catalysts in chemical applications because of the large surface to volume ratio which can improve the catalytic efficiency [49, 50].

Furthermore, the physical and chemical properties of Cu-Co alloys depend on the structure of core, shell and the interfacial interactions which are tunable by simply controlling the core-shell structures of different size and composition [51, 52]. Nowadays, various methods have been used to synthesize the Cu-Co nanostructures such as chemical synthesis, sputtering, solidification, lithography-based nano-structuring and mechanical alloying [27, 53-59]. Among these processes, chemical synthesis which includes sonochemical routes, polyol process and transmetallation reactions, are commonly used because it allows controlling the composition of Cu/Co and the size of both core and shell precisely [27, 56, 60]. Another relatively simple method of forming nano-structures on a surface is based on

the dewetting of thin films on an inert substrate. As a self-assembly and self-organizing technique, the spontaneous dewetting of thin films under thermal treatment has been widely investigated [61]. This process, with an initial smooth film of precise thickness, can fabricate patterns with well-defined morphology and length scales [54]. This is a promising approach to fabricate nano-structures with tunable size and compositions.

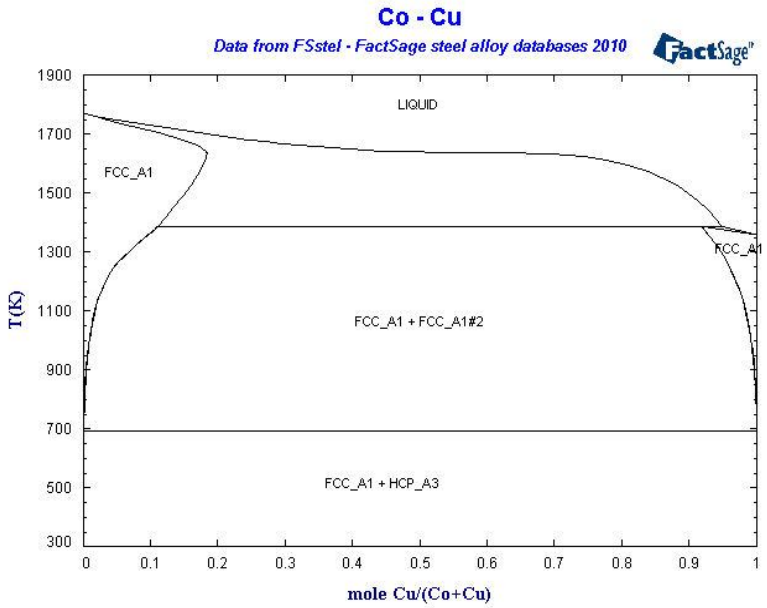

Figure 1.5 Phase diagram of Cu-Co binary system
"From FactSage database"

1.2.1 Cu-Co phase diagram and diffusion

According to the Cu-Co equilibrium phase diagram [62-66], it can be seen that Cu and Co have limited solid solubility and do not form any intermetallic compound. The Cu rich solid solution is face-centered cubic (FCC) while the Co rich solid solution is either FCC (high-temperature) or hexagonal close-packed (HCP) (lower temperature) depending on its heat treatment history [67]. That means Co has a allotropic transformation from a FCC phase to a HCP phase at 422℃ on cooling [66]. Due to the solubility property of Cu-Co system, there is a phase separation during the solidification of liquid alloy.

Diffusion is the mass transport by atomic motion in a solid, liquid or gas. For gas and liquid, the diffusion mechanism is random (Brownian) motion while the movement in solid depends on vacancy or interstitial diffusion.

Fick's First Law relates the diffusive flux to the concentration under the assumption

that diffusion rate is independent of time (steady state). In one spatial dimension, the law is

$$J = -D\frac{\partial C}{\partial x} \tag{1.9}$$

Where J is the diffusion flux, C is the concentration and x is the position, D is the diffusion coefficient or diffusivity, which increases with increasing temperature. And the relationship can be expressed as:

$$D = D_0 \exp\left(-\frac{Q_d}{RT}\right) \tag{1.10}$$

Here D_0 is pre-exponential, Q_d is activation energy, R is gas constant and T is absolute temperature in K.

If the concentration of diffusing species is time dependent (non-steady state), Fick's Second Law is used:

$$\frac{\partial C}{\partial t} = D\frac{\partial^2 C}{\partial x^2} \tag{1.11}$$

The solution of C(x,t) can be obtained using initial and boundary conditions. That is

$$\frac{C(x,t) - C_0}{C_s - C_0} = 1 - \mathrm{erf}\left(\frac{x}{2\sqrt{Dt}}\right) \tag{1.12}$$

Where C(x,t) is the concentration at point x at time t. C_s is the constant surface concentration while C_0 is the concentration at $x = \infty$. And erf(z) is the error function which is equal to

$$\mathrm{erf}(z) = \frac{2}{\sqrt{\pi}}\int_0^z e^{-y^2} dy \tag{1.13}$$

The thin film solution of C(x,t) can be obtained by looking at the case where Δx is very small compared to the diffusion distance x, and the thin film is initially located at x=0:

$$C(x,t) = \frac{N}{\sqrt{4\pi Dt}} e^{-x^2/(4Dt)} \tag{1.14}$$

Where N is the number of "source" atoms per unit area initially placed at x=0.

1.3 Pulsed laser annealing

The spontaneous dewetting of thin films under thermal treatment is a facile method for self-assembly. Among the possible heating sources, nanosecond laser pulses have proved to be important because of their ability to rapidly raise the metal temperature to beyond its melting point and also being able to capture intermediate stages of dewetting due to high quenching rates [61]. It also has a shorter time to anneal the metal films compared with other techniques.

1.3.1 Emission and absorption of light

Laser, which is an acronym for Light Amplification by Stimulated Emission of Radiation, is a device that emits light through a process of optical amplification based on the stimulated emission of electromagnetic radiation. It is distinguished from other light sources by its coherence. One is spatial coherence which allows a laser to be focused to a tight spot. Another one is temporal coherence. This enables applications such as laser pointers by allowing a laser beam to stay narrow over long distances. In this thesis, a Neodymium-doped Yttrium Aluminum Garnet (Nd:YAG) crystal laser with 266nm wavelength is used for thin film annealing.

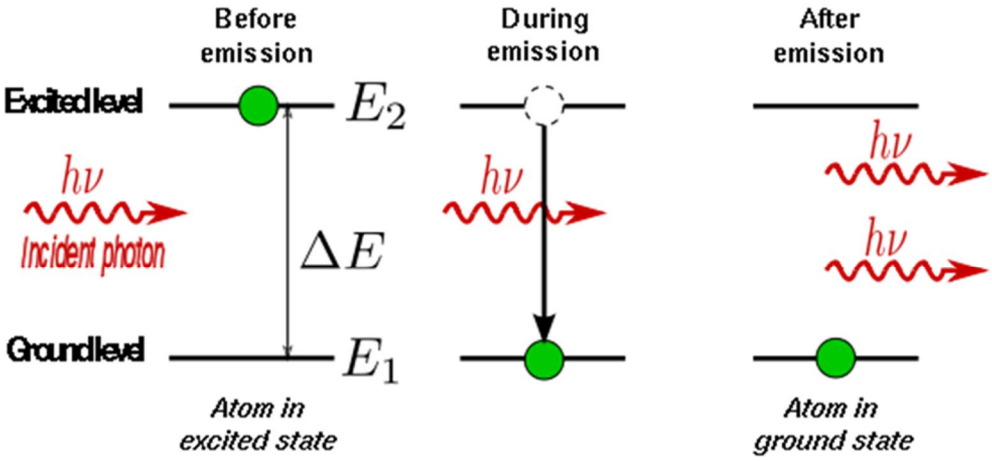

Figure 1.6 Stimulated emission of atom
"From Wikipedia"

The contemporary model of atomic structure describes an electrically neutral system composed of a nucleus with one or more electrons bound to it. Each atom has an array of energy levels: the level with the lowest possible energy is called the ground state, and higher energy levels are called excited states. If an atom is in its ground state, it will stay there until it is excited by external forces.

Movement of electrons from one energy level to another, a transition, happens when the atom either absorbs or emits energy. The transition in either direction can occur as a result of interaction with a photon of light. Consider a transition from a lower level whose energy is E_1 to a higher one with energy E_2. It will only occur if the energy of the incident light higher than the energy difference between levels, i.e.

$$hv = E_2 - E_1 \tag{1.15}$$

where h is Planck's constant, and v is the frequency of the photon. Likewise, when an electron excited to E_2 decays to E_1, it loses energy equal to E_2-E_1. It may decay spontaneously, emitting a photon with energy hv and frequency:

$$v = \frac{E_2 - E_1}{h} \tag{1.16}$$

An electron excited to E_2 can also be stimulated to decay to E_1 by interacting, known as stimulated emission (Figure 1.6), with a photon of frequency v, emitting energy in the form of a pair of photons that are identical to the incident one in phase, frequency and direction.

1.3.2 Population inversion

The net absorption at a given frequency is the difference between the rates of emission and absorption at that frequency. The rate of stimulated emission from E_2 to E_1 is proportional to the population of the upper level (N_2) and the transition probability. Similarly, the rate of excitation from E_1 to E_2 is proportional to the number of atoms in the lower level (N_1) and the transition probability. And the transition probability depends on the flux of the incident wave and the transition cross section. Therefore, the absorption efficiency depends only on the difference between the populations, N_1 and N_2, and the flux of the incident wave.

If the transition scheme is limited to two energy levels, N_2 can never exceed N_1 because each upward transition is matched by one in the opposite direction. Therefore, it is impossible to drive the populations beyond equality. However, if three or more energy levels are employed, additional excitation can create a population inversion where $N_1 > N_2$.

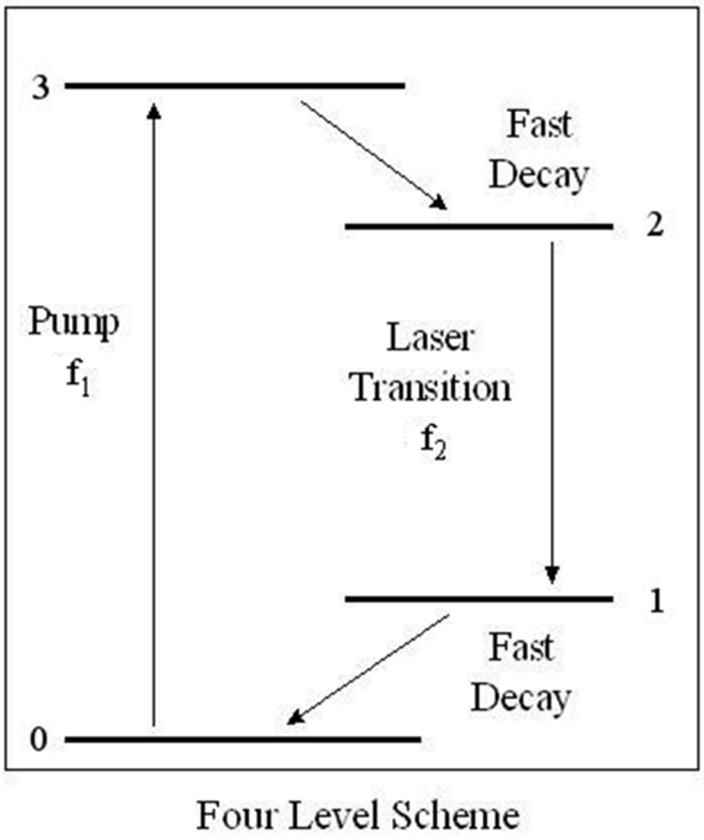

Figure 1.7 A typical four-level transition scheme

For example, a model four-level laser transition scheme is depicted in Figure 1.7. Here, the electron is excited from E_0 to E_3 by a photon. The atom will decay immediately to E_3 if the transition probability from E_3 to E_2 is greater than that from E_3 to E0 and E_3 is short lived. If the electrons in E_2 have a long lifetime, the population will grow rapidly. Eventually, electrons in E_2 will decay to E_1, emitting a photon of frequency v_1. If E_1 is unstable, electrons will rapidly decay to ground state E0, keeping the population of E_1 small. In this case, the population is E_2 is quite large and that of E_1 is low. Thus the population inversion is established between E_2 and E_1.

1.3.3 Distribution properties

In general, the laser pulse under consideration has a temporal Gaussian distribution, and the heat flow across the surface can be described by the conduction heat equation [68]:

$$Gt = \rho C_p \frac{\partial T}{\partial t} - \nabla(k\nabla T) \qquad (1.1)$$

where Gt is the heat source distribution in depth, ρ is the material density, C_p is the

specific heat capacity, T is the temperature, t is the time, k is the thermal conductivity. And a typical temperature profile as a function of time is shown in Figure 1.8.

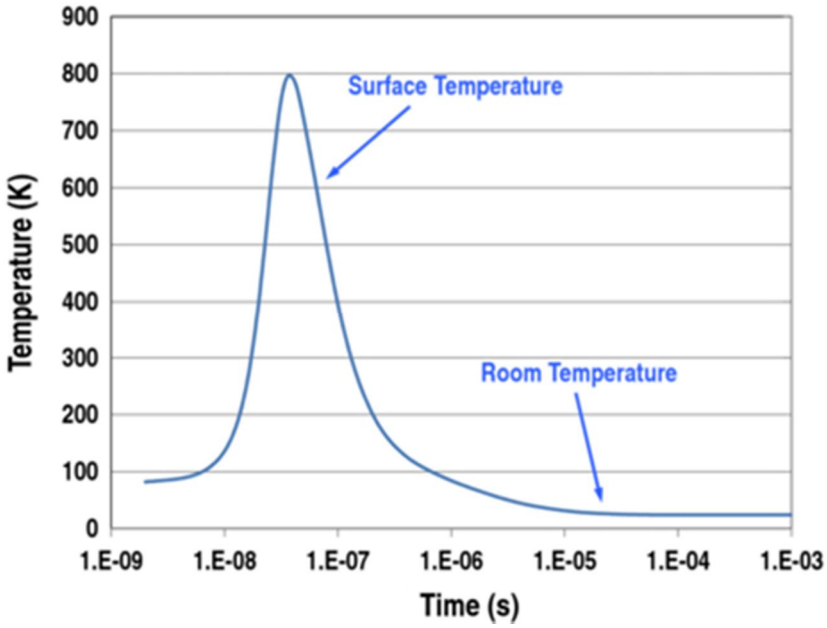

Figure 1.8 Shows temperature profile as a function of time for a silicon sheet after being exposed to a single laser pulse with a KrF excimer laser
"Sedky, S., et al., Microencapsulation of silicon cavities using a pulsed excimer laser. Journal of Micromechanics and Microengineering, 2012. **22**(7)"

1.4 Thin film deposition

Thin film deposition techniques are used to deposit thin film of materials onto a substrate or onto previously deposited layers. It is useful in the manufacturing of electronics, semiconductors, optics, packaging and so on. The deposition techniques fall into two broad categories depending on whether the process is primarily chemical or physical. For chemical deposition, a fluid precursor undergoes a chemical change at a solid surface, leaving a solid layer. Spin coating, chemical vapor deposition, atomic layer deposition are all commonly used chemical deposition routes. Instead of undergoing a chemical change, physical deposition uses mechanical, thermodynamic or electromechanical methods to form a solid thin film. Examples include thermal evaporation, sputtering, pulsed laser deposition, etc.

1.4.1 Magnetron Sputtering System

Figure 1.9 shows a typical sputtering schematic. Sputtering deposition, ejecting material from a target and depositing it on a substrate such as a silicon wafer, is a physical vapor deposition process for depositing thin films. The target is the source

material while substrates are placed in a vacuum chamber which is pumped down to a prescribed process pressure. Sputtering starts when a high voltage is applied to the target materials causing a plasma or glow discharge. Positively charged gas ions (Ar^+) generated in the plasma region are attracted to cathode and sputter the target plate via momentum and energy transfer. The atoms or molecules ejected by Ar-target collisions are deposited on to the surface of the substrates. With the merits of large-area deposition, high uniformity, and good reproducibility, sputtering has been extensively used to deposit thin films of various materials in integrated circuits processing in the semiconductor industry. Thin anti-reflection coatings on glass are also deposited by sputtering for optical applications. It also a good method to deposit contact materials for thin film transistors. Furthermore, this technique is used to fabricate other high-quality functional films, such as thin film sensors, photovoltaic thin films, metal cantilevers and interconnects etc. [69].

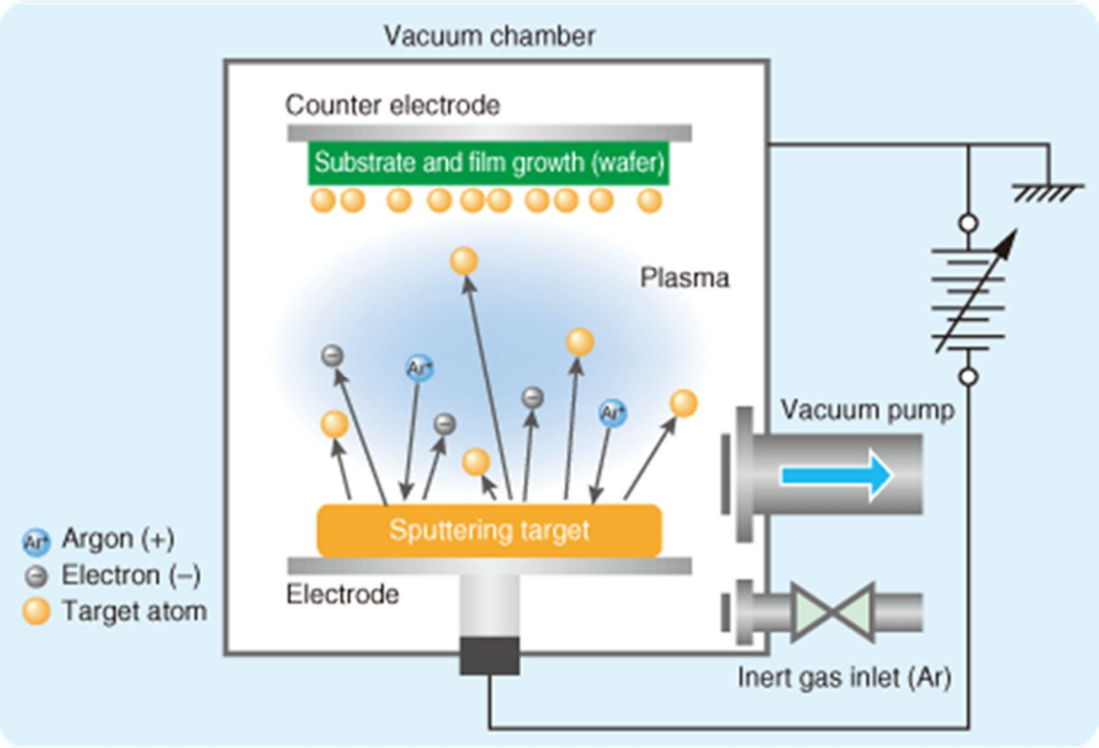

Figure 1.9 A typical sputtering schematic
"From M-SYSTEM CO., LTD web site"

Magnetron sputtering can be done either in direct current (DC) or radio frequency (RF) mode. In DC sputtering, positive charges accumulate on the cathode (targets) and thus eventually the accumulated positive charge negates the negative external bias and extinguishes the plasma. In order to avoid the charge build-up on insulating targets during DC sputtering, an alternative current (AC) in RF 13.5 MHz is applied in sputtering. With the alternative characteristic, the positive charges will stay in plasma

zone and not accumulate in cathode. In this way, the cathode can sustain a high voltage difference and continue the sputtering for insulating films by varying the sign of the anode-cathode bias at a high rate.

An AJA International ATC 2000 UHV sputtering system as shown in Figure 1.10 is used for thin film deposition in this thesis. There are four magnetron sputtering sources which feature in-situ source head tilting allowing precise and repeatable con-focal, direct, and off-axis deposition. 4" or 6" substrates can be used in this system. Argon (Ar) inert gas is injected at the target surface while reactive gases can be injected at the substrate surface for reactive sputtering. Sputter deposition rate is a function of sputter yield of the material, power density into the target and type of power used. By using the standard surface source evaporation equation, a model was set up for our specific sputtering system [70]:

$$\frac{d\bar{M}_s}{dA_s} = \frac{\bar{M}_T(n+1)\cos^n\emptyset\cos\theta}{2\pi r^2} \tag{1.16}$$

where dM_s/dA_s is the mass deposited on the substrate per unit area, M_T is the total mass sputtered from the target, n is the degree of forward peaking of the sputtered flux, $\emptyset$ is the angle between the target surface normal and a line extending from the center of the target to a point on the substrate surface, r is the distance from the center of the target to the substrate surface, and θ is the angle between the substrate surface normal and a line extending from the center of the target surface to a point on the substrate surface. This model incorporates the spatial distribution of the sputtering flux and the geometry of the chamber including the targets and the relevant distances and angles to the substrate holder in our specific chamber.

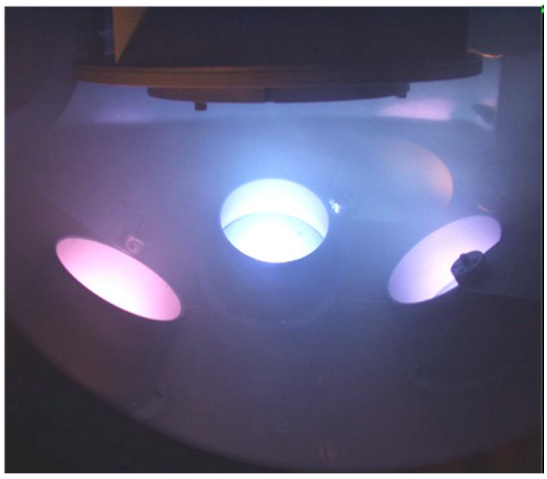

Figure 1.10 AJA International ATC 2000 sputtering system during a 3-component co-sputtering synthesis

CHAPTER 2 EXPERIMENT PROCEDURE

2.1 Cu-Co alloy thin films deposition

Cu-Co alloy thin films with total thickness of ~10 nm were deposited using RF magnetron sputtering system initially pumped to high vacuum (5×10^{-7} Torr). The sputtering conditions are as follow: a 2 inch diameter Cu target (Kurt J. Lesker company) and a RF power of 29 W (120V self-bias) were used for Cu deposition while a 2 inch diameter Co foil target (Alfa Aesar company) and a RF power of 69 W (260V self-bias) were used for Co deposition. Meanwhile, 25 sccm Ar gas at 5 mTorr is the processing pressure. The Cu and Co film thicknesses were measured by Filmetrics F20-UV thin film analyzer. The sputtering rates measured at the center of the substrate were 1.6nm/min for both Cu and Co. Three Cu-Co alloy thin films were deposited on 100 nm SiO_2 coated silicon substrates (100 mm diameter) and quartz (100 mm diameter) respectively via the above sputtering conditions to obtain gradient compositions: (1) 10 nm co-sputtered Cu-Co alloy thin film (co-sputter). (2) 5 nm (at center) Cu thin film covered by 5 nm (at center) Co thin film (Co top Cu bottom). (3) 5 nm (at center) Co thin film covered by 5 nm (at center) Cu thin film (Cu top Co bottom). In addition, 10 nm pure Cu and Co thin films were also prepared on the three substrates described above for comparison with the alloy. The schematics of targets and substrate positions are shown in Figure 2.1.

2.2 Pulsed laser irradiation

All the films were irradiated in air by a normal incident laser beam with 7.5 mm diameter spot. A neodymium-doped yttrium aluminum garnet (Nd:YAG) laser at 266 nm wavelength was used. The laser energy density was chosen to be 90 mJ/cm^2 with 6 pulses for SiO_2 substrates and 80 mJ/cm^2 with 3 pulses for quartz substrates to form nanoparticles, respectively.

2.3 Characterization

A LEO 1525 Scanning Electron Microscope (SEM) was used to capture the morphologies of different stages of pure Cu, Co and Cu-Co alloy thin film dewetting evolutions after pulsed laser irradiation. On each Cu-Co alloy sample (SiO_2 and quartz substrates), five positions were irradiated and characterized. They are 10 mm (S1), 30 mm (S2), 50 mm (S3), 70 mm (S4) and 90 mm (S5) away from Cu-rich edge. Figure 2.1 also shows the substrates with locations.

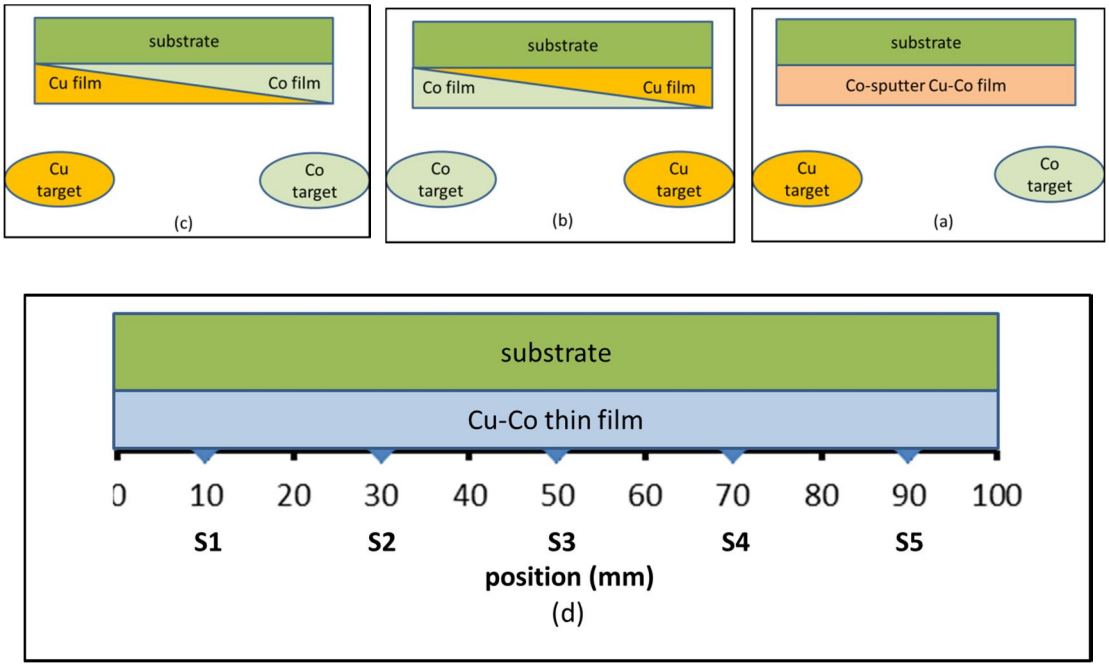

Figure 2.1 (a-c) Schematics of three Cu-Co thin film structures: co-sputter (a), Co top Cu bottom (b) and Cu top Co bottom (c). Illustration of Cu-Co thin film surface with locations.

Energy Dispersive Spectroscopy (EDS) analysis was also obtained by LEO 1525 to measure the compositions at different position for Cu-Co thin films deposited on SiO_2 substrates and membranes. EDS measurements were operated on both thin films and particles on all the samples with 4kV accelerating voltage and 8 mm working distance.

The reflectance of all samples on SiO_2 and quartz substrates was measured using a Filmetrics F20-UV thin film analyzer between 200 to 900 nm wavelength. Additionally, Cary 5000 (Varian Inc.) between 300 to 1000 nm wavelengths was used for absorption and transmission measurement of samples deposited on quartz substrates.

CHAPTER 3 EXPERIMENT RESULTS

3.1 Thin film and particle properties of Cu-Co on SiO_2 substrates

The composition of Cu and Co and optical properties of thin films on SiO_2 substrates were measured using EDS, Filmetrics F20-UV thin film analyzer and Cary 5000 (Varian Inc.) as mentioned in the experiment procedure. After laser irradiation, the composition, optical properties and distribution of nanoparticles were also obtained.

3.1.1 Composition analysis of Cu-Co thin films

The composition of each sample at different substrate position was examined by EDS measurement. During the process, all samples were tilted 45 degrees and the aperture size was 120μm. Table 3.1 shows the resultant average atomic percentage of Cu using Origin software. Meanwhile, both average composition and the standard error versus position for each sample are also plotted in scatter chart shown in Figure 3.1. It shows the Cu composition gradient in the thin film as a function of distance along a line on the substrate surface. This line lies along a plane that intersects the centers of both the Cu and Co targets, and the substrate surface. Typical EDS spectra of Cu-Co thin film, presented in Figure 3.2 to 3.4, indicate the presence of Cu and Co together with the substrate materials, Silicon (Si) and Oxygen (O).

Table 3.1 Cu atomic percentage of at position S1, S2, S3, S4, and S5 of co-sputter, Co top Cu bottom and Cu top Co bottom Cu-Co thin film on SiO_2 substrates

Position	S1	S2	S3	S4	S5
Co-sputter Cu at. %	67	55	34	19	10
Co top Cu bottom Cu at. %	67	48	32	15	6
Cu top Co bottom Cu at. %	68	51	32	17	9

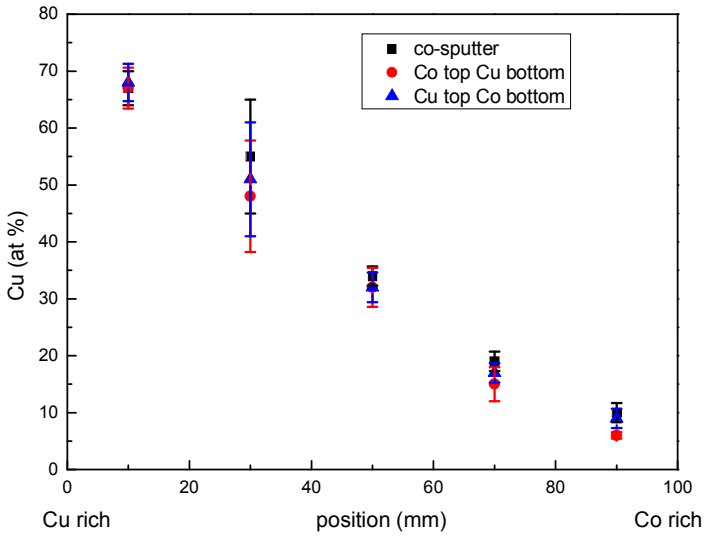

Figure 3.1 Cu atomic compositions and stand error versus position for co-sputter (black square), Co top Cu bottom (red circle) and Cu top Co bottom (blue triangle). Each data point is an average of several spectra

In Table 3.1, each sample has a similar composition at the five positions. The percentage of Cu has a range from ~5% to ~70%. At the S3 (center) position, the ratio of Cu to Co is lower than 1:1 for all three samples. In this figure, the average composition of Cu atom is nearly linearly dependent to the sample surface position. And the standard errors, shown in Figure 3.1, are very small except for the S2 position.

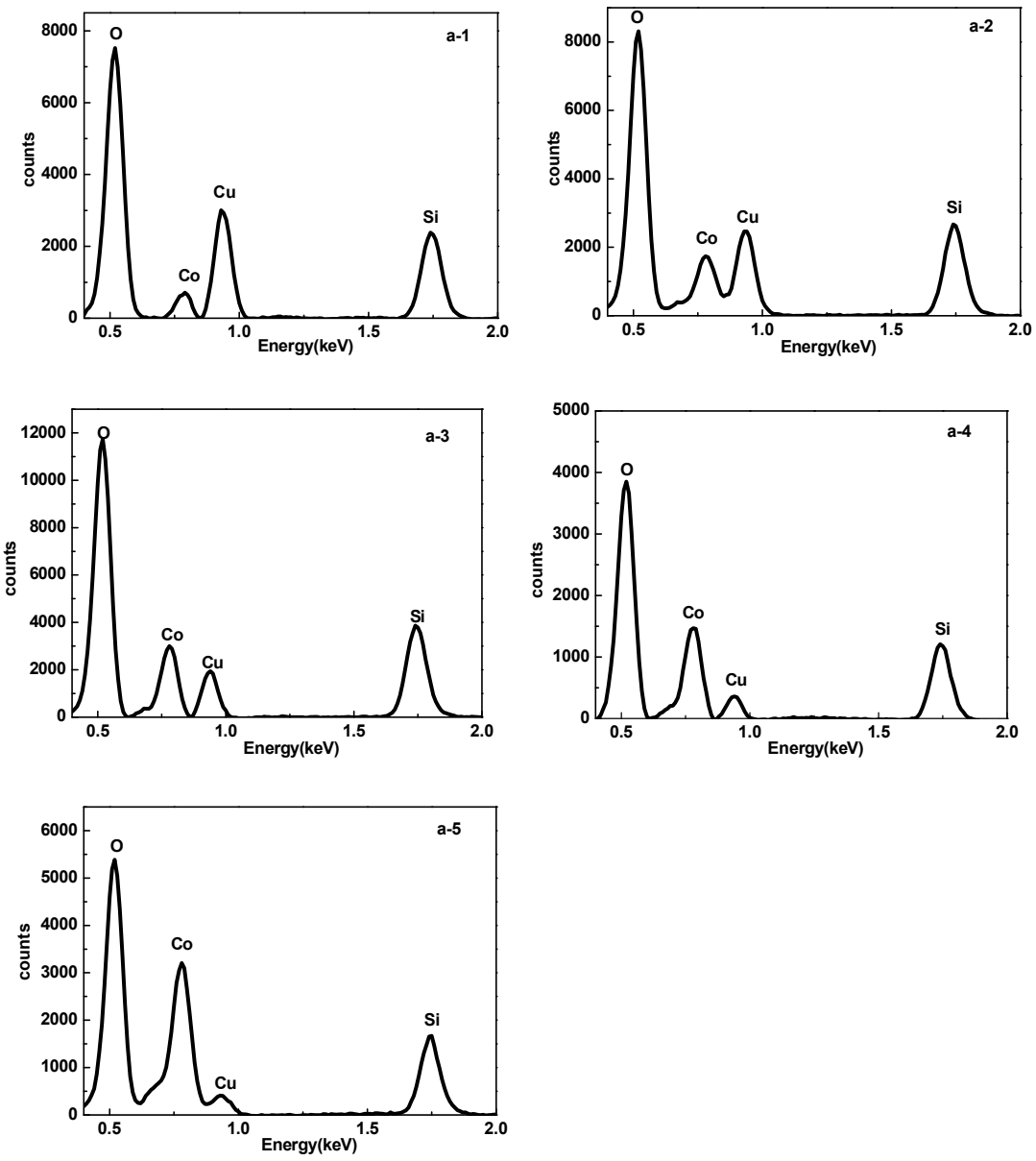

Figure 3.2 (a-1 to a-5) Typical EDS spectra of co-sputter Cu-Co thin film on SiO_2 substrate at the five positions along the substrate

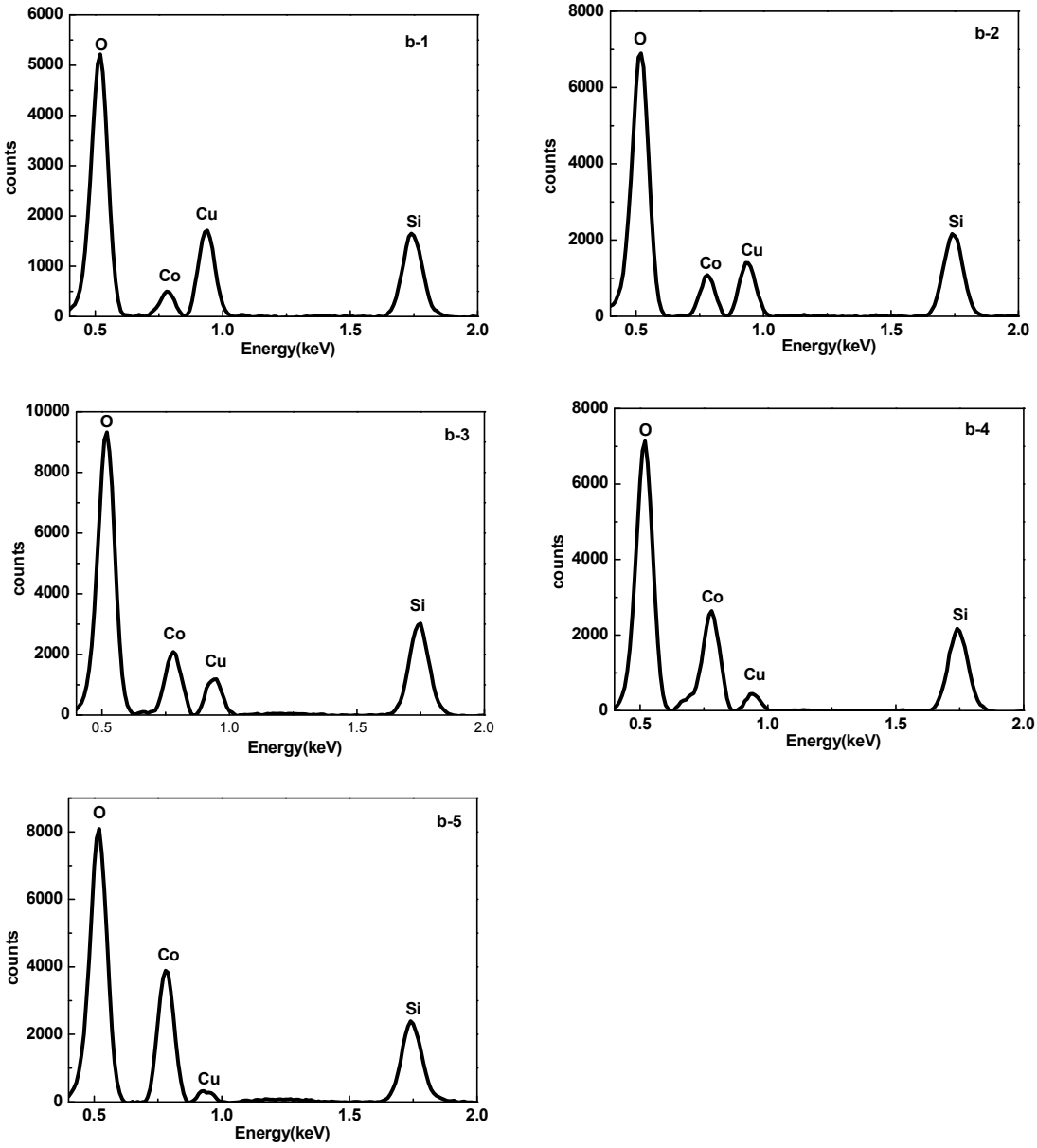

Figure 3.3 (b-1 to b-5) Typical EDS spectra of Co top Cu bottom Cu-Co thin film on SiO_2 substrate at the five positions along the substrate

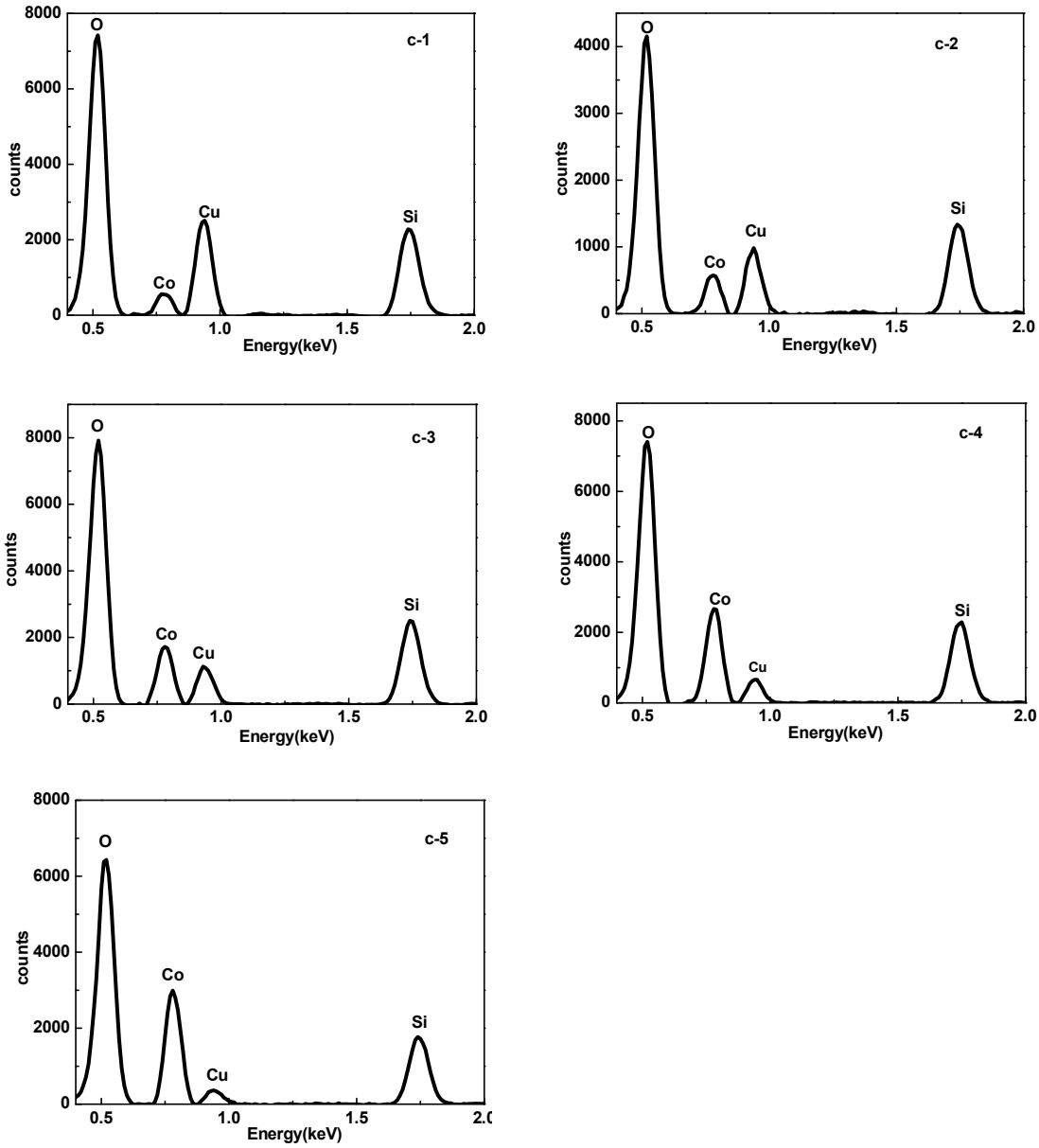

Figure 3.4 (c-1 to c-5) Typical EDS spectra of Cu top Co bottom Cu-Co thin film on SiO_2 substrate at the five positions along the substrate

In each typical EDS spectrum, both the thin film (Cu and Co) information and substrate materials (Si and O) information are captured since the films are only ~10 nm thick. According to the spectra, the counts from Cu decrease from position 1 to 5, which is consistent with our expectations since the substrate position is further from the copper target. As expected, all the three samples have this trend.

3.1.2 Reflectance of Cu-Co thin films

The reflectance of Cu-Co thin films and particles was measured with a Filmetrics F20-UV thin film analyzer between 200 to 900 nm wavelengths at different position.

The results were also compared with pure Cu and Co films. Figure 3.3 shows the detail information about the reflectance at all five positions of each sample. Furthermore, the reflectance of the three samples at same position is also compared in Figure 3.4.

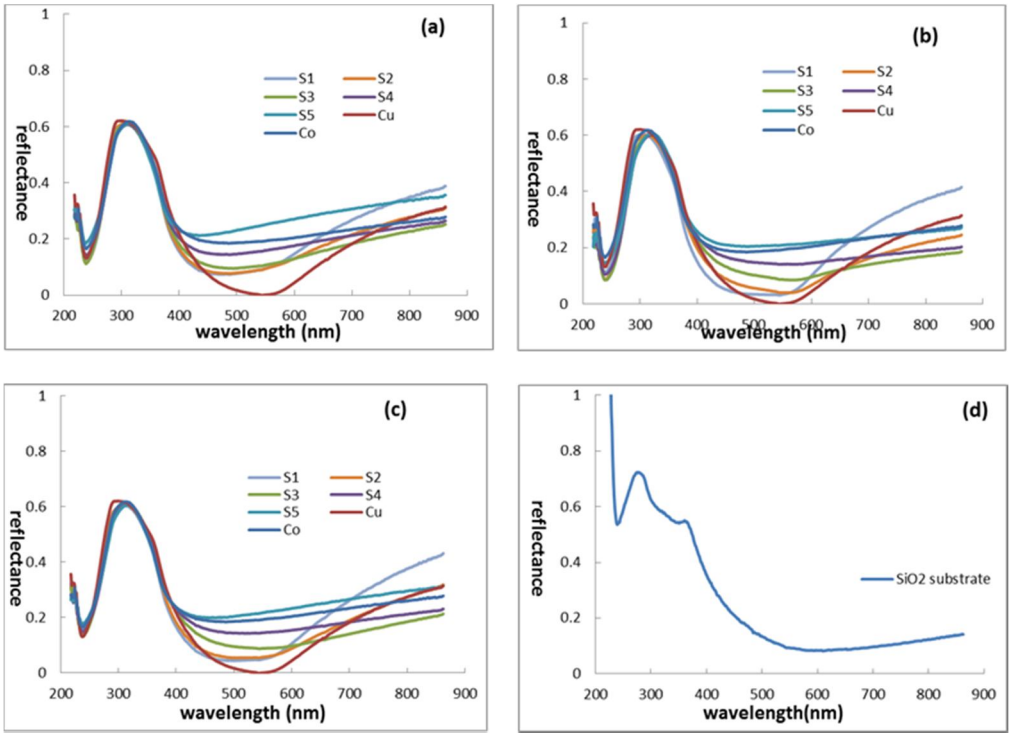

Figure 3.5 Reflectance of co-sputter (a), Co top Cu bottom (b) and Cu top Co bottom (c) Cu-Co thin films at each position compared with reflectance of pure Cu and Co. (d) is reflectance of 100 nm SiO_2/Si wafer

For these three reflectance graphs, the main trend is similar. The highest reflectance shows up in the Ultra Violet (UV) range which is attributed to the silicon substrate signal (this can be confirmed by comparison with the reflectance of pure substrate). In this wavelength range, the reflectance of each sample is almost same. The samples vary as the wavelength approaches 400 nm. From 400 nm to 600 nm, the reflectance decreases with increasing Cu concentration. This is due to the inter-band gap transition. As the wavelength increases to 700 nm, the reflectance increases.

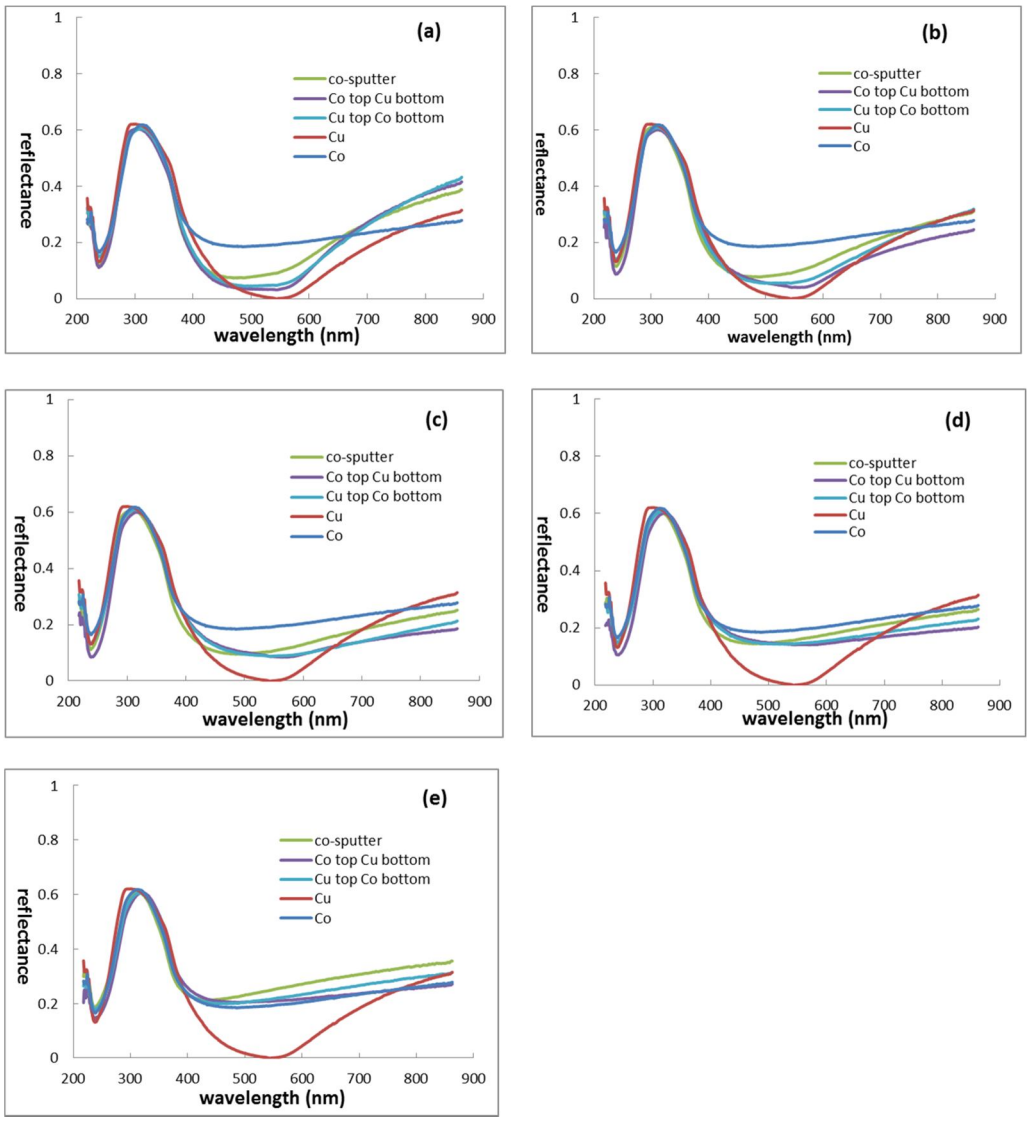

Figure 3.6 The reflectance of pure Cu, Co and Cu-Co thin film samples at all five positions: S1 (a), S2 (b), S3 (c), S4 (d) and S5 (e)

There is not much difference from 200 nm to 400 nm in Fig. 3.4. In general, the three different samples have similar reflectance which is not unexpected since the multi-layer thickness is much smaller than the wavelength, thus a simple rule of mixtures is expected.

3.1.3 SEM and particle distributions of Cu-Co thin films

All the Cu-Co thin film samples were irradiated by Nd:YAG Q-switch laser using appropriate energy to form nanoparticles. The particle morphology was obtained by SEM. Furthermore, the resultant SEM images were analyzed to determine the particle size distribution using Image J software. Figure 3.7, 3.8 and 3.9 present particle properties of co-sputter, Co top Cu bottom and Cu top Co bottom samples respectively. The resultant average particle diameters are summarized in Table 3.1.

and Figure 3.10.

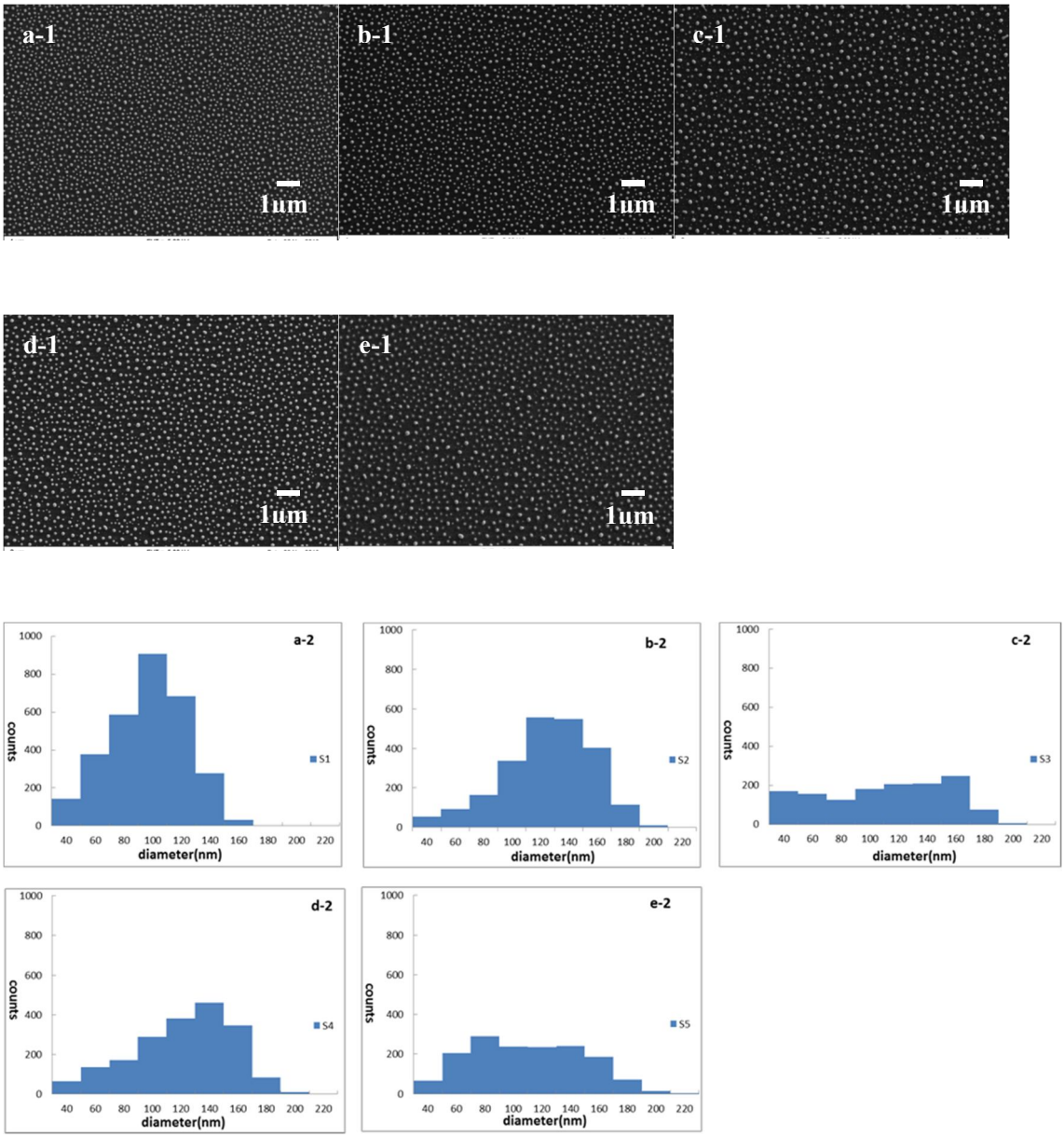

Figure 3.7 SEM images of co-sputter Cu-Co particles at S1 (a-1), S2 (b-1), S3 (c-1), S4 (d-1) and S5 (e-1) positions. Particle diameter size distribution of co-sputter Cu-Co sample at Cu40 S1, Cu20 S2, center S3, S4 (d-2) and S5 (e-2) positions

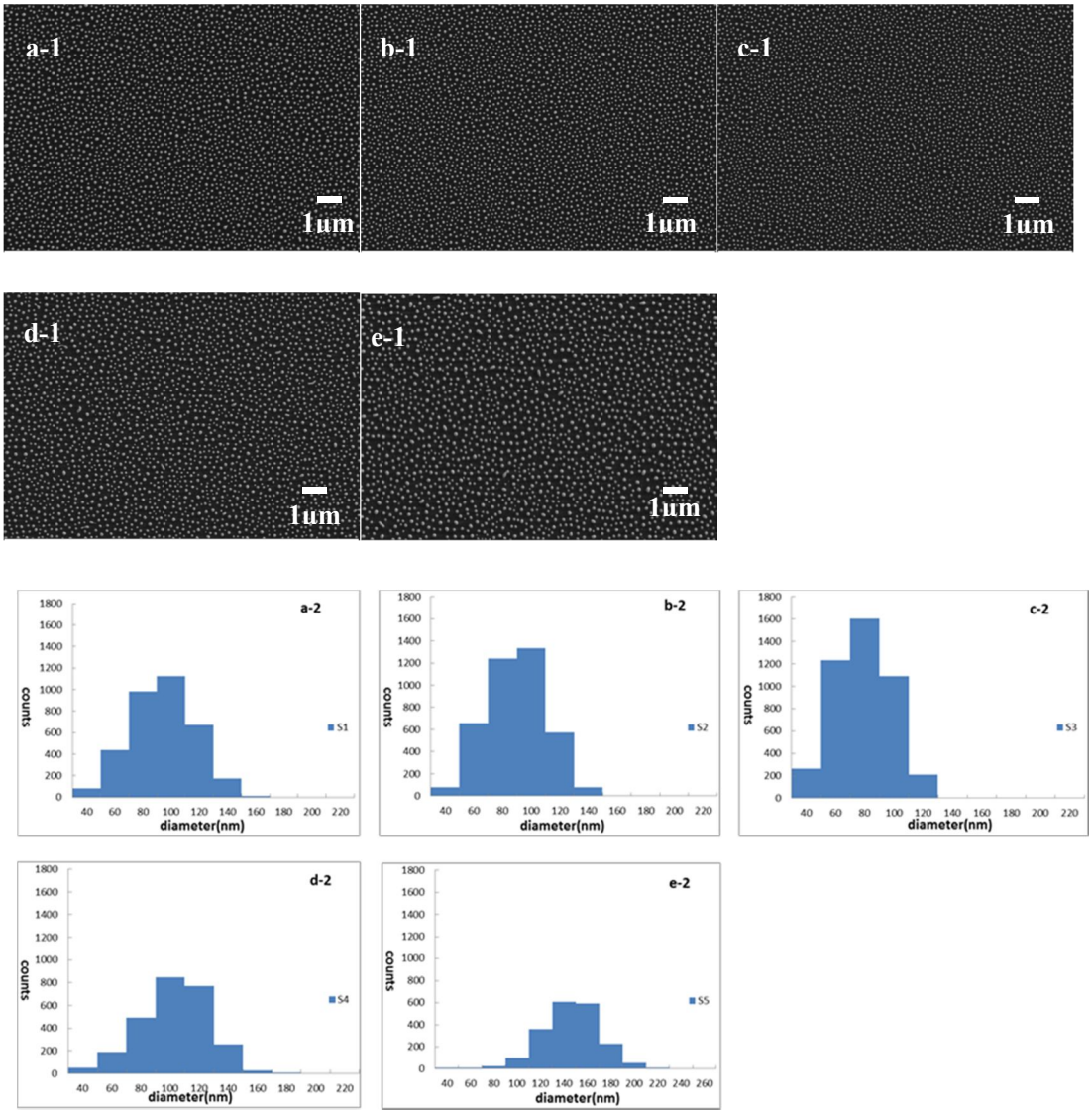

Figure 3.8 SEM images of "Co top Cu bottom" Cu-Co particles at S1 (a-1), S2 (b-1), S3 (c-1), S4 (d-1) and S5 (e-1) positions. Particle diameter size distribution of co-sputter Cu-Co sample at S1 (a-2), S2 (b-2), S3 (c-2), S4 (d-2) and S5 (e-2) positions

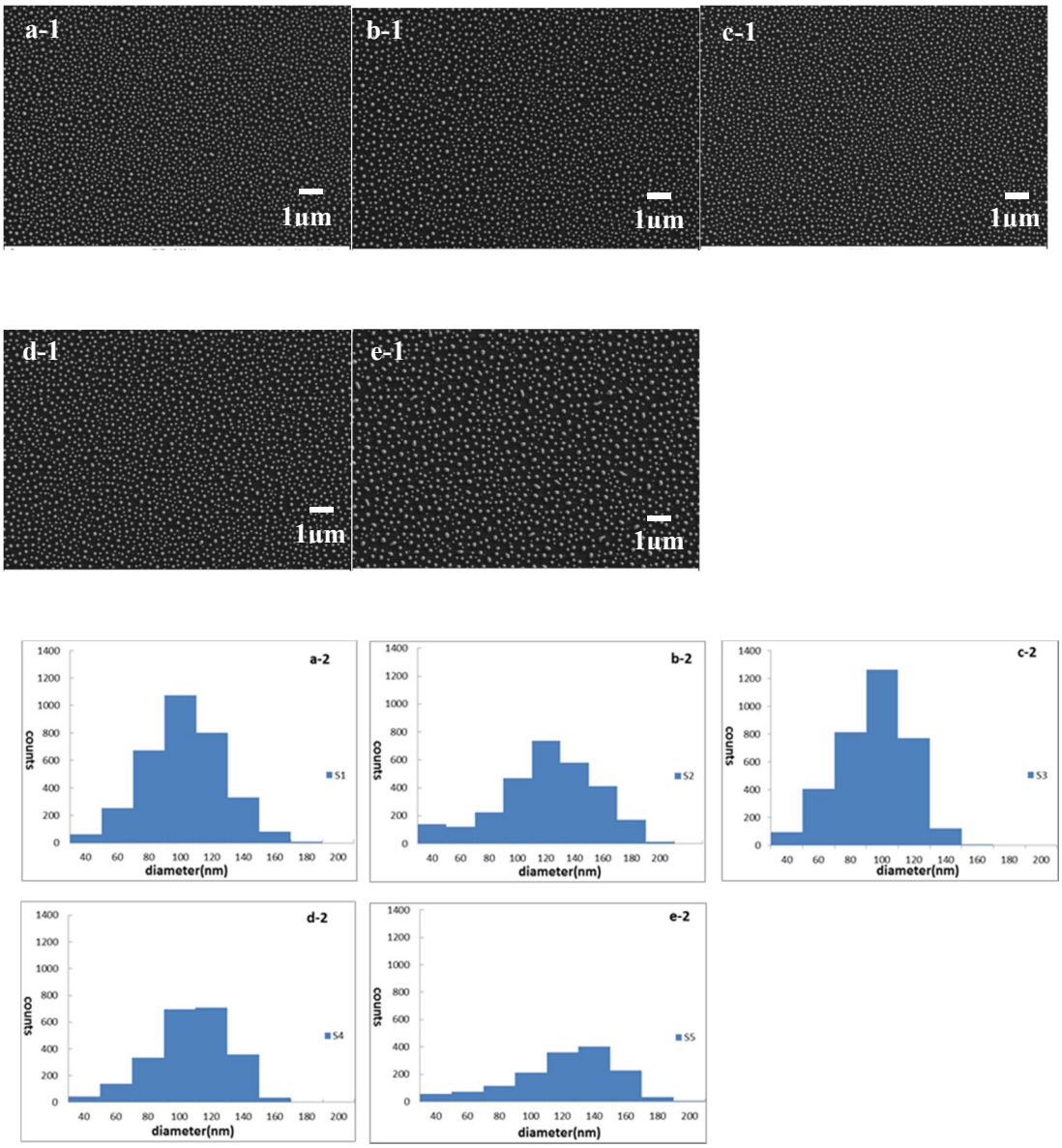

Figure 3.9 SEM images of "Cu top Co bottom" Cu-Co particles at S1 (a-1), S2 (b-1), S3 (c-1), S4 (d-1) and S5 (e-1) positions. Particle size distribution of co-sputter Cu-Co sample at S1 (a-2), S2 (b-2), S3 (c-2), S4 (d-2) and S5 (e-2) positions

After 6 pulses laser irradiation with 90 mJ/cm^{2}energy density, all the Cu-Co thin films were dewetted into particles. In every image, particles are well saturated and dispersed.

For co-sputtered Cu-Co sample, the uniformities of particle size at position S3 and S5 are not as good as others. This can be observed in both SEM images and histograms. There are quite a number of particles with small size at the center of the sample, while there are certain numbers of particles in every size range at position S5. For the other positions, most particles have diameters between 80 nm to 120 nm.

From the SEM images in Figure 3.6, we can observe that particles at the Co rich position have a larger diameter size than that of other four positions. This is also confirmed in the following histograms. The diameter size of most particles at position S1, S2, S3 and S4 are between 60 nm and 120 nm. However, the particle size concentrated at 120 nm to 180 nm for position S5.

Even though there are still some small particles with small diameters at some positions (especially position S2 and S5), the majority of particles have diameters ranging from 80 nm to 160 nm in the Cu top Co bottom sample.

Additionally, all the SEM images shown above were analyzed by ImageJ software to collect the average particle size for each sample at the five positions. They are presented in Table 3.2. The scatter plot in Figure 3.8 also provides a simple way to compare the particle size.

Table 3.2 Average particle diameter at positionS1, S2, S3, S4 and S5 of co-sputter, Co top Cu bottom and Cu top Co bottom thin films on SiO_2 substrates

position	S1	S2	S3	S4	S5
Co-sputter particle dia.(nm)	87	115	100	111	100
Co top Cu bottom particle dia.(nm)	84	79	69	92	135
Cu top Co bottom particle dia.(nm)	92	111	85	96	111

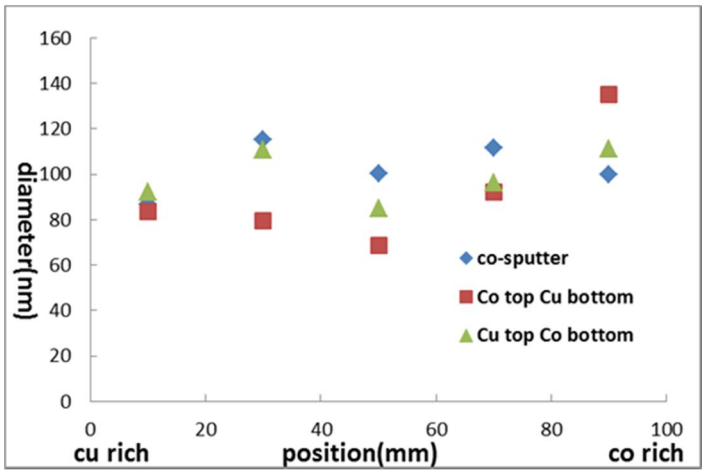

Figure 3.10 Scatter plot of average particle diameter at position S1, S2, S3, S4 and S5 of co-sputter, Co top Cu bottom and Cu top Co bottom thin films on SiO_2 substrate

The particle diameters of Co top Cu bottom sample have a larger variation as a function of different positions compared with other two samples. Table 3.4 shows the particle diameter for this sample varies from 70 nm (S3) to 135 nm (S5). For co-sputter and Cu top Co bottom samples, the majority of particles have a diameter around 100 nm with a small deviation.

3.1.4 Composition analysis of Cu-Co particles

The composition of each sample at different positions was examined by EDS measurement. During the process, the aperture size was 120μm in order to get stronger signals. Table 3.2 shows the resultant average atomic percentage of Cu using Origin software. Additionally, both average composition and the standard error versus position for each sample are also plotted on the scatter chart shown in Figure 3.11. Typical EDS spectra of Cu-Co particles, presented in Figure 3.12 to 3.14, indicate the presence of Cu and Co together with the substrate materials, Silicon (Si) and Oxygen (O).

Table 3.3 Cu atomic percentage at position S1, S2, S3, S4 and S5 of co-sputter, Co top Cu bottom and Cu top Co bottom Cu-Co particles on SiO_2 substrates

position	S1	S2	S3	S4	S5
Co-sputter Cu at. %	77	58	31	20	9
Co top Cu bottom Cu at. %	74	64	42	22	12
Cu top Co bottom Cu at. %	76	67	38	19	11

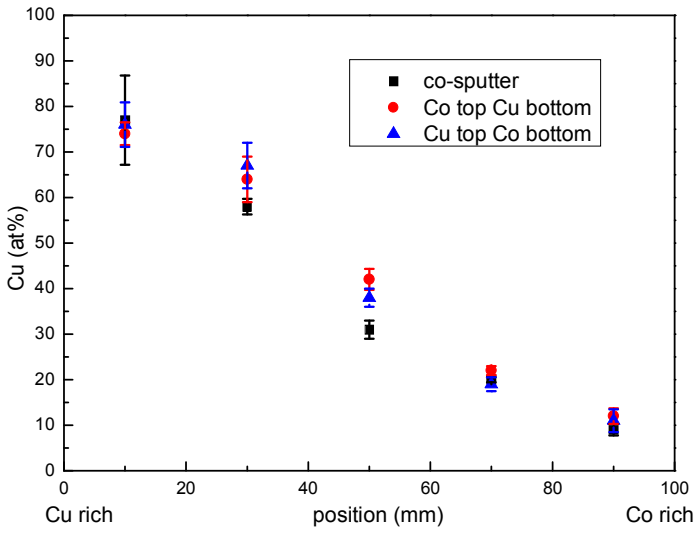

Figure 3.11 Cu atomic compositions and stand error versus position for co-sputter (black square), Co to Cu bottom (red circle) and Cu top Co bottom (blue triangle). Each data point is an average of several spectra

In Table 3.3, each of the 3 samples have similar compositions at the five positions. The percentage of Cu has a range from ~10% to ~80%. At the S3 position, the atomic percentage of Cu is lower than 50% for all three samples. Figure 3.11 shows a scatter

plot of the Cu composition gradient in the thin film as a function of distance along a line on the substrate surface. In this figure, the average composition of Cu is nearly linearly dependent to the sample surface position.

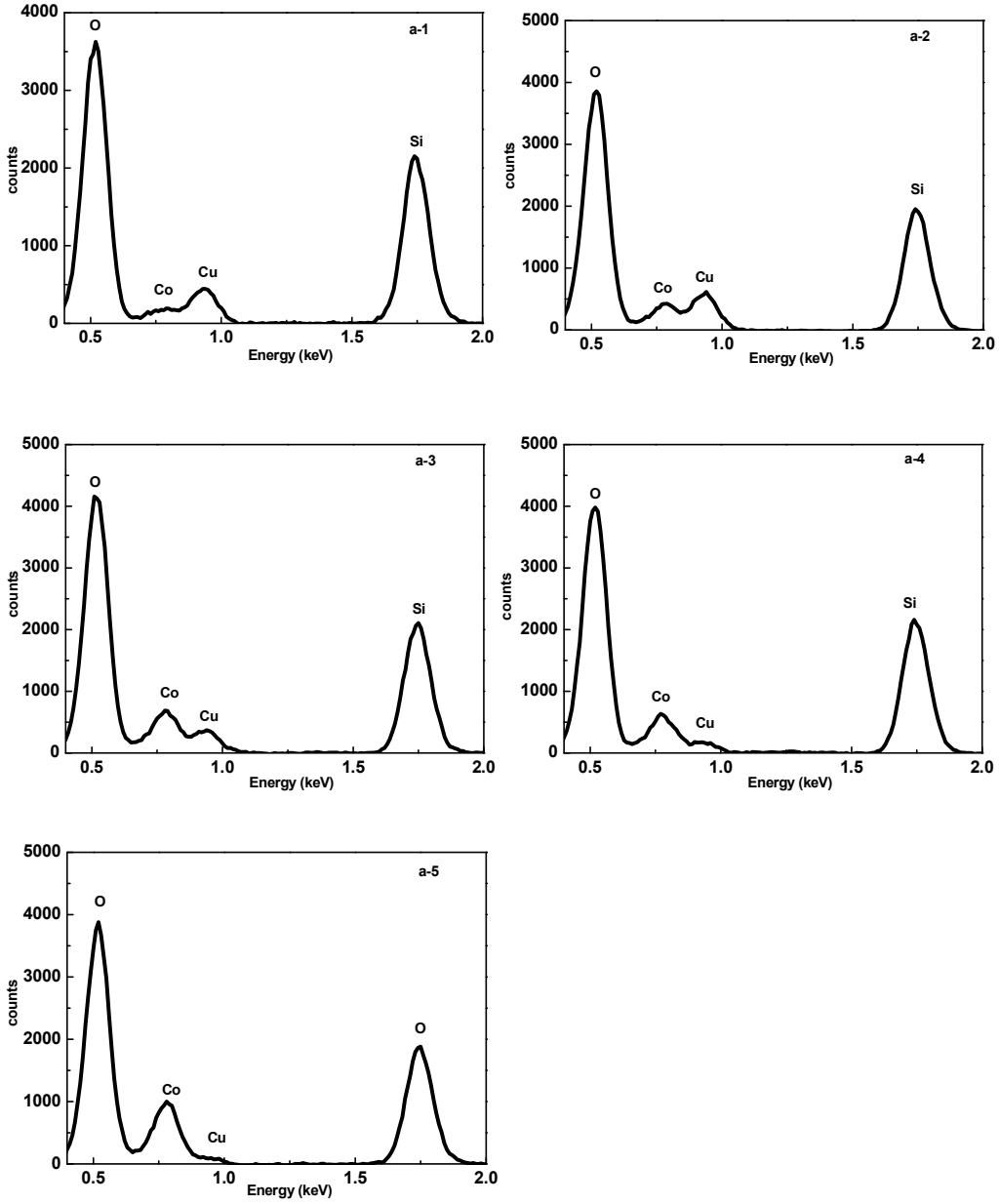

Figure 3.12 (c-1 to c-5) Typical EDS spectra of co-sputter Cu-Co particles on SiO_2 substrate

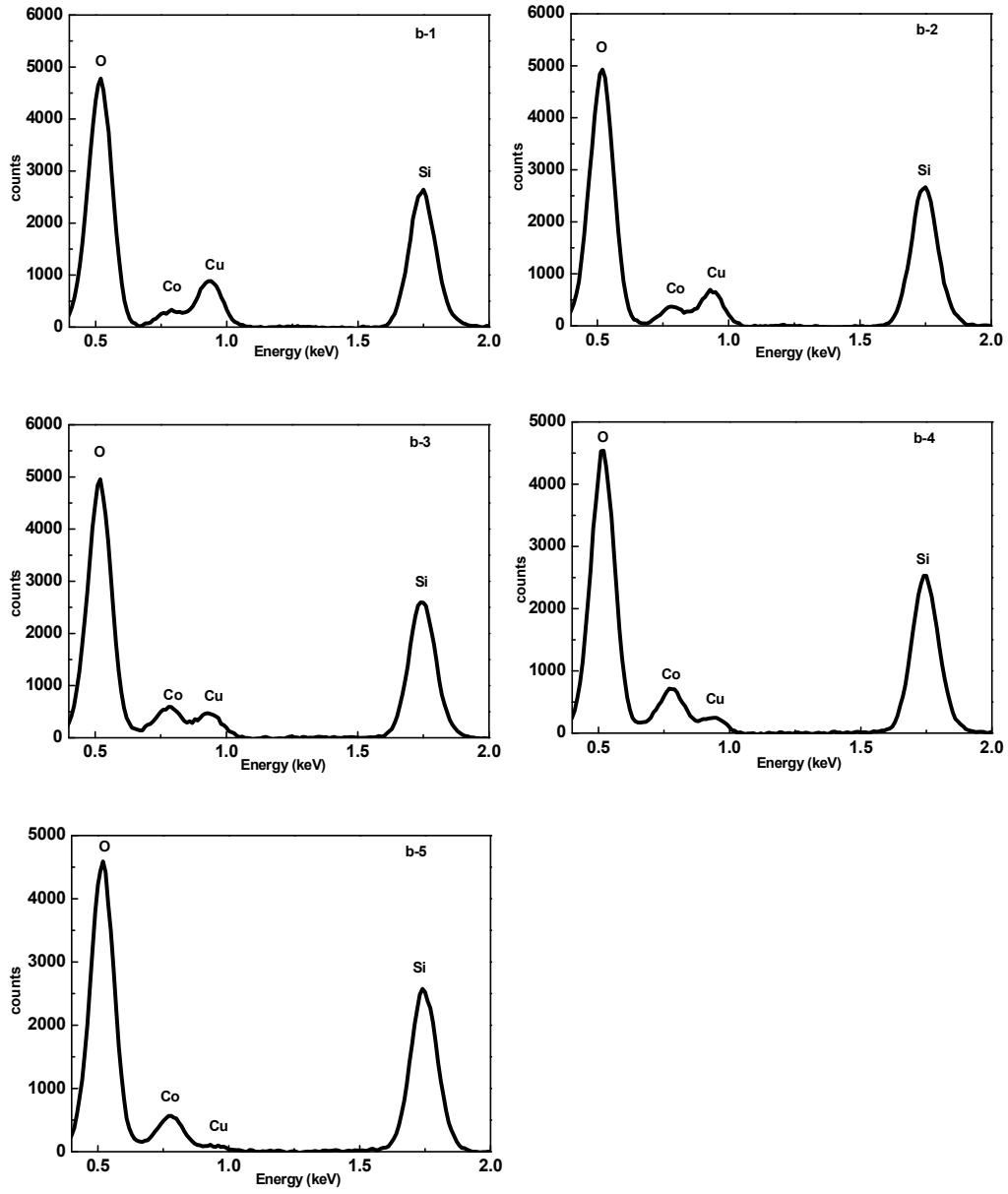

Figure 3.13 (c-1 to c-5) Typical EDS spectra of Co top Cu bottom Cu-Co particles on SiO_2 substrate

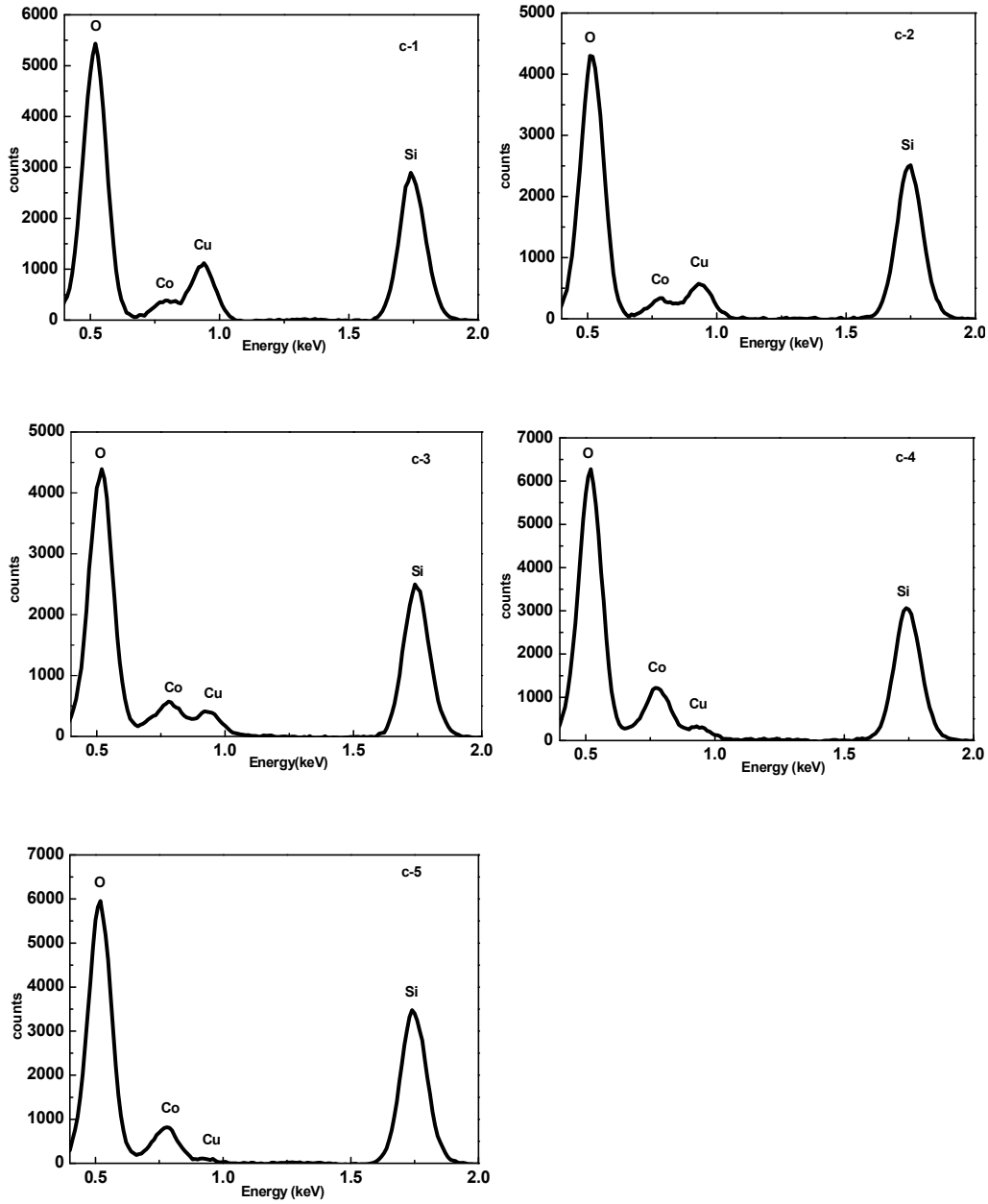

Figure 3.14 (c-1 to c-5) Typical EDS spectra of Cu top Co bottom Cu-Co particles on SiO_2 substrate

Each typical EDS spectrum indicates both Cu-Co particles and substrate materials (Si and O) information. According to the spectra of all the three samples, the counts of Cu atom descend with the decrease of Cu, which is consistent with the results shown in Table 3.3 and Figure 3.11.

3.1.5 Reflectance of Cu-Co particles

Cu-Co particles were obtained with laser irradiation at all five positions of three thin film samples. The reflectance of Cu-Co particles at the corresponding positions was

measured by Filmetrics F20-UV thin film analyzer and presented in Fig 3.15 and 3.16.

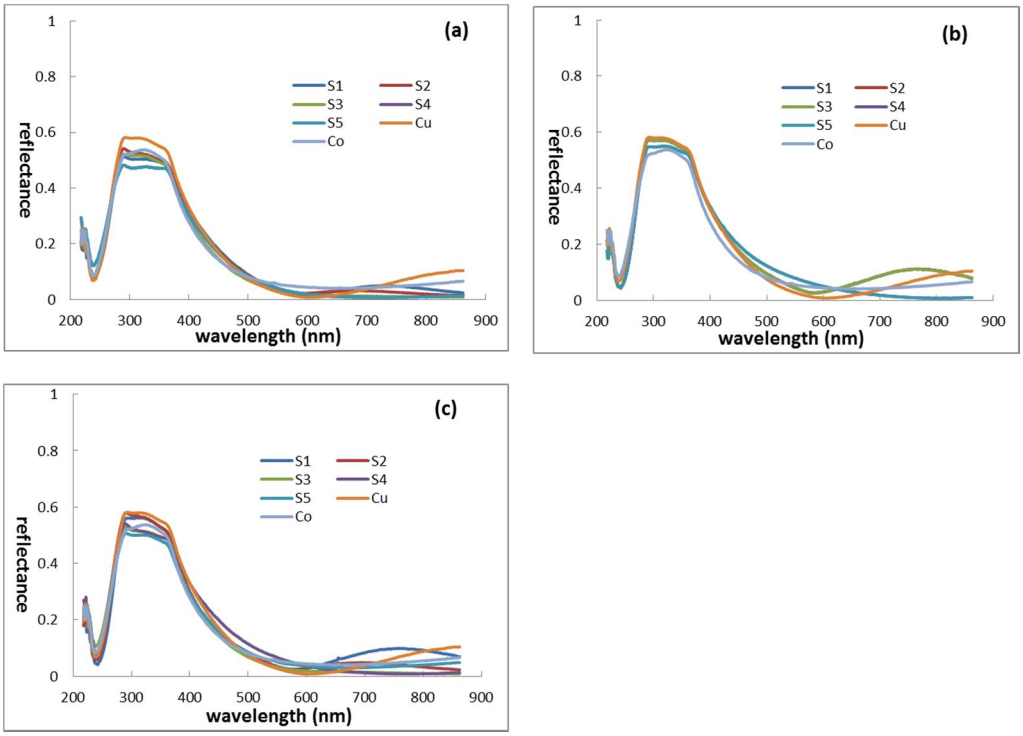

Figure 3.15 Reflectance of co-sputter (a), Co top Cu bottom (b) and Cu top Co bottom (c) Cu-Co particles at each position compared with reflectance of pure Cu and Co

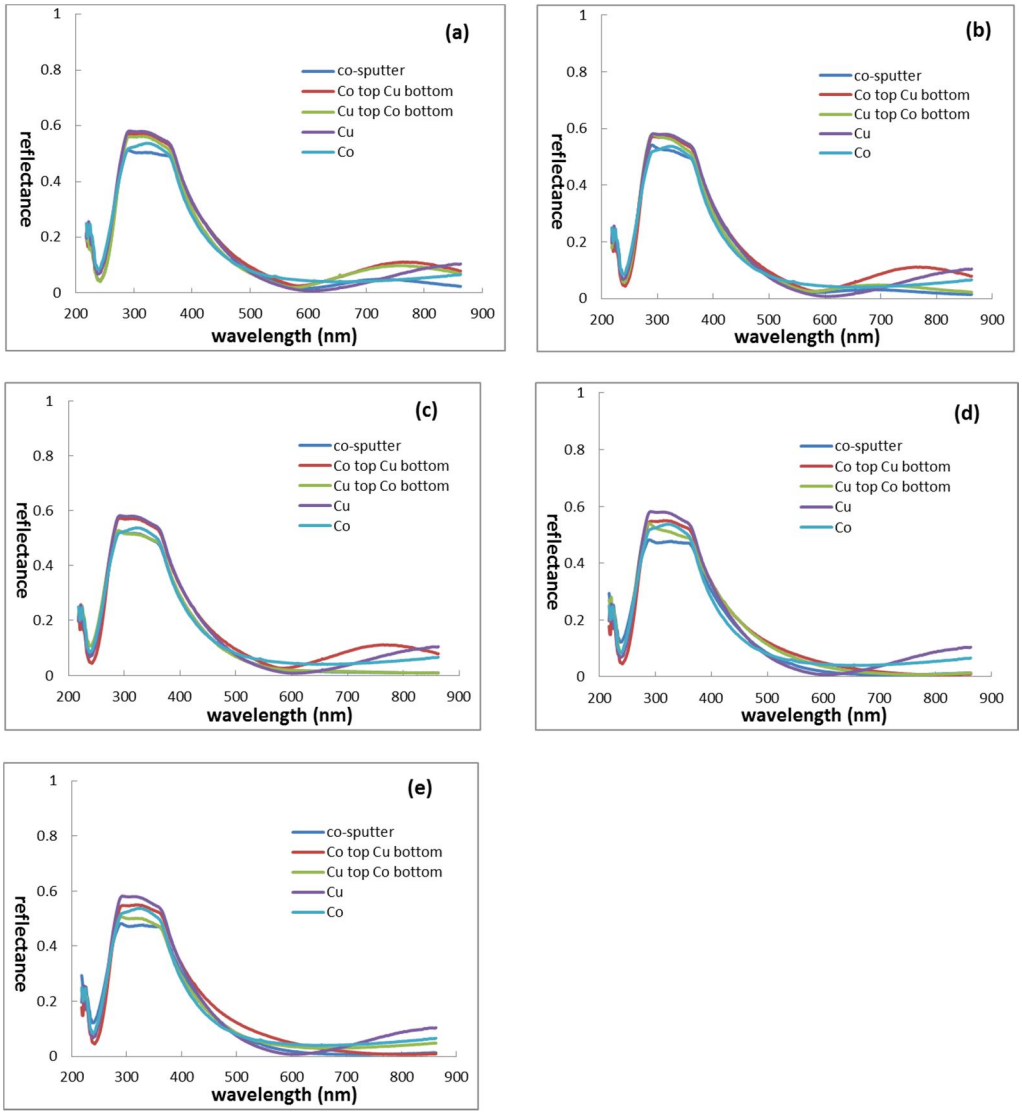

Figure 3.16 Reflectance of pure Cu, Co and Cu-Co particles samples at all five positions: S1 (a), S2 (b), S3 (c), S4 (d) and S5 (e)

Figure 3.15 reveals a rapid increase of reflectance at the range from 250 nm to 300 nm. All these three Cu-Co thin film structures show reflection peaks between 300 nm to 300 nm wavelength, which is quite flat. After that, the reflectance decrease gradually. Comparing the reflectance at all five positions and pure Cu, Co, there is no significant reflectance difference between them except the emergence of a small peak in the near infrared region (~ 700 nm) for copper rich nanoparticles. The trend shown in Figure 3.16 is quite similar to Figure 3.15.

3.2 Thin film and particle properties of Cu-Co on quartz substrates

The optical properties of thin films on quartz substrates were measured using Filmetrics F20-UV thin film analyzer and Cary 5000 (Varian Inc.) as mentioned in the experiment procedure. After laser irradiation, the optical properties and distribution of

Cu-Co particles were also obtained.

3.2.1 SEM and particle distributions of Cu-Co thin films

All the Cu-Co thin film samples were irradiated by Nd:YAG Q-switch laser using appropriate energy to form nanoparticles. And the particle morphology was obtained by SEM. Furthermore, the resultant SEM images were analyzed to determine the particle size distribution using Image J software. Figure 3.17, 3.18 and 3.19 present particle properties of co-sputter, Co top Cu bottom and Cu top Co bottom samples respectively. The resultant average particle diameters are summarized in Table 3.4 and Figure 3.20.

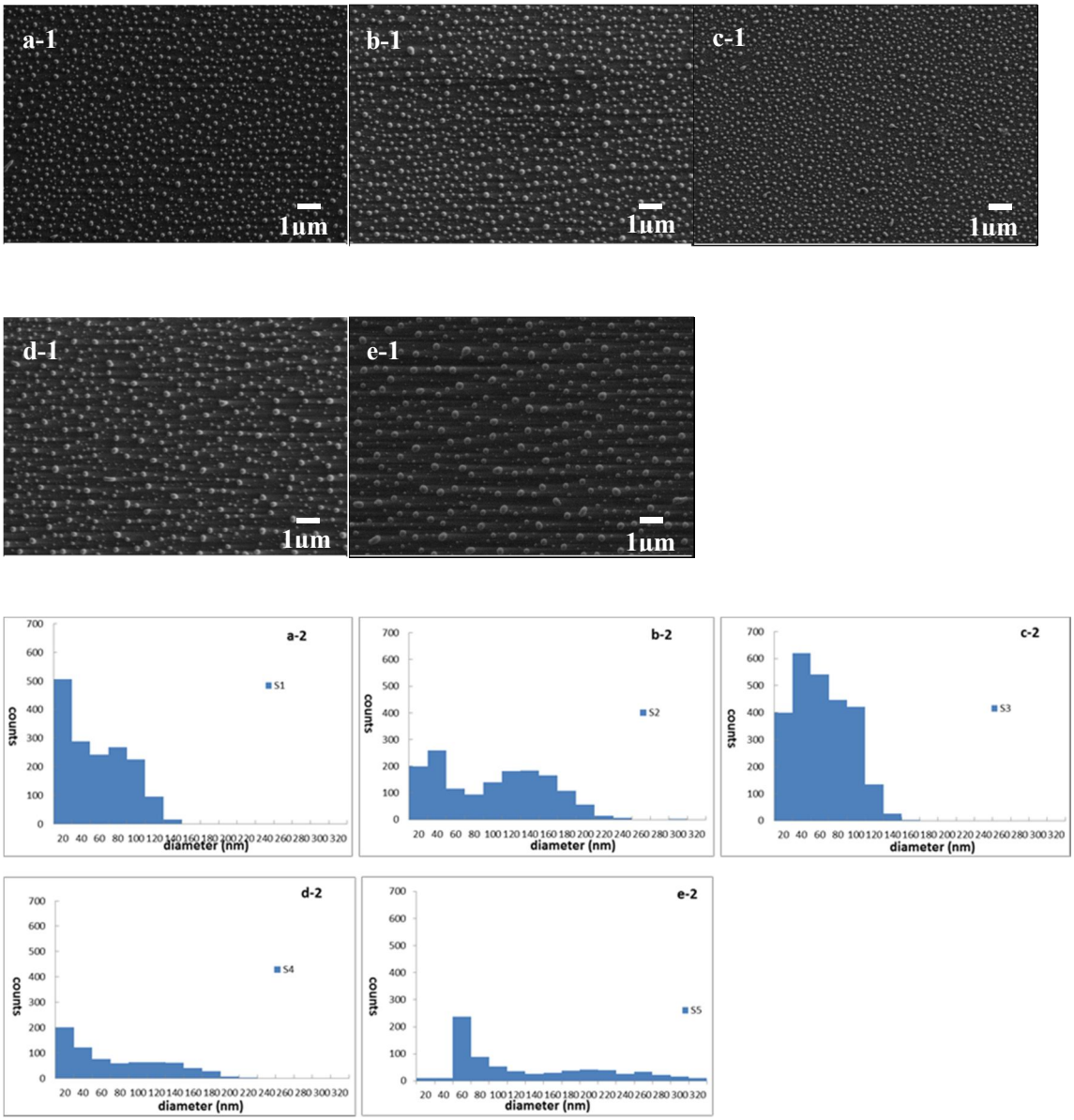

Figure 3.17 SEM images of co-sputter Cu-Co particles at S1 (a-1), S2 (b-1), S3 (c-1), S4 (d-1) and S5 (e-1) positions. Particle diameter size distribution of co-sputter Cu-Co sample at S1 (a-2), S2 (b-2), S3 (c-2), S4 (d-2) and S5 (e-2) positions

From the SEM images, we can observe that particles are all saturate completely. However, the particles distribution is totally different. Co-sputtered Cu-Co particles have a better uniformity at position S1 and S3 than that of other positions. At Co-rich position (S5), particles with quite large size are also formed during pulsed laser irradiation. The histograms reveal that particles size ranges from 20 nm to 160 nm at these two positions while other positions show a much wider range. For the five positions, a large number of particles have diameters within 20 nm, especially for the particles located at position S5. In this area, almost the diameters of all particles are less than 60 nm.

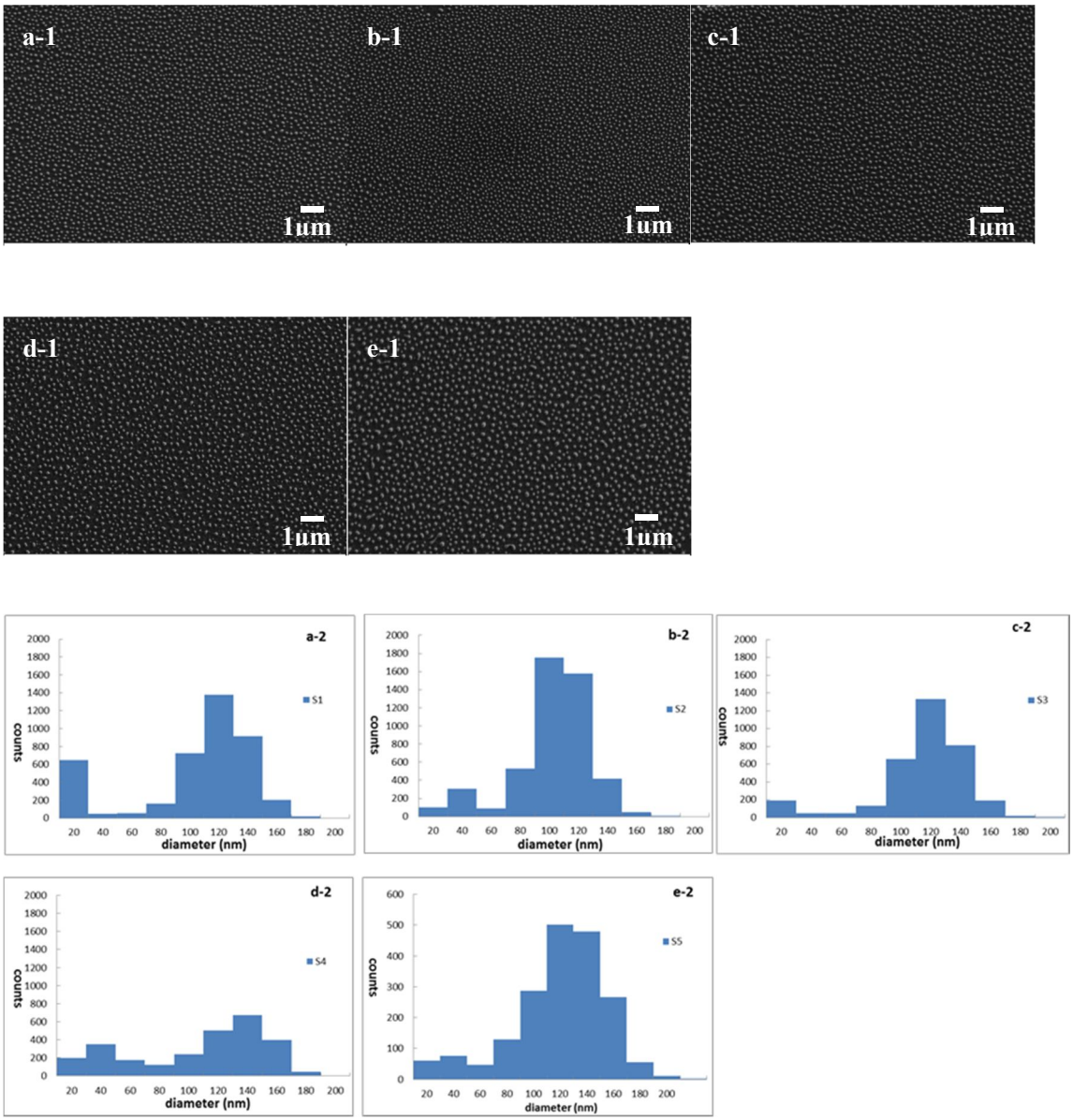

Figure 3.18 SEM images of "Co top Cu bottom" Cu-Co particles at S1 (a-1), S2 (b-1), S3 (c-1), S4 (d-1) and S5 (e-1) positions. Particle diameter size distribution of co-sputter Cu-Co sample at S1 (a-2), S2 (b-2), S3 (c-2), S4 (d-2) and S5 (e-2) positions

The SEM images of Co top Cu bottom structure shows a good uniformity. Generally speaking, the particles at position S2 have a smaller size than that of other four positions. This phenomenon can also be confirmed by the histogram which shows a large number of particles are smaller than 20 nm. At positions S1 and S3, particles have quite uniform sizes, and most of them have diameters between 100 nm to 140 nm. There are also some particles with sizes located at 0~20 nm range, but the number is not larger than that of position S2.

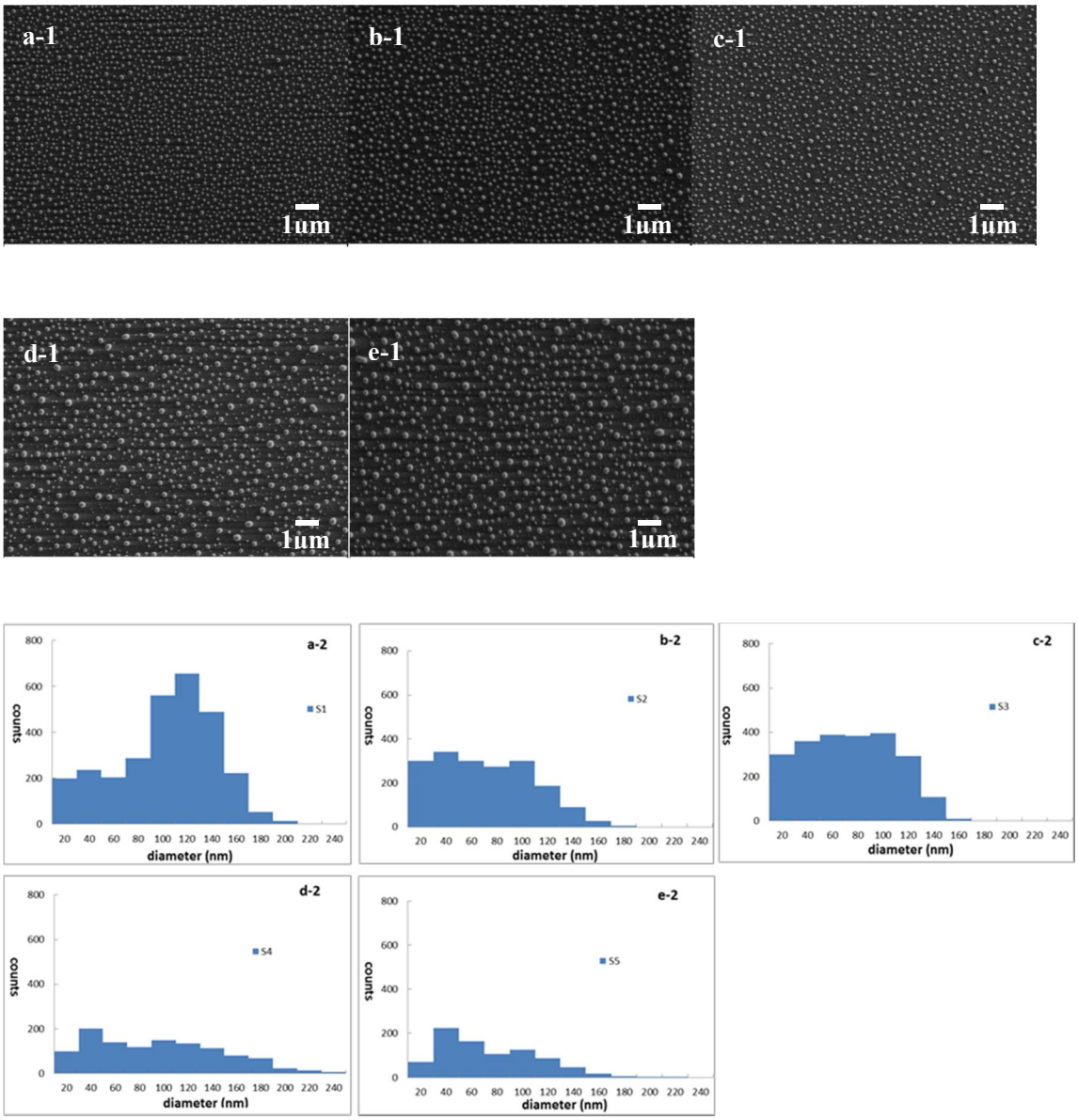

Figure 3.19 SEM images of "Cu top Co bottom" Cu-Co particles at S1 (a-1), S2 (b-1), S3 (c-1), S4 (d-1) and S5 (e-1) positions. Particle diameter size distribution of co-sputter Cu-Co sample at S1 (a-2), S2 (b-2), S3 (c-2), S4 (d-2) and S5 (e-2) positions

The particle distribution demonstrates that the particle uniformity with this film structure is not good, especially at position S4 and S5. S4 and S5 positions show a large particle size difference. From the histogram, we can observe that there are a large number of small particles (less than 20 nm) as well as larger ones (around 120 nm) show up at position S1. However, at positions S2, S3, S4 and S5, the majority of particles are smaller than 20 nm.

Additionally, all the SEM images shown above were analyzed by ImageJ software to collect the average particle size for each sample at five positions. They are presented

in Table 3.4. The scatter plot in Figure 3.20 also provides a much easier way for particle size comparison and further analysis.

Table 3.4 Average particle diameter at position S1, S2, S3, S4 and S5 of co-sputter, Co top Cu bottom and Cu top Co bottom thin films on SiO_2 substrates

position	S1	S2	S3	S4	S5
Co-sputter particle dia. (nm)	57	92	53	76	58
Co top Cu bottom particle dia. (nm)	103	73	109	93	102
Cu top Co bottom particle dia. (nm)	93	62	65	84	58

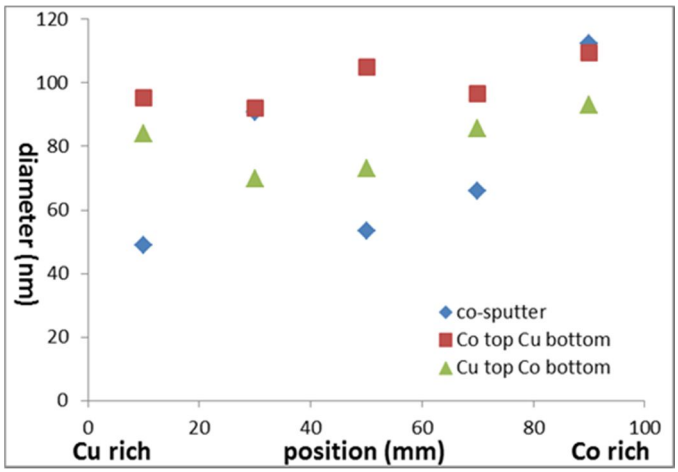

Figure 3.20 Scatter plot of average particle diameter at position S1, S2, S3, S4 and S5 of co-sputter, Co top Cu bottom and Cu top Co bottom thin films on SiO_2 substrates

Different Cu-Co thin film structure shows a large difference in particle size. For instance, at position S1, S3 and S5, particles with “Co top Cu bottom” structure are almost twice as big as those with co-sputter structure. If we compare the particle size at each position with the same thin film structure, it is not regularity either. Figure 3.20 reveals that particles with “Co top Cu bottom” structure are in general a little

bigger than those with other structures.

3.2.2 Optical characterization of Cu-Co thin films

The reflectance, absorbance and transmittance (T%) of Cu-Co thin films was measured by Filmetrics F20-UV thin film analyzer between 200 to 900 nm wavelengths while the transmission and absorption were measured by Cary 5000 (Varian Inc.) from 300 nm to 1000 nm at each position.. All the results were compared with pure Cu and Co films.

3.2.2.1 Reflectance of Cu-Co thin films

Figure 3.21 shows the detail information about the reflectance at all five positions of each sample. Furthermore, the reflectance of the three samples at same position is also compared in Figure 3.22.

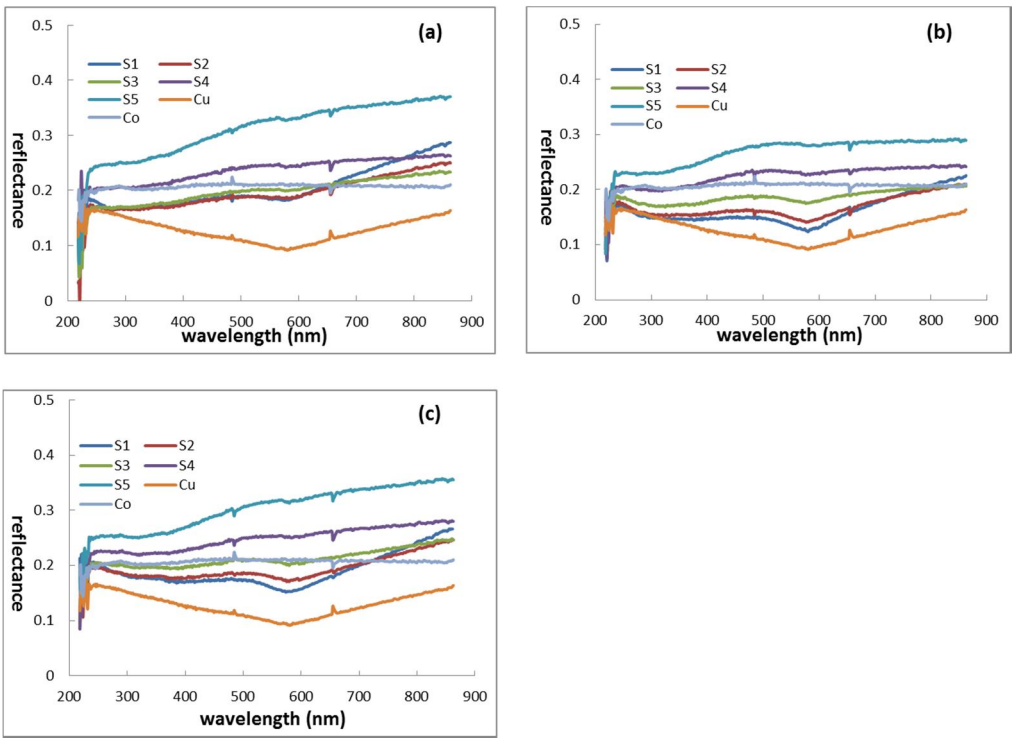

Figure 3.21 Reflectance of co-sputter (a), Co top Cu bottom (b) and Cu top Co bottom (c) Cu-Co thin films on quartz at five positions compared with pure Cu and Co

All the three graphs demonstrate that the reflectance is decreasing in the order of S5, S4, S3, S2 and S1 in visible wavelength. Pure Cu thin film has a lowest reflectance in all the three graphs. But the reflectance of pure Co is in between that of the others.

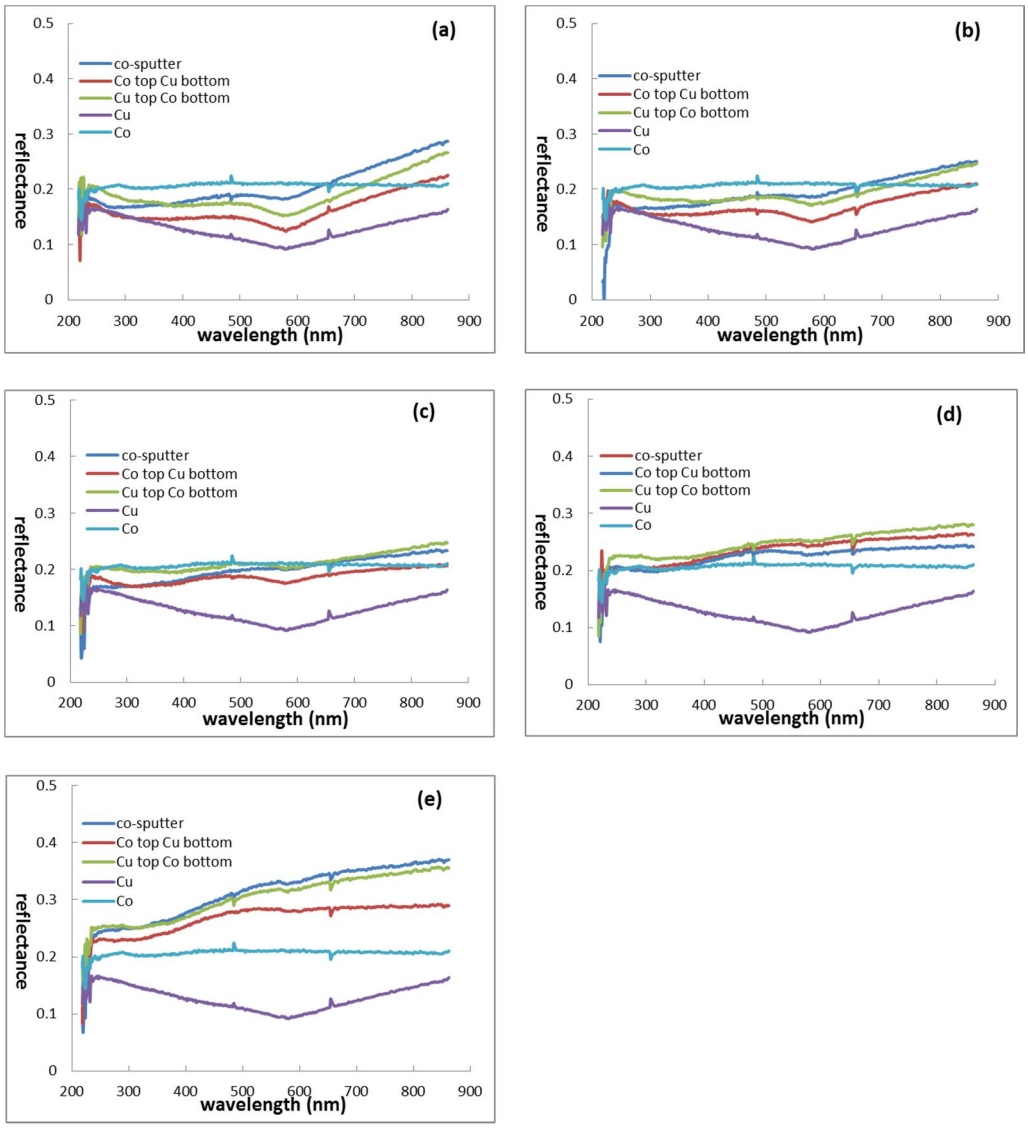

Figure 3.22 Reflectance of pure Cu, Co and Cu-Co thin films on quartz at all five positions: S1 (a), S2 (b), S3 (c), S4 (d) and S5 (e)

In Figure 3.22, thin films with co-sputter structure show an increased reflectance compared with that having "Cu top Co bottom" structure while the reflectance of Cu-Co thin films with "Co top Cu bottom" structure is lower than that with other two structures at positions S1, S2 and S5. At position S3, "Co top Cu bottom" structure shows a lower reflectance than other two structures. And at position S4, the reflectance is increasing in the order of "Co top Cu bottom", "co-sputter" and "Cu top Co bottom" structures.

3.2.2.2 Transmittance of Cu-Co thin films

Figure 3.23 compares the transmittance at all five positions of each sample. Furthermore, the transmittance of the three samples at same position is also shown in Figure 3.24.

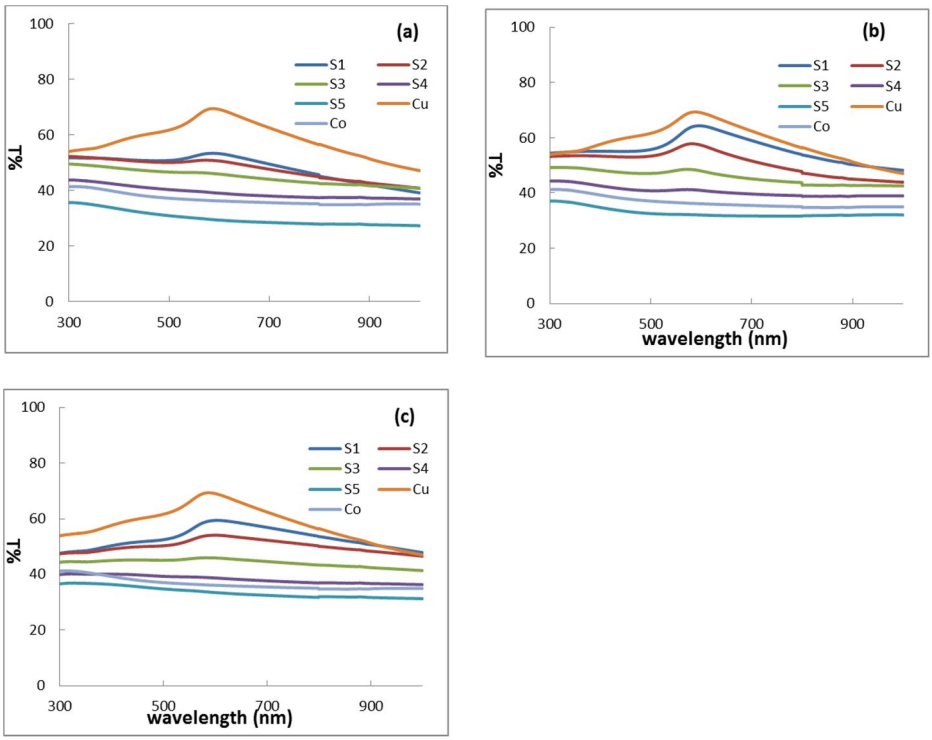

Figure 3.23 Transmittance of co-sputter (a), Co top Cu bottom (b) and Cu top Co bottom (c) Cu-Co thin films on quartz at five positions compared with pure Cu and Co

Figure 3.25 reveals that the transmittance is decreasing in the order of pure Cu, S1,S2, S3, S4, pure Co and S1 for all three structures. With comparison to Co top Cu bottom and Cu top Co bottom structures, the three transmittance curves of S1, S2 and S3 are pretty close for co-sputtered thin film.

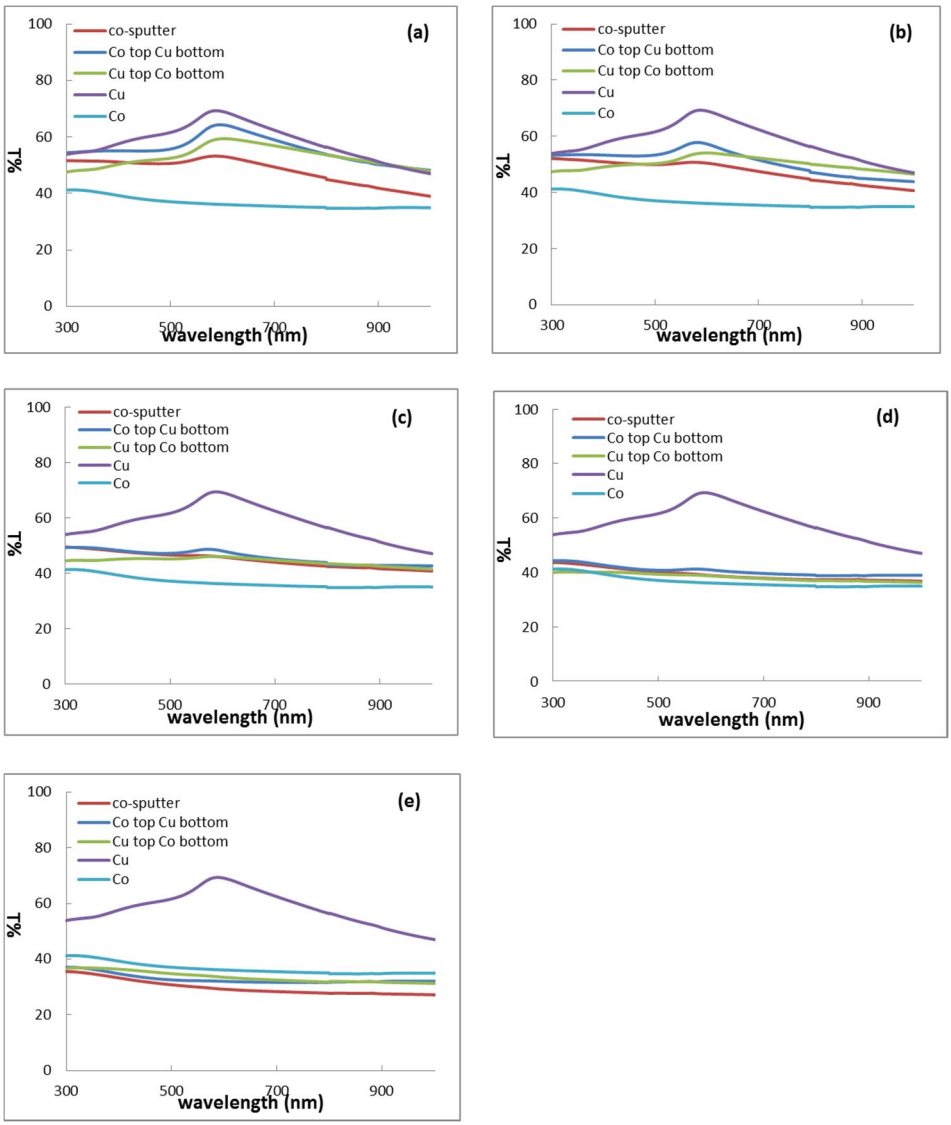

Figure 3.24 Transmittance of pure Cu, Co and Cu-Co thin films on quartz at all five positions: S1 (a), S2 (b), S3 (c), S4 (d) and S5 (e)

Figure 3.26 is transmittance of pure Cu, Co and Cu-Co thin films with co-sputter, Co top Cu bottom and Cu top Co bottom structures. In (a) and (b) co-sputtered film has a more flat curve than that of other two structures. It can also be observed that more light was transmitted through Co top Cu bottom structured film compared with co-sputtered film. And the curve of Cu top Co bottom intersects with these two. At position S3, S4 and S5, the transmittance of all three structures doesn't vary very much at different wavelength.

3.2.2.3 Absorbance of Cu-Co thin films

In this work, absorbance is defined as 1-T%-reflectance. Figure 3.25 shows the detail information about the absorbance at all five positions of each sample. Furthermore,

the absorbance of the three samples at same position is also compared in Figure 3.26.

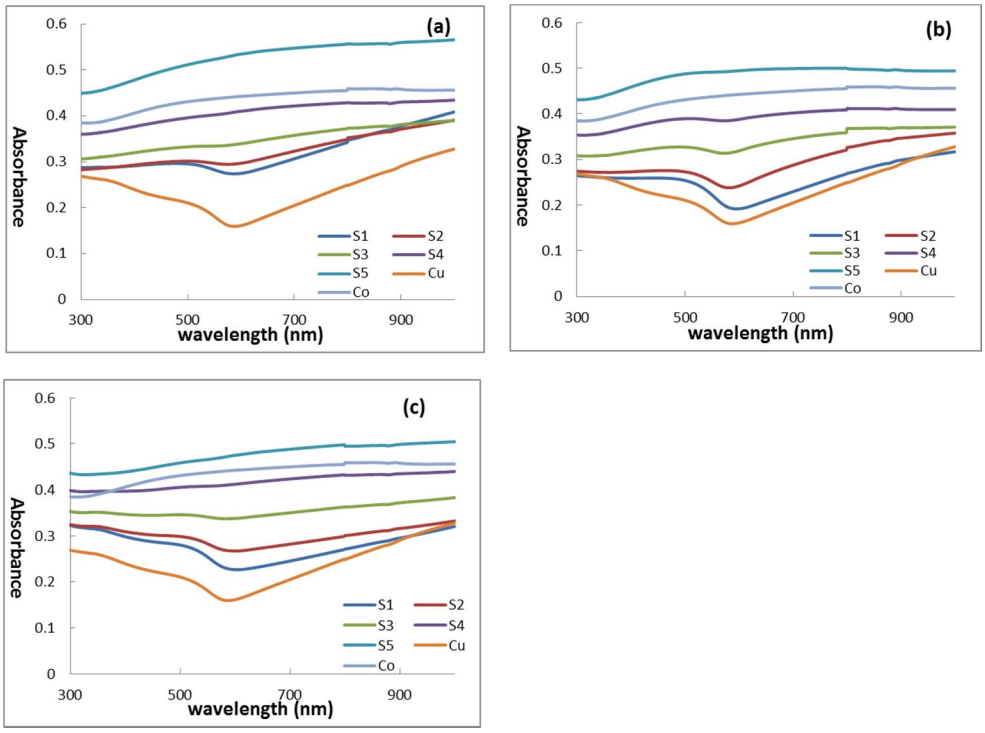

Figure 3.25 Absorbance of co-sputter (a), Co top Cu bottom (b) and Cu top Co bottom (c) Cu-Co thin films on quartz at five positions compared with pure Cu and Co

For all the three samples, position S5 has the highest absorbance while the other four absorbance curves are between pure Co and Cu as shown in Figure 3.25. The absorbance decreases in the order of S5, S4, S3, S2 and S1. Co-sputtered film has a more flat curve than that of other two structures. With comparison to Co top Cu bottom and Cu top Co bottom structures, the three curves of S1, S2 and S3 are pretty close for co-sputtered thin film.

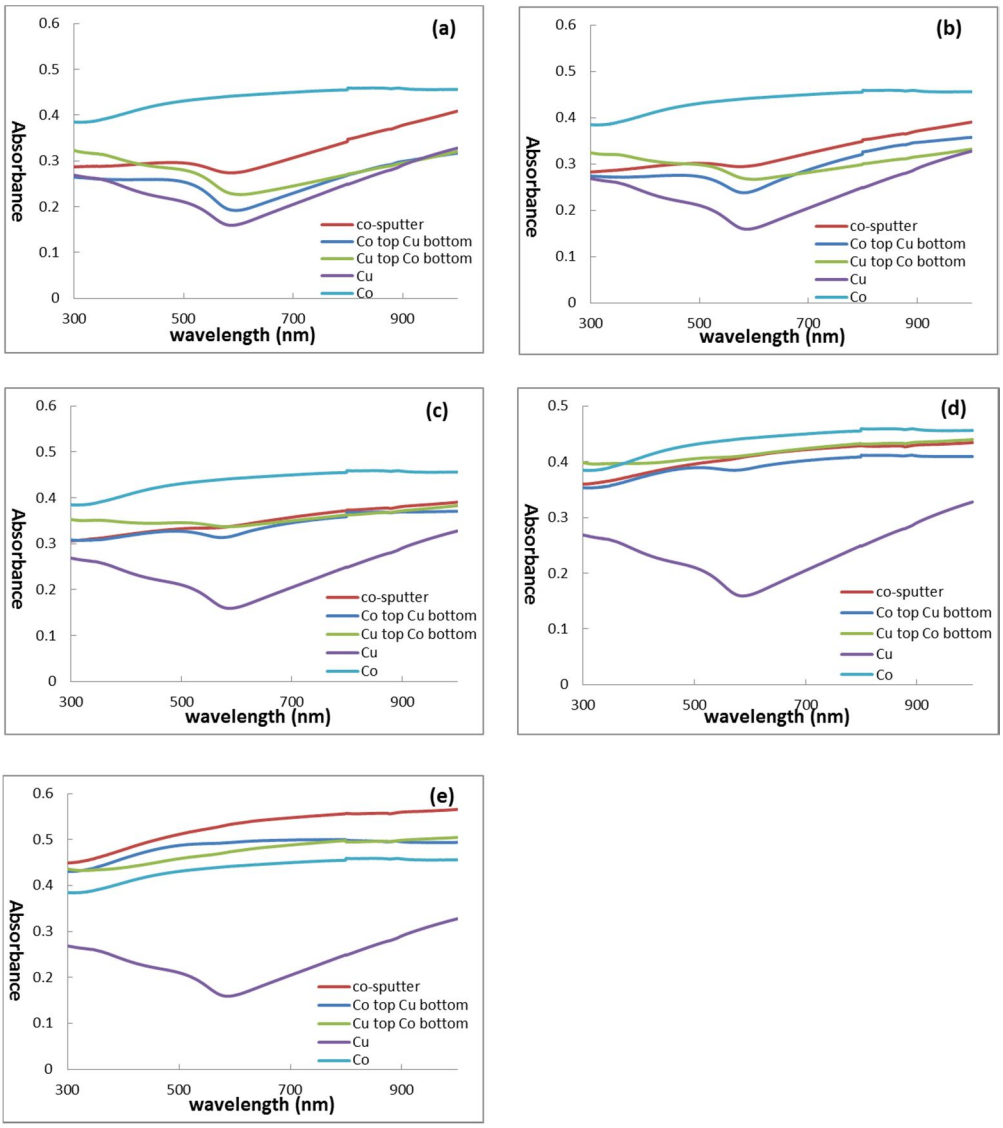

Figure 3.26 Absorbance of pure Cu, Co and Cu-Co thin films on quartz at all five positions: S1 (a), S2 (b), S3 (c), S4 (d) and S5 (e)

In Figure 3.26, the absorbance of Cu-Co thin films with all three structures is between that of pure Cu and Co at position S1, S2, S3 and S4. The co-sputtered Cu-Co thin film has a higher absorbance than that with Co top Cu bottom structure while the absorbance curve of Cu top Co bottom structure thin film intersects with other two for position S1 and S2. There is no big difference at position S3 and S4. At position S5, the absorbance of co-sputtered Cu-Co thin film is still higher than that of Co top Cu bottom thin film. However, thin film with Cu top Co bottom structure has a littler lower absorbance compared with other two. All these three curves are above Co curve.

3.2.3 Optical characterization of Cu-Co particles

The reflectance, absorbance and transmittance of Cu-Co particles was measured by Filmetrics F20-UV thin film analyzer between 200 to 900 nm wavelengths at different position while the transmission and absorption were measured by Cary 5000 (Varian Inc.) from 300 nm to 1000 nm at each position. All the results were compared with pure Cu and Co films.

3.2.3.1 Reflectance of Cu-Co particles

Figure 3.27 shows the detail information about the reflectance at all five positions of each sample. Furthermore, the reflectance of the three samples at same position is also compared in Figure 3.28.

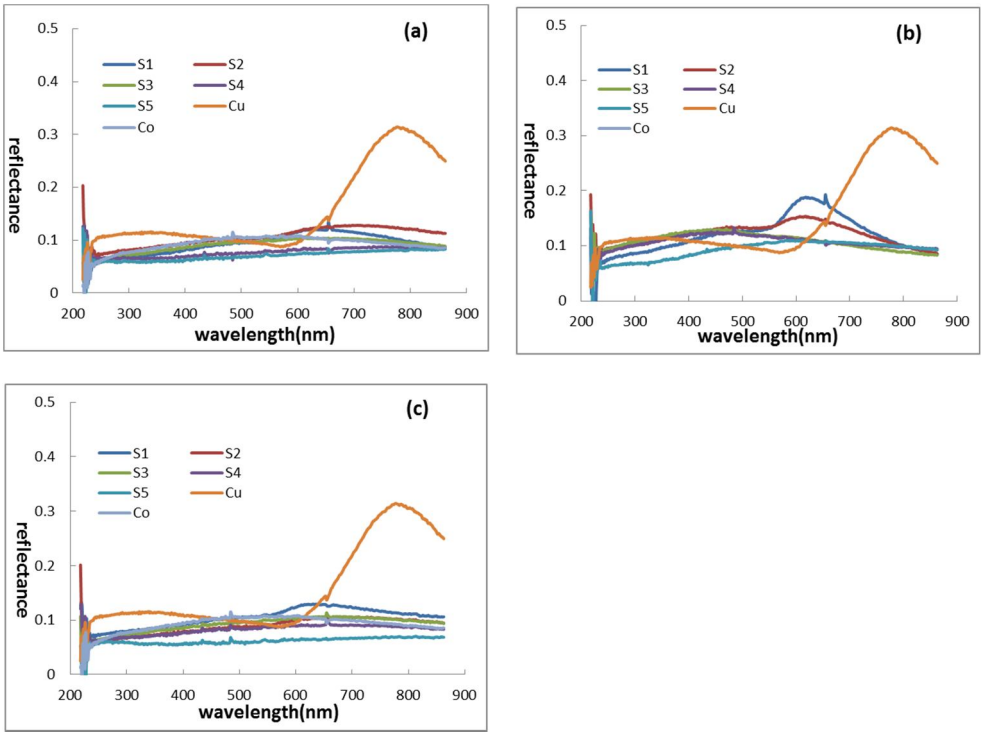

Figure 3.27 Reflectance of co-sputter (a), Co top Cu bottom (b) and Cu top Co bottom (c) Cu-Co particles on quartz at five positions compared with pure Cu and Co

Pure Cu reflectance curve shows a peak at around 800 nm wavelength. And the cure of pure Co is in between that of Cu-Co alloy particles. Particles with co-sputter and "Cu top Co bottom" structures have relatively flat reflectance curves at all five positions. Whereas, the graphs of Co top Cu bottom Cu-Co particles with Co top Cu bottom structure display a small reflectance peak around 600 nm wavelength at both S1 and S2 positions. And the peak of position S1 is a little stronger than that of position S2.

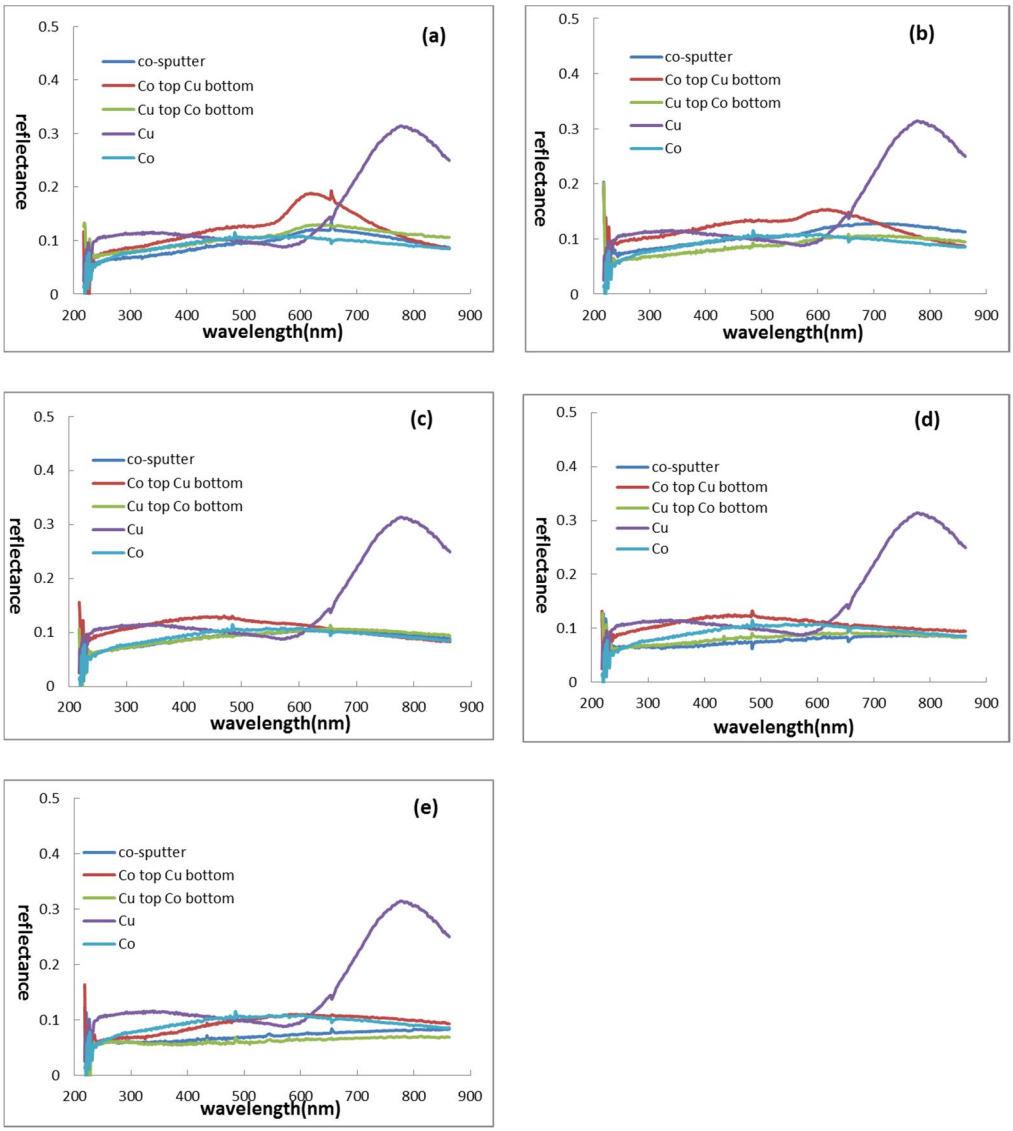

Figure 3.28 Reflectance of pure Cu, Co and Cu-Co particles on quartz at all five positions: S1 (a), S2 (b), S3 (c), S4 (d) and S5 (e).

At all the five positions, the reflectance of particles with co-sputter and Cu top Co bottom structures is pretty close. Both of them are lower than that of Co top Cu bottom samples at the wavelength from 200 nm to 700 nm.

3.2.3.2 Absorbance of Cu-Co particles

Figure 3.29 shows the absorbance of Cu-Co particles at all five positions of each sample. Additionally, the absorbance of particles with three structures at same position is also compared in Figure 3.30.

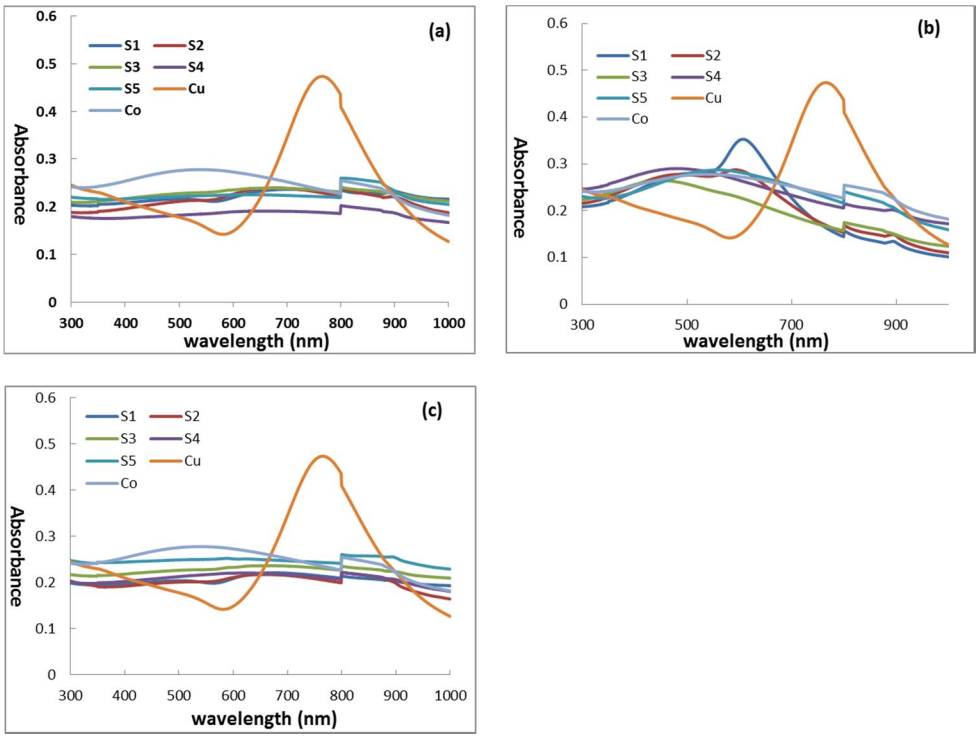

Figure 3.29 Absorbance of co-sputter (a), Co top Cu bottom (b) and Cu top Co bottom (c) Cu-Co particles on quartz at five positions compared with pure Cu and Co

In Figure 3.29, Cu shows an absorbance peak around 800 nm wavelength. For particles with Co top Cu bottom structure, there is also a small absorbance peak at around 600 nm wavelength at position S1. And position shows a tiny peak around the same wavelength. At position S3, S4 and S5, the absorbance increases a little bit and then decrease with increasing the wavelength. Curves of particles with co-sputter and Cu top Co bottom structures are quite flat.

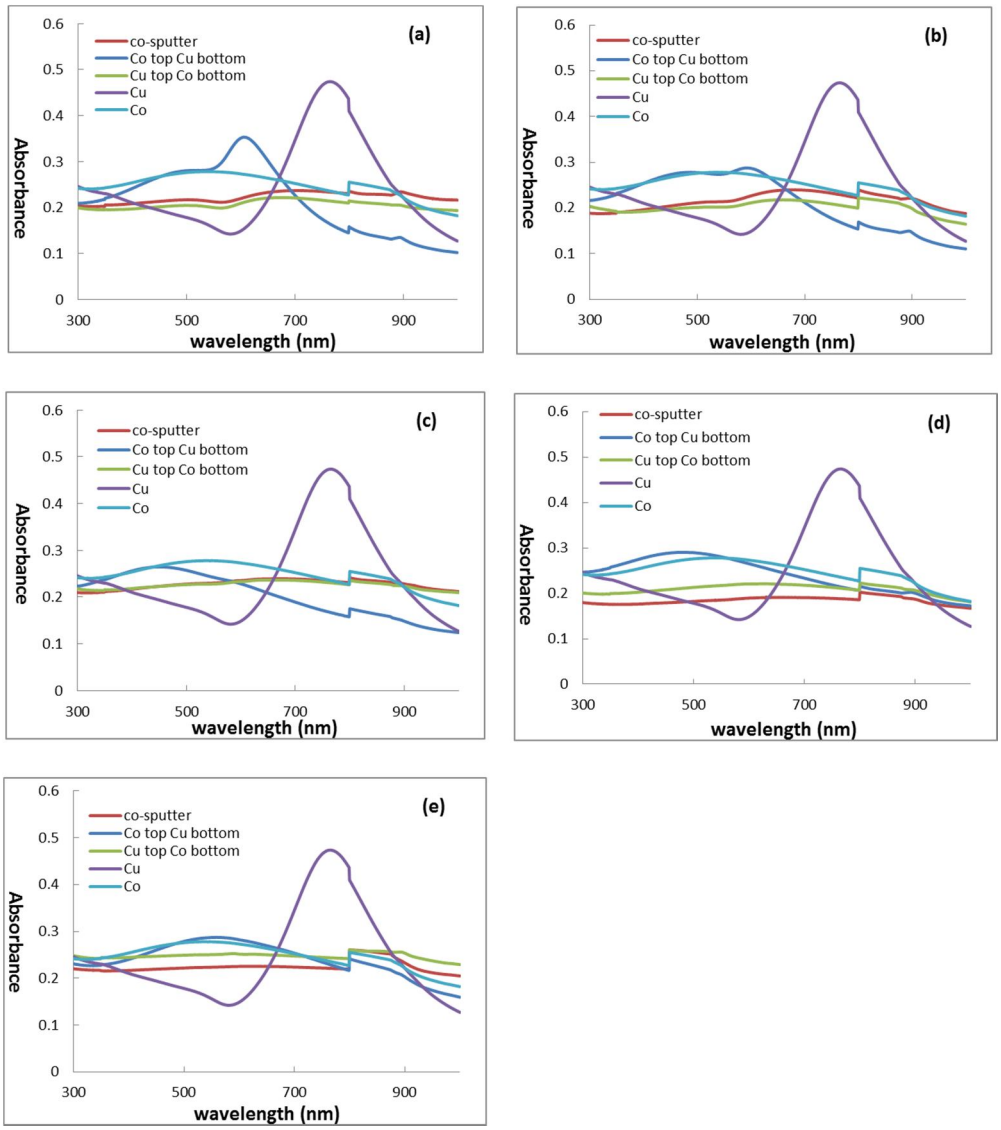

Figure 3.30 Absorbance of pure Cu, Co and Cu-Co particles on quartz at all five positions: S1 (a), S2 (b), S3 (c), S4 (d) and S5 (e)

Particles with Co top Cu bottom structure have an absorbance peak around 600 nm at position S1 and S2. Other two structures don't show any increase at this wavelength.

3.2.3.3 Transmittance of Cu-Co particles

Figure 3.31 and Figure 3.32 are the transmittance curves of Cu-Co particles with three different deposition procedure. They are compared with pure Cu and Co particles.

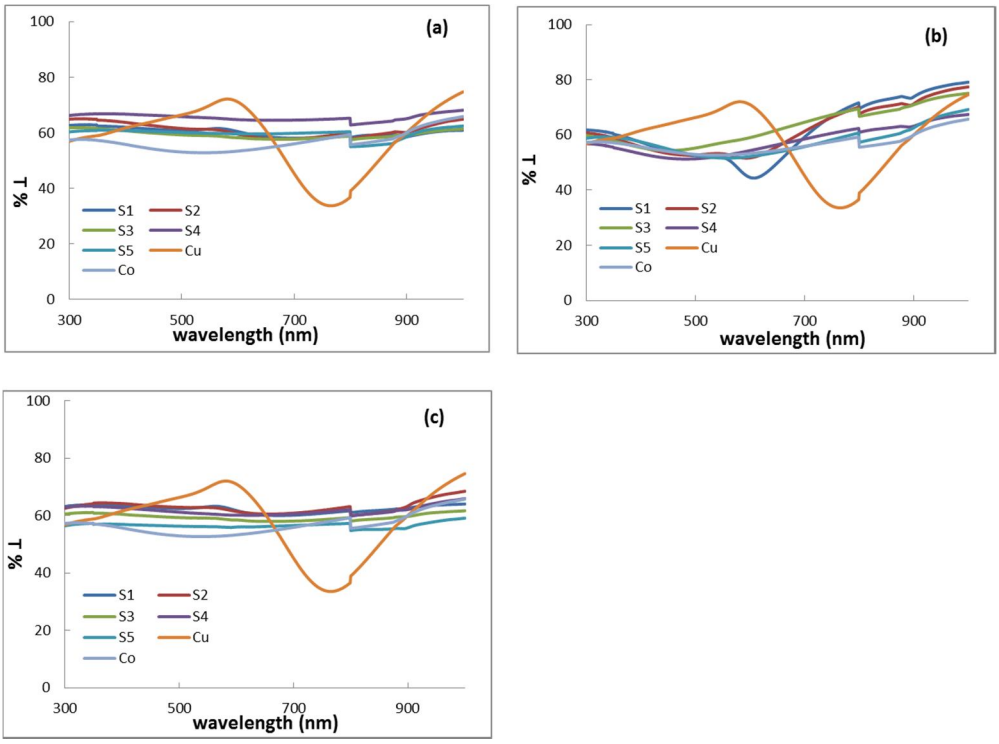

Figure 3.31 Transmittance of co-sputter (a), Co top Cu bottom (b) and Cu top Co bottom (c) Cu-Co particles on quartz at five positions compared with pure Cu and Co

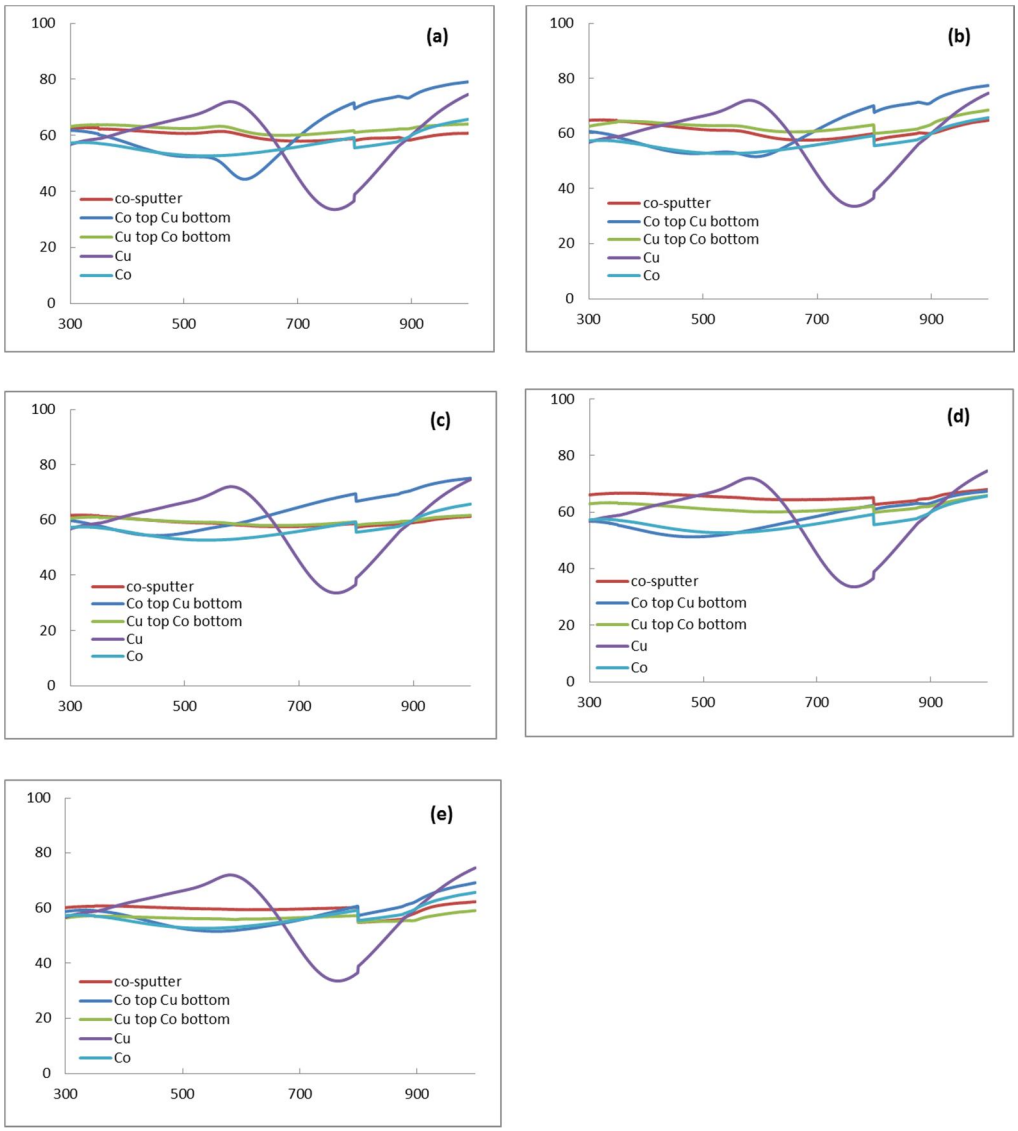

Figure 3.32 Transmittance of pure Cu, Co and Cu-Co particles on quartz at all five positions: S1 (a), S2 (b), S3 (c), S4 (d) and S5 (e)

In Figure 3.31 and 3.32, only Co top Cu bottom samples shows a transmission decrease at position S1 and S2.

3.3 Optical properties comparison between Cu-Co thin films and particles on quartz substrates

Reflectance, absorbance and transmittance of bother Cu-Co thin films and particles were compared in this section.

3.3.1 Reflectance comparisons between thin film and particles

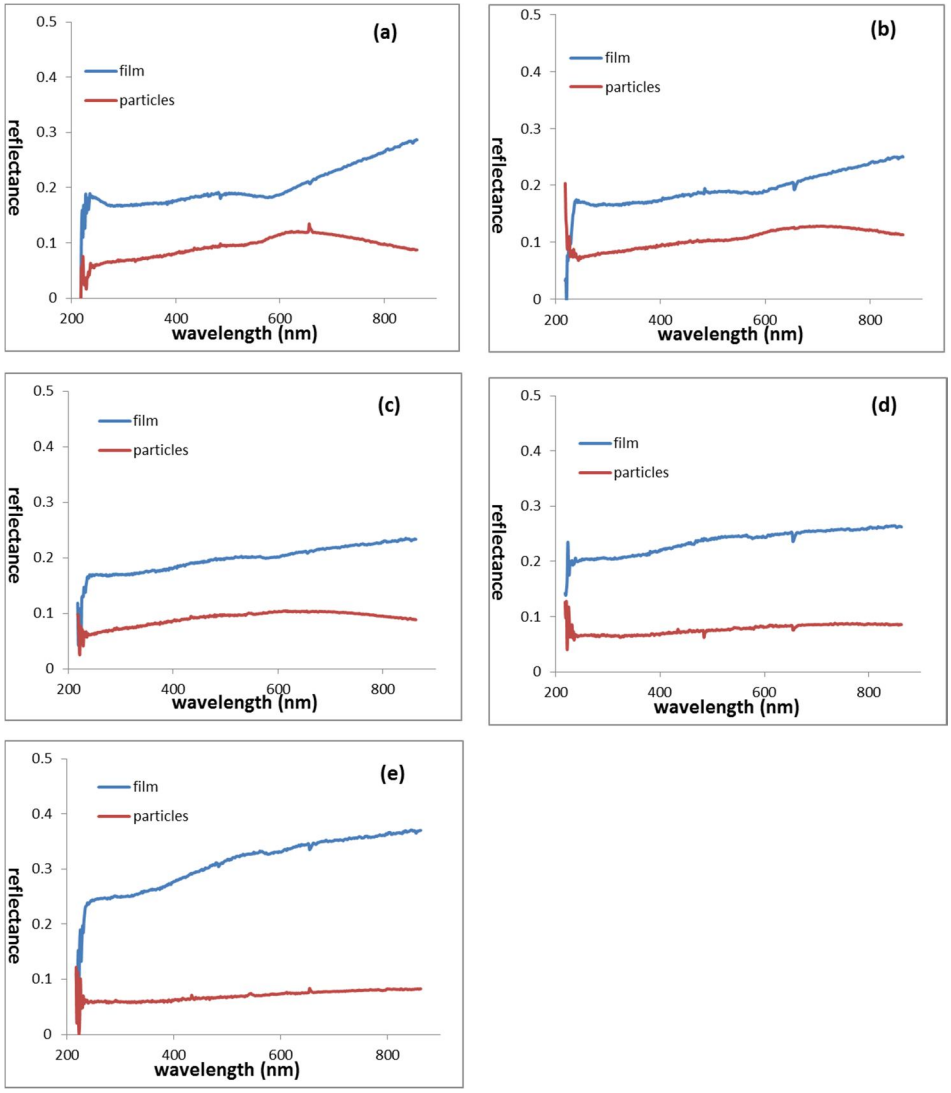

Figure 3.33 Reflectance of thin film and particles of co-sputtered Cu-Co on quartz substrate at position S1 (a), S2 (b), S3 (c), S4 (d) and S5 (e)

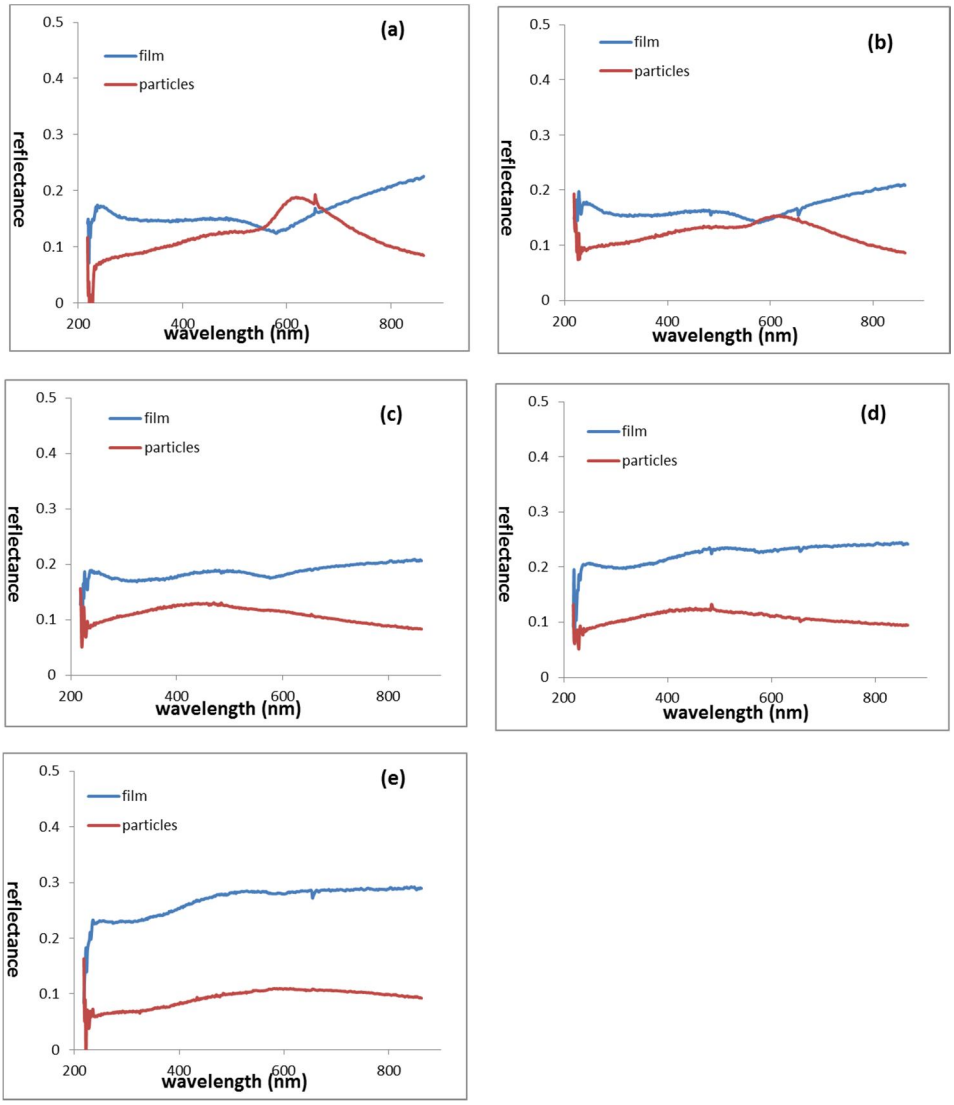

Figure 3.34 Reflectance of thin film and particles of Co top Cu bottom structured Cu-Co on quartz substrate at position S1 (a), S2 (b), S3 (c), S4 (d) and S5 (e)

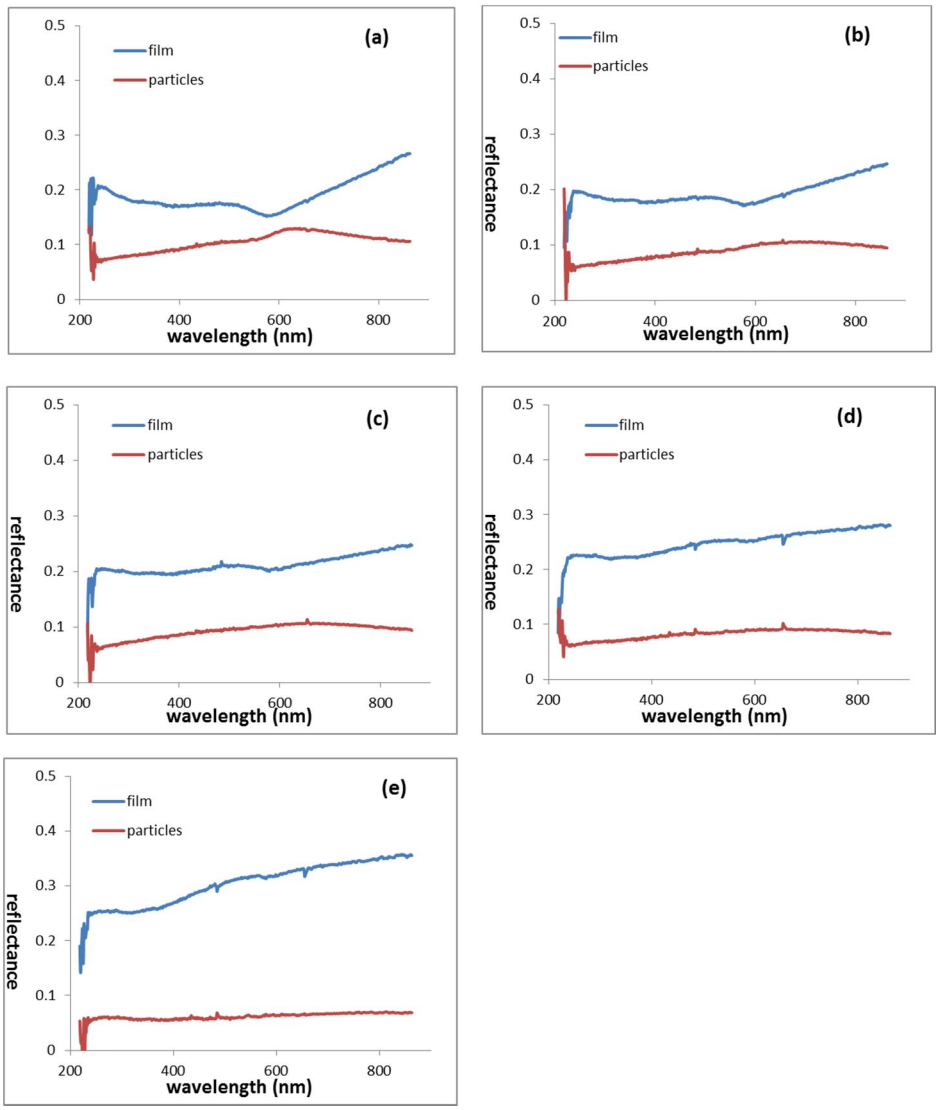

Figure 3.35 Reflectance of thin film and particles of Cu top Co bottom structured Cu-Co on quartz substrate at position S1 (a), S2 (b), S3 (c), S4 (d) and S5 (e)

Figure 3.34 shows that reflectance of Co top Cu bottom structured particles increases at around 600 nm wavelength at position S1 and S2. And the peak of S1 is much bigger than that of S2. There is also a tiny increase of reflectance of Cu top Co bottom structured particles at position S1 shown in Figure 3.35. For all other positions, particles have higher reflectance than that of thin films at every wavelength. And their reflectance curves are quite flat.

3.3.2 Absorbance comparisons between thin film and particles

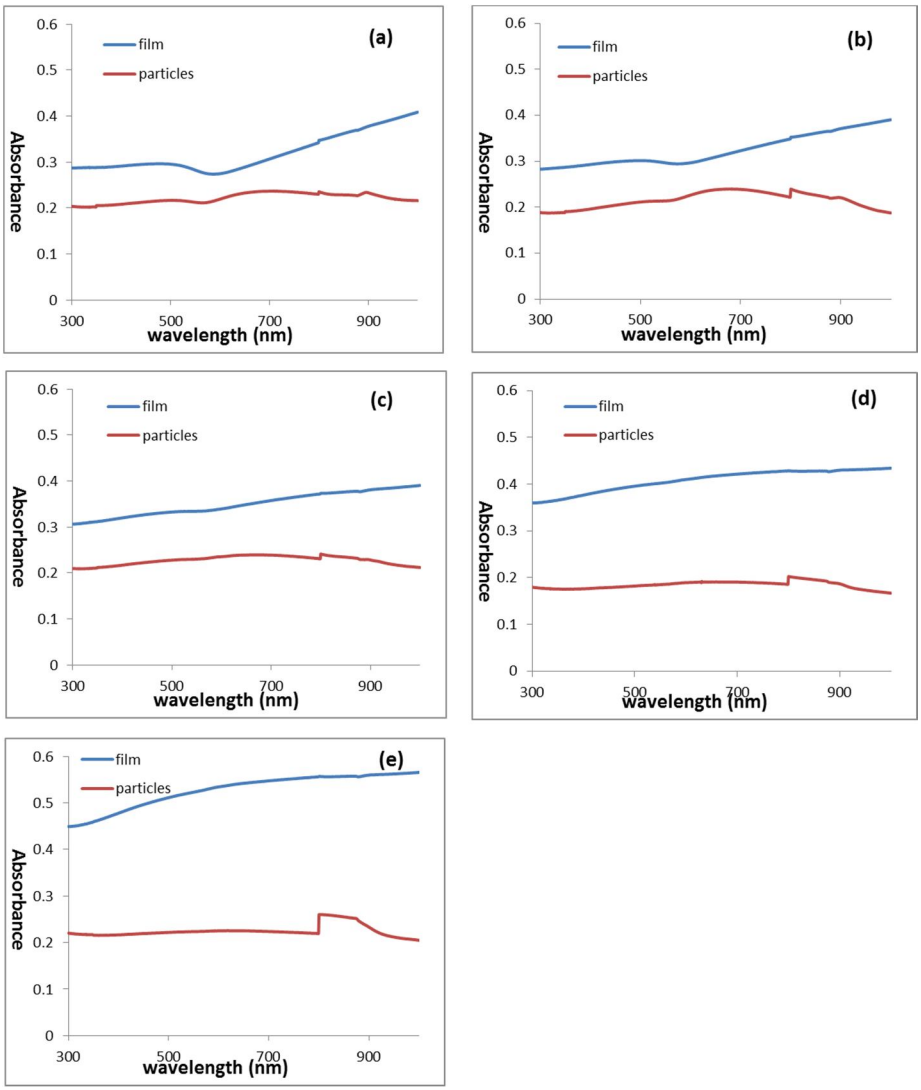

Figure 3.36 Absorbance of thin film and particles of co-sputtered Cu-Co on quartz substrate at position S1, S2, S3, S4 and S5

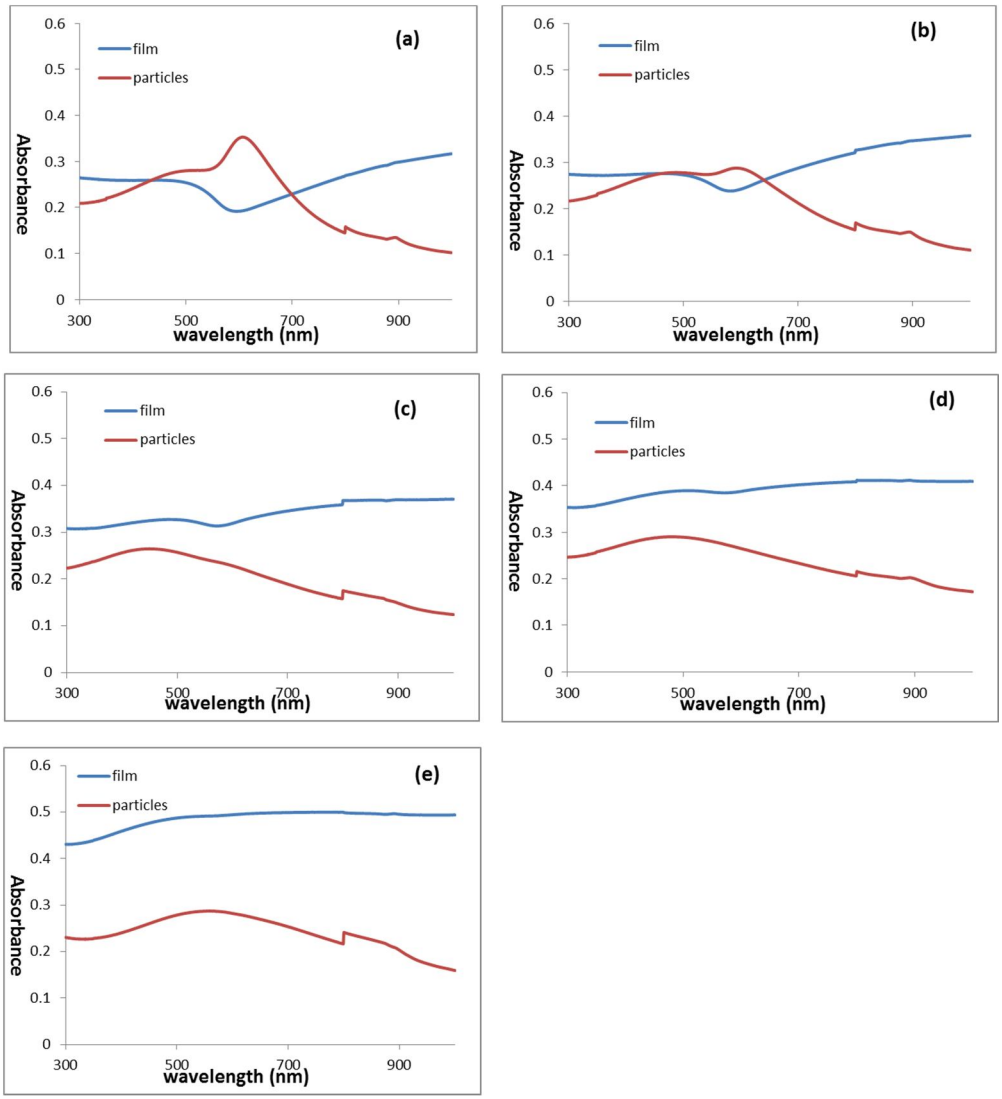

Figure 3.37 Absorbance of thin film and particles of Co top Cu bottom structured Cu-Co on quartz substrate at position S1, S2, S3, S4 and S5

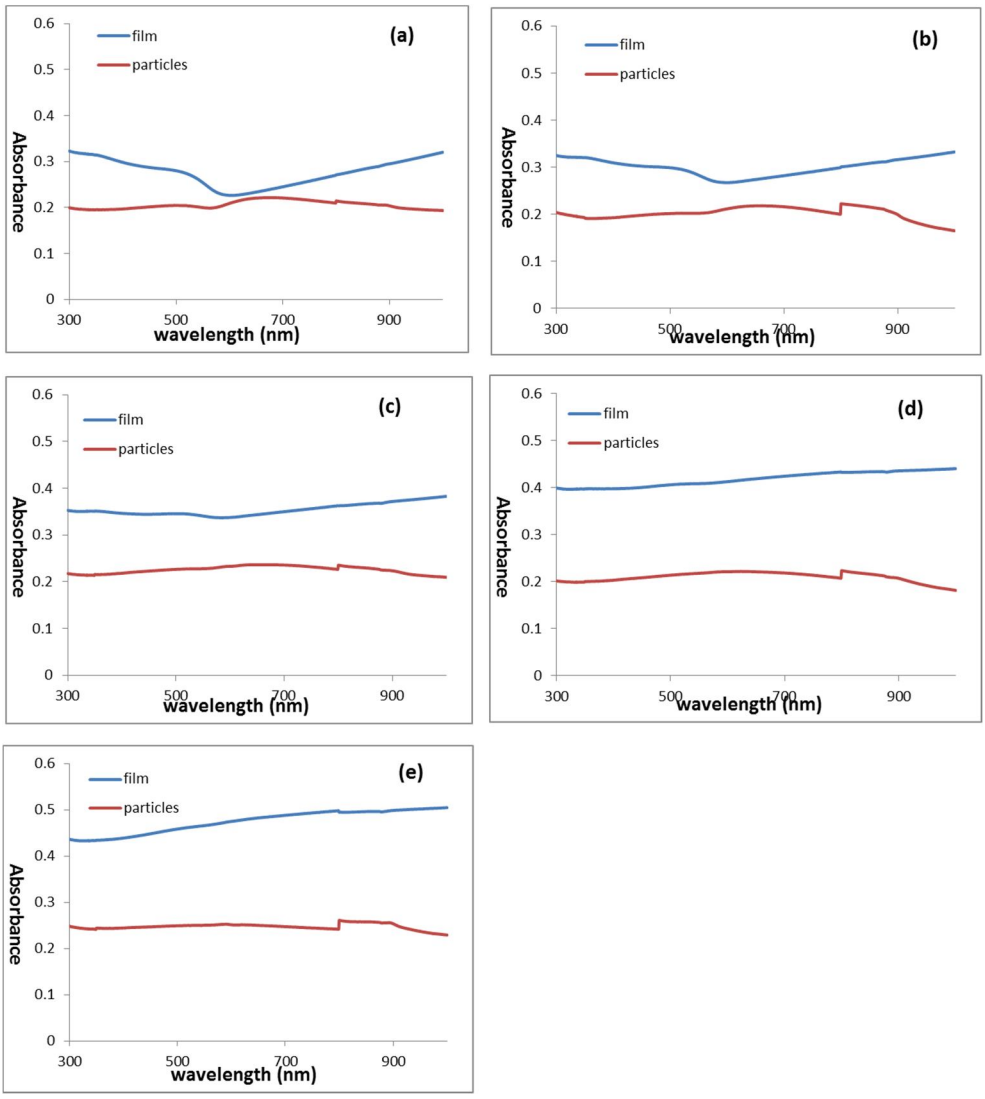

Figure 3.38 Absorbance of thin film and particles of Cu top Co bottom structured Cu-Co on quartz substrate at position S1, S2, S3, S4 and S5

Figure 3.37 shows that absorbance of Co top Cu bottom structured particles increases at around 600 nm wavelength at position S1 and S2. And the peak of S2 is much weaker than that of S1. After that, it damps quickly. For all other positions, particles have lower absorbance than that of thin films at every wavelength. And there is no absorbance peak exists.

3.3.3 Transmittance comparisons between thin film and particles

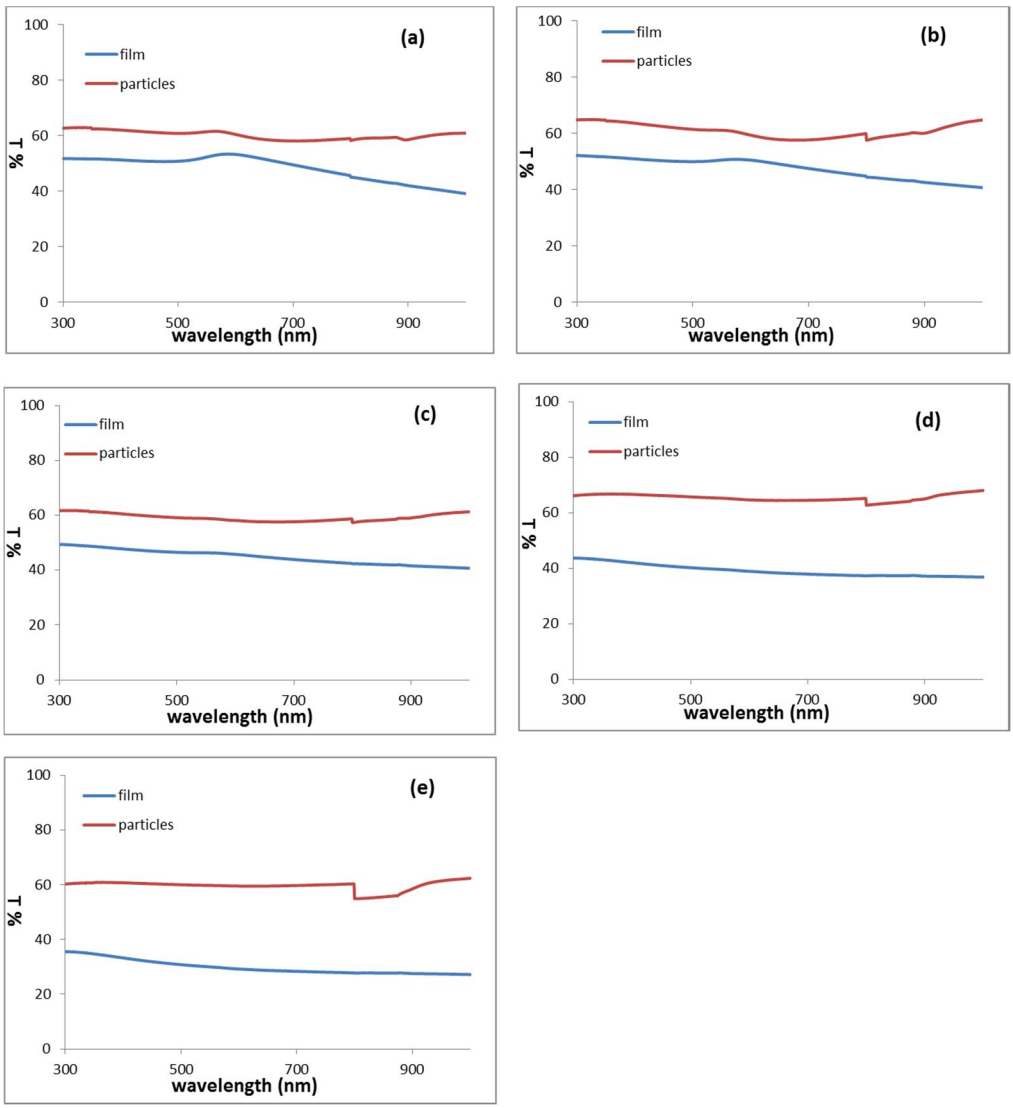

Figure 3.39 Transmittance of thin film and particles of co-sputtered Cu-Co on quartz substrate at position S1, S2, S3, S4 and S5

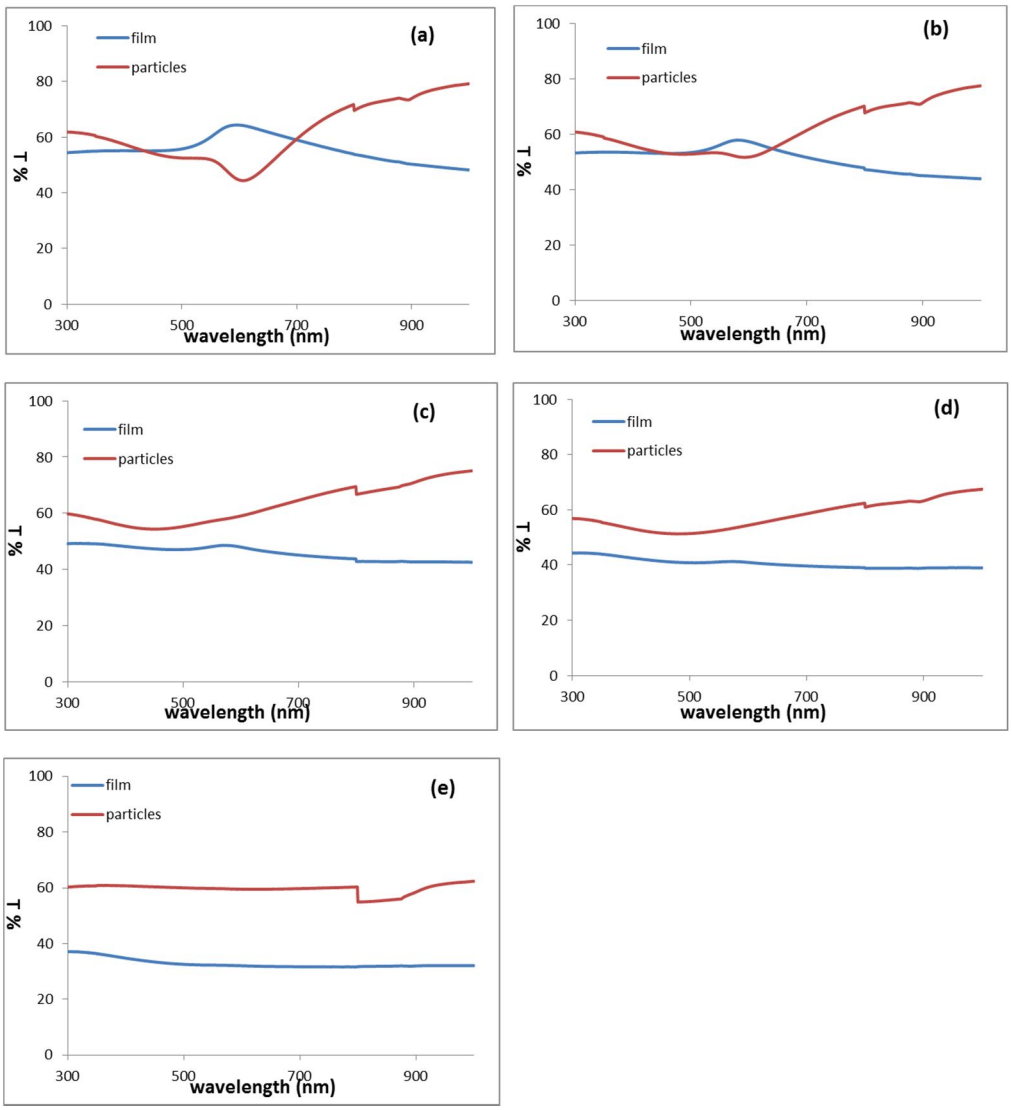

Figure 3.40 Transmittance of thin film and particles of Co top Cu bottom structured Cu-Co on quartz substrate at position S1, S2, S3, S4 and S5

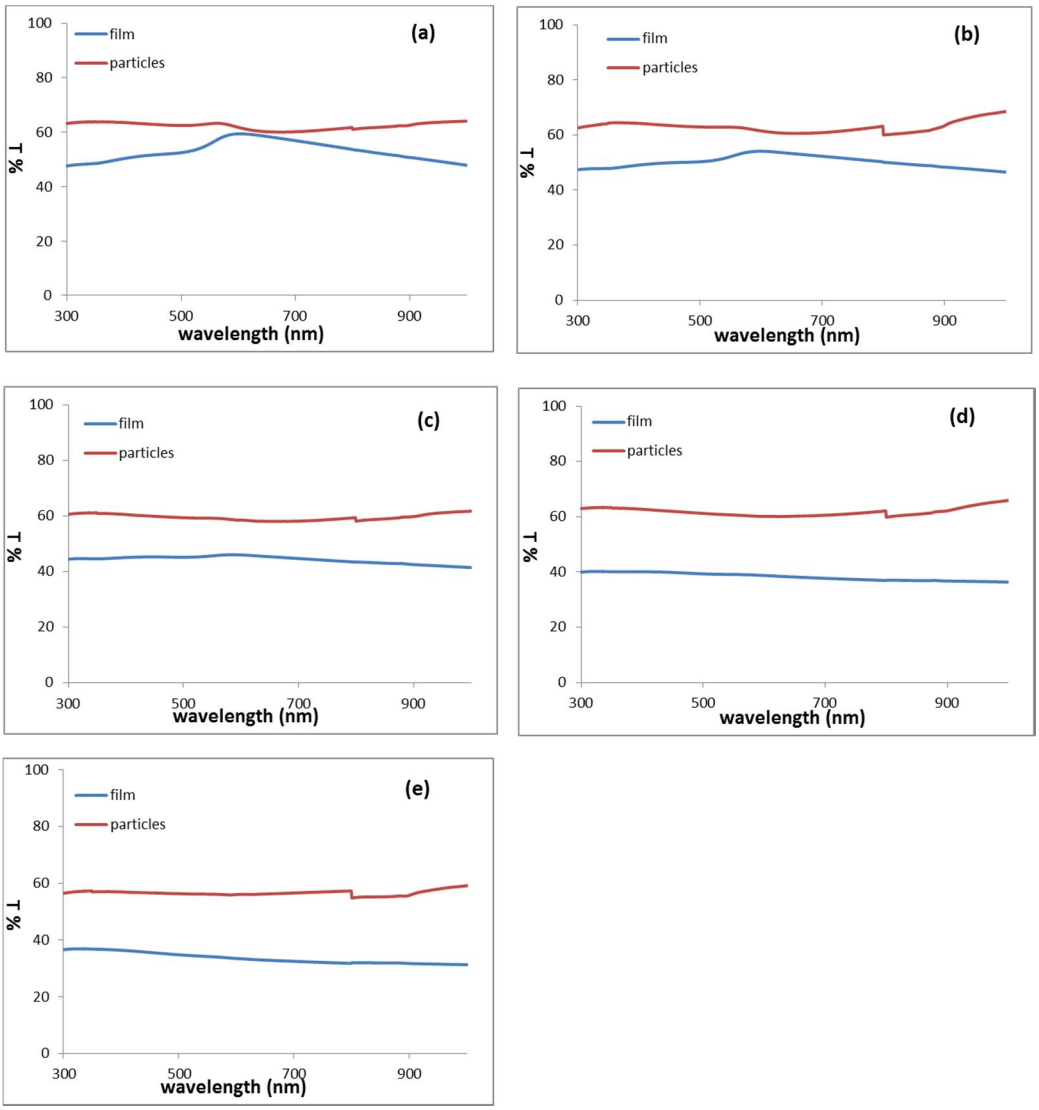

Figure 3.41 Transmittance of thin film and particles of Cu top Co bottom structured Cu-Co on quartz substrate at position S1, S2, S3, S4 and S5

From Figure 3.39, 3.40 and 3.41, we can observe that more light transmitted through particles than thin film except S1 and S2 of Co top Cu bottom structured samples. In Figure 3.40 (a) and (b), the transmittance of particles decreases at visible wavelength.

CHAPTER 4 DISCUSSION

4.1 Cu-Co phase diagram

4.1.1 Equilibrium and non-equilibrium solidification

The free energy of any phase is a function of pressure, temperature, and composition. Equilibrium is attained when the Gibbs free energy is at a minimum, that is:

$$\mathrm{dG}(\mathrm{P},\mathrm{T},n_{i\ldots}) = (\frac{\partial G}{\partial T})_{P,n_{i}\ldots}dT + (\frac{\partial G}{\partial P})_{T,n_{i}\ldots}dP + (\frac{\partial G}{\partial n_i})_{T,P\ldots}dn_i + \cdots = 0 \qquad (4.1)$$

where n_i is the number of moles of component i. The potential derivatives of the free energy are called partial molar free energies, or chemical potentials:

$$\mu_i = (\frac{\partial G}{\partial n_i})_{T,P,n_{i}\ldots} \qquad (4.2)$$

At equilibrium, and assuming T, P=constant,

$$\mathrm{dG} = \mu_i dn_i + \mu_j dn_j + \cdots = 0 \qquad (4.3)$$

If the cooling rate is extremely slow, or species diffusion rate is very fast, equilibrium solidification can be reached. And a homogeneous solid phase is formed.

However, when the solidification is under a fast cooling rate, diffusion is insufficient to homogenize the composition simultaneously during the process which is called non-equilibrium solidification.

4.1.2 Solidification of Cu-Co system

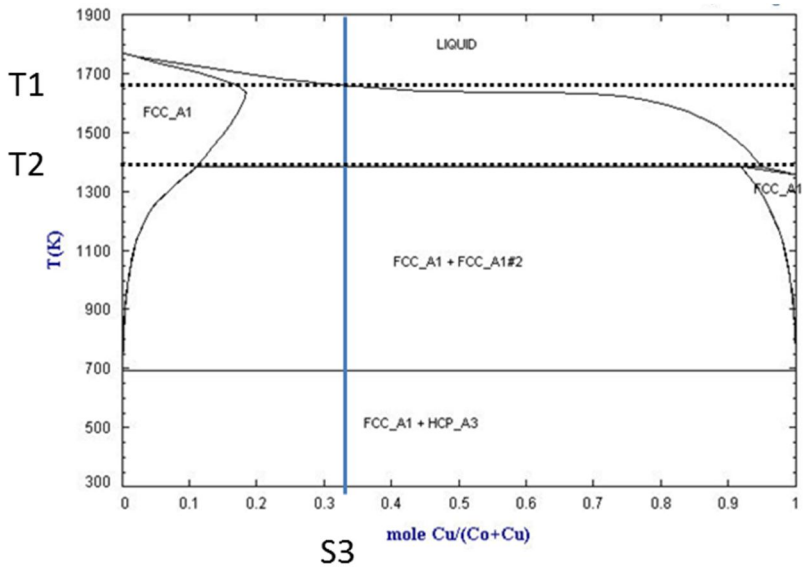

Figure 4.1 Phase diagram of Cu-Co binary system

For our Cu-Co thin films, the Cu atomic composition at the center (position S3) is ~35% which is labeled as the blue line shown in Figure 4.1. After laser irradiation, thin films with ~35% Cu were melted into liquid quickly. Based on the phase diagram, as the temperature decreases, Co-rich material solidifies first at T1 because of the higher melting temperature of Co. For a non-equilibrium (fast) cooling a Co-rich nuclei form which will be surrounded by liquid phase matrix. On further cooling to T2, an outer shell with different element composition is formed surrounding Co-core. This final particle structure is like the left cored structure shown in Figure 4.2. At the center, Co has a higher atomic percentage than the outer shell.

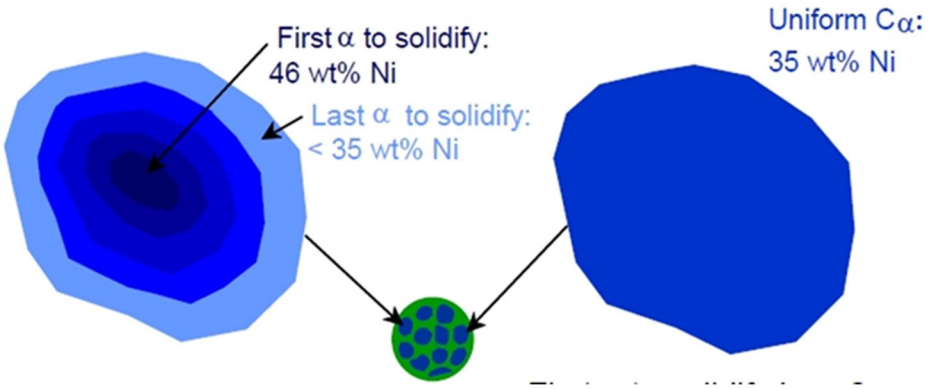

Figure 4.2 equilibrium and non-equilibrium solidification of Cu-Ni binary system

However, if the cooling rate is pretty slow, an equilibrium structure will be obtained. Therefore the composition of Cu-Co nano-particle from center to surface is quite uniform as shown in Figure 4.2. Different structure has different effect on the materials characters such as crystal lattice and mechanical properties.

4.2 Laser heating and cooling curve

The simulated laser heating curves of temperature vs. time show that the heating and cooling rates are all fast. Based on these simulations, Cu-Co thin films melt into liquid quickly. After laser irradiation, the liquid also cools and re-solidifies fairly fast. Since Co (1768K) has a much higher melting temperature than Cu (1358K), we can expect that Cu shows a longer liquid time than that of Co, which agrees with the simulation results of Cu and Co melting and cooling curves shown in Figure 4.3. Both the melting temperature and liquid time affects the nano-particle distribution after laser irradiation. The histograms of particles distribution in experimental results section illustrate the distribution variation with different compositions and a constant laser fluence.

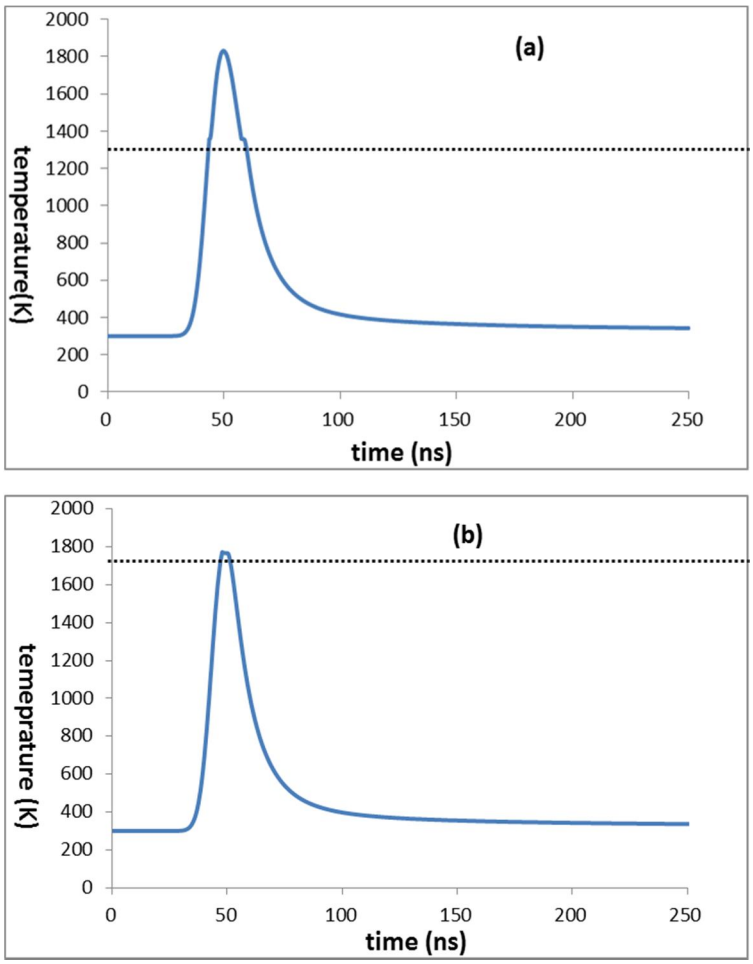

Figure 4.3 1D surface temperature vs. time simulation results of 10 nm Cu (a) and Co (b) thin film on 100 nm SiO_2/Si wafer (assume no lateral thermal diffusion)

4.3 Film and particle composition as function of position

The EDS results show that the average composition of Cu atom is nearly linearly dependent to the sample surface position which agrees with our simulation result which is shown in Figure 4.4. According to the EDS measurement and the simulation data, there is no significant difference in the Cu at.% at each position. Therefore, we can assume that there is little preferential evaporation or diffusion as a result of the laser irradiation.

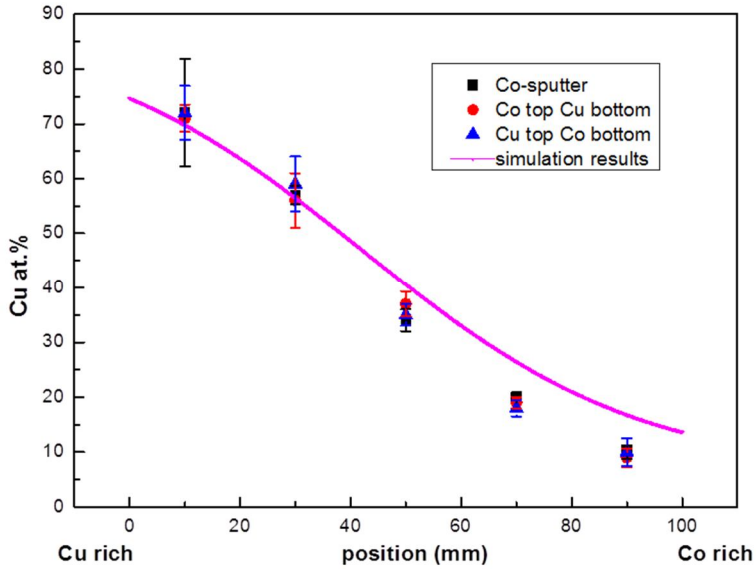

Figure 4.4 Experiment and simulation result of Cu at.% at different positions

4.4 Dewetting as a function of film structure and composition

Figure 3.7, 3.8 and 3.9 shows the SEM images of Cu-Co particles of three structures after pulsed laser irradiation on SiO_2 substrates. Particles are on the substrates with a contact angle θ_C which can be described by Young's Equation:

$$\gamma_{SG} = \gamma_{SL} + \gamma_{LG} cos\theta_C \tag{4.1}$$

where $\gamma_{LG}, \gamma_{SL}, \gamma_{SG}$ are interfacial tensions between liquid-gas medium, solid-liquid medium and solid-gas medium. θ_C is contact angle.

The dominant dewetting mechanism of Cu-Co thin films studied here is attributed to the spinodal dewetting process because each structured thin films and have a correlated particle size and spacing as illustrated in Figure 4.5. The spinodal dewetting breakup process evolves via the amplification of surface instability waves.

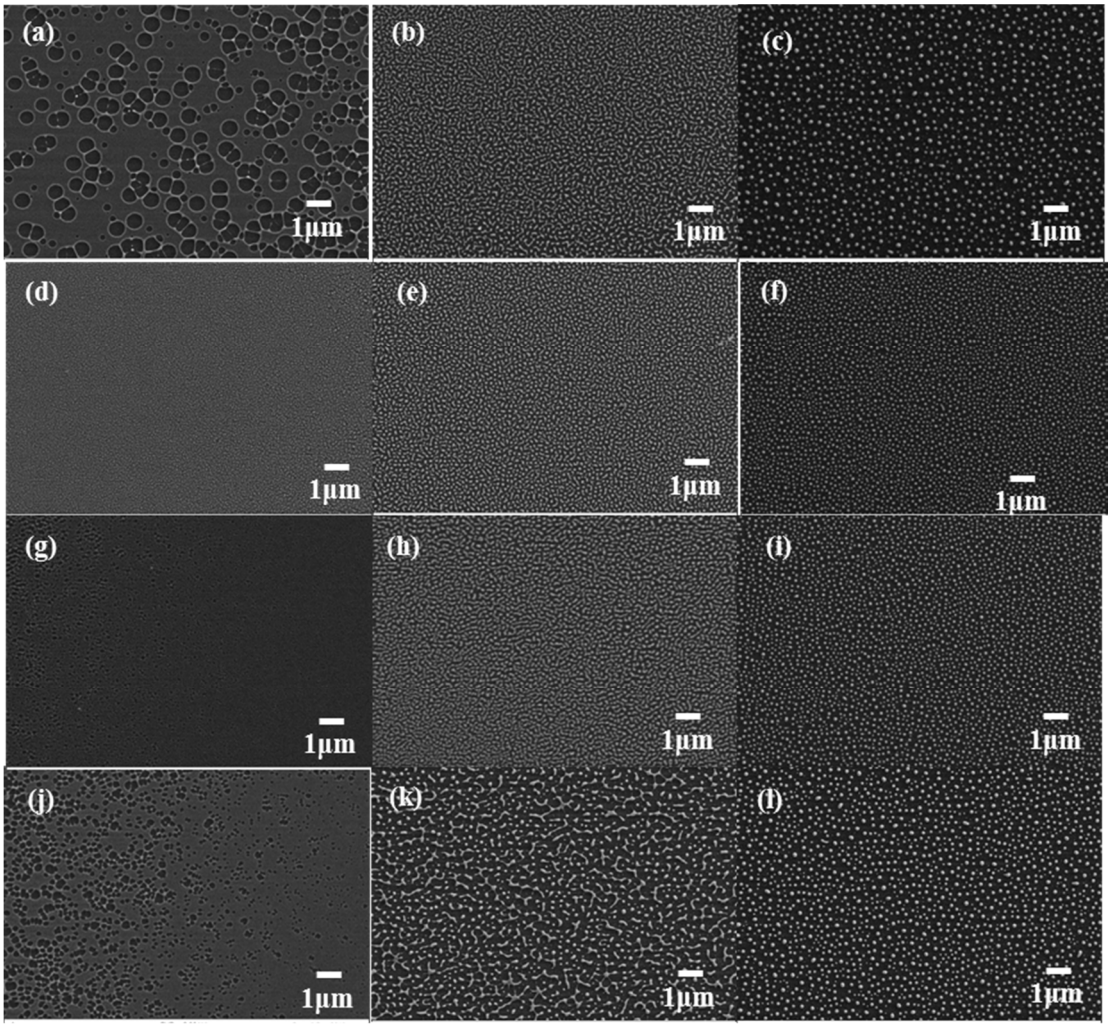

Figure 4.5 (a) – (c): Dewetting pattern evolution of co-sputtered Cu-Co thin films at center position (S3) on SiO_2 substrate with different pulses. (d) – (f): Dewetting pattern evolution of Co top Cu bottom structured Cu-Co thin films at center position on SiO_2 substrate with different pulses. (g) – (i): Dewetting pattern evolution of Cu top Co bottom structured Cu-Co thin films at center position on SiO_2 substrate with different pulses. (j)-(l): Dewetting pattern evolution of co-sputtered Cu-Co thin films at position S4.

Figure 4.5 (a)-(c), (d)-(f), (g)-(i) and (j)-(l) are the dewetting patterns evolution of an around 10 nm Cu-Co thin films with structure co-sputter, Co top Cu bottom and Cu top Co bottom respectively. For each group of images, the laser pulses were increasing from left to right, consequently the energy was also increasing and the total liquid lifetime. At the initial stage of dewetting, as shown in (a) (d) (g) and (j), thin films broke up into holes because of the surface perturbations. The holes grow and form intermediate patterns due to the coalescence of rims from adjacent holes. Eventually, the intermediate patterns decay into particles.

From the particles size distribution in Figure 3.7-3.9, we can observe that the

uniformity of Cu-Co alloy particles with Co top Cu bottom structure (Figure 3.8) is much better than that with other two structures (Figure 3.7 and Figure 3.9). Even though the structure is same, the distribution is still not same at different position if we compare the five histograms in each figure. The atomic concentration was quite different at each position which was well confirmed by EDS results in Table 3.1 and 3.3. That means the composition affects the particle distribution as well. According to these observations, it is suspected that both thin film structure and element composition can affect the particles distribution.

As mentioned in introduction section, the main difference between spinodal process and others is the characteristic wavelength Λ:

$$\Lambda(\mathrm{h}) = \sqrt{\frac{16\pi^3\gamma}{A}}h^2 \qquad (4.2)$$

Where γ is the surface tension of the metal, h is film thickness, A is the Hamaker constant. By considering the dewetting pattern evolution and final particles distribution of Cu-Co alloy thin films, it is expected that thin films studies in this work follow the spinodal dewetting mechanism, but the length scale is modified by alloy composition and film structure. In our alloy system, Co has a larger Hamaker constant than Cu [2]. Thus, the characteristic wavelength of Co should be bigger according to equation 4.2. However, it's hard to determine the trend of particles size along the substrate since the film thickness may vary slightly at different positions. This is also revealed in Figure 3.10 and 3.20.

Additionally, in Figure 4.5, the SEM image of Co top Cu bottom (d) and Cu top Co bottom (g) structured alloy films do not show an obvious perturbation wave on the surface of alloy thin films compared with the large holes shown in image (a) of co-sputtered films. Although, the film structure is same, there is no guarantee that the dewetting evolution is similar which is demonstrated in images (a) and (j). These two were from co-sputtered Cu-Co sample, but with different alloy concentration.

Therefore, it is a possible method to tune dewetting patterns by adjusting alloy composition and film structure owing to the different dewetting evolution and particle distribution of Cu-Co alloy films.

4.5 Optical properties of alloy films as a function of structure and composition

Surface plasmon resonance (SPR) is the collective oscillation of electrons stimulated by incident light. SPR is established when frequency of photons matches the frequency of surface electrons. If this happens in nano-materials, it is called localized surface plasmon resonance. The electromagnetic properties of metal particles have been known for a long time, but it is still attractive because of the development of

new fabrication techniques and wide applications, such as sensors, solar cells and some medical applications [71-74].

Au and Ag are commonly used metals which support the plasmon resonance based on both theory and experiment. Cu also shows the surface plasmon resonance, even though it's not as strong as Au and Ag and because of its oxidation. The optical properties of both pure Cu and Cu-Co alloy particles demonstrate the SPR phenomenon of Cu.

With the aim of investigating the optical properties of the Cu-Co system, a series of optical measurement were carried out on the alloy films deposited on quartz substrate with different element composition and structure before and after pulsed laser treatment. Figure 3.34 – Figure 3.36 present a relatively flat reflectance for Cu-Co alloy thin films. And the absorbance and transmittance graphs (Figure 3.37 – Figure 3.42) do not show any plasmon resonance regardless of the composition or film structure. Contrary to thin films, an absorbance peak shows up on Cu-Co alloy particles after laser irradiation. However, a relatively strong SPR at certain wavelength (~600 nm) only exists in Co top Cu bottom structured nanoparticles while there is no significant resonance for particles with other structures. When the wavelength is longer than the SPR position, the absorbance damped rapidly since it only happens at the resonance wavelength. Whereas, SPR only exist at position S1 and S2 on Co top Cu bottom structured sample. It disappears with increasing Co concentration. Therefore, both film structure and element composition have an effect on the SPR phenomenon of Cu-Co particles.

Several works reported that alloys (particularly solid solutions) typically have one single SPR absorption peak that is located between the two individual resonance peaks of each element, and the peak position is related to the elements and their relative composition [75, 76]. Figure 3.27 – Figure 3.32 suggest that the resonance wavelength of pure Cu particle is around 760 nm while the resonance wavelength is tuned to ~600 nm at position S1 and S2 on Co top Cu bottom sample. This blue shift of can be contributed to mixture of Cu and Co. Moreover, the disappearance of SPR is due to the decrease of Cu concentration. Therefore, the SPR wavelength of Cu-Co alloy particles is tunable by adjusting alloy composition or film structure. Additionally, further study is valuable on this alloy system since a whole range of possibilities exist for tuning of surface plasmon such as particles size, shape, and refractive index of the surrounding medium.

CHAPTER 5 CONCLUSIONS

Cu-Co alloy nanoparticles were fabricated via pulsed laser dewetting. The films composition, particle distribution and optical properties were studies as a function of film structure and element composition.

We observe that there is no preferential evaporation during the dewetting process. The thin film and nano-particle compositions varies as predicted across the substrate and a Cu composition range of 10-70 at.% was realized.

It demonstrated that thin film dewetting patterns can be affected by film structure. Furthermore, film structure and element composition also affects the particle size distribution. Therefore, it is possible to tune dewetting patterns by adjusting alloy composition and film structure owing to the different dewetting evolution and particles distribution of Cu-Co alloy films.

By comparing the optical properties of Cu-Co thin films and particles with three structures with different element concentration, SPR phenomenon shows up in particles. However this SPR only exists in Co top Cu bottom structured particles obviously. And it is damped by Co concentration. Thus, the resonance wavelength is adjustable by controlling film structure or element composition.

REFERENCES

1. Favazza, C., R. Kalyanaraman, and R. Sureshkumar, *Robust nanopatterning by laser-induced dewetting of metal nanofilms.* Nanotechnology, 2006. **17**(16): p. 4229-4234.
2. Krishna, H., et al., *Thickness-dependent spontaneous dewetting morphology of ultrathin Ag films.* Nanotechnology, 2010. **21**(15).
3. Yadavali, S., H. Krishna, and R. Kalyanaraman, *Morphology transitions in bilayer spinodal dewetting systems.* Physical Review B, 2012. **85**(23).
4. Teichert, C., et al., *Stress-induced self-organization of nanoscale structures in SiGe/Si multilayer films.* Physical Review B, 1996. **53**(24): p. 16334-16337.
5. Seemann, R., S. Herminghaus, and K. Jacobs, *Shape of a liquid front upon dewetting (vol 87, art. no. 196101, 2001).* Physical Review Letters, 2001. **87**(24).
6. Bischof, J., et al., *Dewetting modes of thin metallic films: Nucleation of holes and spinodal dewetting.* Physical Review Letters, 1996. **77**(8): p. 1536-1539.
7. Herminghaus, S., et al., *Spinodal dewetting in liquid crystal and liquid metal films.* Science, 1998. **282**(5390): p. 916-919.
8. Reiter, G., *Unstable Thin Polymer-Films - Rupture and Dewetting Processes.* Langmuir, 1993. **9**(5): p. 1344-1351.
9. Singh, S.P., *Spinodal Theory: A Common Rupturing Mechanism in Spinodal Dewetting and Surface Directed Phase Separation (Some Technological Aspects: Spatial Correlations and the Significance of Dipole-Quadrupole Interaction in Spinodal Dewetting).* Advances in Condensed Matter Physics, 2011.
10. Seemann, R., S. Herminghaus, and K. Jacobs, *Gaining control of pattern formation of dewetting liquid films.* Journal of Physics-Condensed Matter, 2001. **13**(21): p. 4925-4938.
11. Diez, J.A., A.G. Gonzalez, and L. Kondic, *On the breakup of fluid rivulets.* Physics of Fluids, 2009. **21**(8).
12. Herminghaus, S., R. Seemann, and K. Landfester, *Polymer surface melting mediated by capillary waves.* Physical Review Letters, 2004. **93**(1).
13. Trice, J., et al., *Novel self-organization mechanism in ultrathin liquid films: Theory and experiment.* Physical Review Letters, 2008. **101**(1).
14. Brada, M.P. and D.R. Clarke, *A thermodynamic approach to the wetting and dewetting of grain boundaries.* Acta Materialia, 1997. **45**(6): p. 2501-2508.
15. Ruffino, F., et al., *Novel approach to the fabrication of Au/silica core-shell nanostructures based on nanosecond laser irradiation of thin Au films on Si.* Nanotechnology, 2012. **23**(4).
16. Matar, O.K., R.V. Craster, and K. Sefiane, *Dynamic spreading of droplets containing nanoparticles.* Physical Review E, 2007. **76**(5).
17. Seemann, R., S. Herminghaus, and K. Jacobs, *Shape of a liquid front upon dewetting - art.no. 196101.* Physical Review Letters, 2001. **87**(19).
18. Song, M. and G. Tryggvason, *The formation of thick borders on an initially stationary fluid sheet.* Physics of Fluids, 1999. **11**(9): p. 2487-2493.
19. Sunderhauf, G., H. Raszillier, and F. Durst, *The retraction of the edge of a planar liquid sheet.* Physics of Fluids, 2002. **14**(1): p. 198-208.
20. Boulogne, F., et al., *Suppression of the Rayleigh-Plateau instability on a vertical fibre coated with wormlike micelle solutions.* Soft Matter, 2013. **9**(32): p. 7787-7796.
21. Al Riyabi, A., M. Boutat, and S. Hilout, *On the Rayleigh-Plateau instability.* Applied Mathematics-a Journal of Chinese Universities Series B, 2012. **27**(2): p. 127-138.

22. Geschiere, S.D., et al., *Slow growth of the Rayleigh-Plateau instability in aqueous two phase systems.* Biomicrofluidics, 2012. **6**(2).
23. Fowlkes, J., et al., *Signatures of the Rayleigh-Plateau Instability Revealed by Imposing Synthetic Perturbations on Nanometer-Sized Liquid Metals on Substrates.* Angewandte Chemie-International Edition, 2012. **51**(35): p. 8768-8772.
24. Prado, G., Y. Amarouchene, and H. Kellay, *Experimental Evidence of a Rayleigh-Plateau Instability in Free Falling Granular Jets.* Physical Review Letters, 2011. **106**(19).
25. Thaokar, R.M., *Effect of counterions on the Rayleigh-Plateau instability of a charged cylinder.* European Physical Journal E, 2010. **31**(3): p. 315-325.
26. Miyamoto, U., *Curvature driven diffusion, Rayleigh-Plateau instability, and Gregory-Laflamme instability.* Physical Review D, 2008. **78**(2).
27. Kamal, S.S.K., et al., *Chemical synthesis of Co/Cu core/shell nanocomposites and evaluation of their magnetic properties.* Materials Science and Engineering B-Advanced Functional Solid-State Materials, 2012. **177**(14): p. 1200-1206.
28. Muzikansky, A., et al., *Ag Dewetting in Cu@Ag Monodisperse Core-Shell Nanoparticles.* Journal of Physical Chemistry C, 2013. **117**(6): p. 3093-3100.
29. Fratoddi, I., et al., *Core shell hybrids based on noble metal nanoparticles and conjugated polymers: synthesis and characterization.* Nanoscale Research Letters, 2011. **6**.
30. Rocha, A.L., I.G. Solrzano, and J.B.V. Sande, *Heterogeneous and homogeneous nanoscale precipitation in dilute Cu-Co alloys.* Materials Science & Engineering C-Biomimetic and Supramolecular Systems, 2007. **27**(5-8): p. 1215-1221.
31. Aizawa, T. and C. Zhou, *Nanogranulation process into magneto-resistant Co-Cu alloy on the route of bulk mechanical alloying.* Materials Science and Engineering a-Structural Materials Properties Microstructure and Processing, 2000. **285**(1-2): p. 1-7.
32. Gomez, E., et al., *Characterisation of cobalt/copper multilayers obtained by electrodeposition.* Surface & Coatings Technology, 2002. **153**(2-3): p. 261-266.
33. Tochitskii, T.A., et al., *Fine structure and possible growth mechanisms of some electrodeposited CuCo granular films.* Journal of Magnetism and Magnetic Materials, 2001. **224**(3): p. 221-232.
34. Correia, J.B. and H.A. Davies, *Magnetic and structural monitoring of nanophase precipitation during ageing of water-atomised Cu-5% Co alloy powders.* Acta Materialia, 2000. **48**(16): p. 4115-4123.
35. Bisero, D., et al., *Effects of atomic diffusion processes in Co-Cu multilayer granular films.* Nanostructured Materials, 1999. **11**(6): p. 769-774.
36. Dubiel, B., D. Wolf, and A. Czyrska-Filemonowicz, *TEM and electron holography analyses of granular and thin layered Cu-Co magnetic materials.* Ultramicroscopy, 2010. **110**(5): p. 433-437.
37. Straumal, B.B., et al., *SPb-induced changes of structure and magnetic properties in the Cu-Co alloys.* Materials Letters, 2013. **98**: p. 217-221.
38. Yang, G.Y., et al., *Precipitation of nanoscale Co particles in a granular Cu-Co alloy with giant magnetoresistance.* Materials Research Bulletin, 2000. **35**(6): p. 875-885.
39. Egry, I., et al., *Surface Tension, Phase Separation and Solidification of Undercooled Cu-Co.* Microgravity Science and Technology, 2005. **16**(1-4): p. 50-54.
40. Biziere, N., C. Fermon, and G. Le Goff, *Hyper frequency behavior of the GMR effect in a*

single spin valve sensor. Journal of Magnetism and Magnetic Materials, 2007. **316**(2): p. 340-343.

41. Pattanaik, G.R., D.K. Pandya, and S.C. Kashyap, *Effect of process parameters on GMR in electrodeposited Cu-Co nanogranular thin films.* Thin Solid Films, 2003. **433**(1-2): p. 247-251.
42. Kuzminski, M., et al., *The effect of particle size and surface-to-volume ratio distribution on giant magnetoresistance (GMR) in melt-spun Cu-Co alloys.* Journal of Magnetism and Magnetic Materials, 1999. **205**(1): p. 7-13.
43. Wen, M., et al., *Positive microemulsion synthesis and magnetic property of amorphous multicomponent Co-, Ni- and Cu-based alloy nanoparticles.* Colloids and Surfaces a-Physicochemical and Engineering Aspects, 2008. **318**(1-3): p. 238-244.
44. Miranda, M.G.M., et al., *Spinodal decomposition and giant magnetoresistance.* Physica B-Condensed Matter, 2006. **384**(1-2): p. 175-178.
45. Hutten, A. and G. Thomas, *Investigation of Heterogeneous Cu1-Xcox Alloys with Giant Magnetoresistance.* Ultramicroscopy, 1993. **52**(3-4): p. 581-590.
46. Sugawara, T., K. Takanashi, and H. Fujimori, *Appearance of GMR on annealing in Cu-Co granular alloys with high Co concentration.* Journal of Magnetism and Magnetic Materials, 1998. **177**: p. 951-952.
47. Miyazaki, K., et al., *Giant magnetoresistance in Co-Cu granular alloy films and nanowires prepared by pulsed-electrodeposition.* Electrochimica Acta, 1999. **44**(21-22): p. 3713-3719.
48. Hutten, A. and K.H. Muller, *Giant magnetoresistance in bulk materials.* Sensors and Actuators a-Physical, 1997. **59**(1-3): p. 236-242.
49. Kolbe, M., et al., *Undercooling and demixing of copper-based alloys.* Microgravity Science and Technology, 2006. **18**(3-4): p. 174-177.
50. Battezzati, L., et al., *Undercooling and demixing in rapidly solidified Cu-Co alloys.* Materials Science and Engineering a-Structural Materials Properties Microstructure and Processing, 2007. **449**: p. 7-11.
51. You, C.Y., et al., *Structural and magnetic characterization of Co-Cu nanoparticles prepared by arc-discharge.* European Physical Journal-Applied Physics, 2004. **28**(1): p. 73-77.
52. Guevara, J., A.M. Llois, and M. Weissmann, *Large variations in the magnetization of Co clusters induced by noble-metal coating.* Physical Review Letters, 1998. **81**(24): p. 5306-5309.
53. Liddle, J.A., Y. Cui, and P. Alivisatos, *Lithographically directed self-assembly of nanostructures.* Journal of Vacuum Science & Technology B, 2004. **22**(6): p. 3409-3414.
54. Kalyanaraman, S.Y.R., *Fabricating Metal Nanostructures with Pulsed Laser Dewetting Self-Assembly.* Advanced Materials & Processes, 2013. **171**(7): p. 22-26.
55. Anton, R.L., et al., *Synthesis and characterisation of electrodeposited Cu90Co10 thin film.* Journal of Magnetism and Magnetic Materials, 2003. **254**: p. 85-87.
56. Kim, N.H., J. Peck, and J.Q. Wang, *Anomalous magnetic nanostructural evolution in annealed CuCo granular thin films.* Applied Physics Letters, 2006. **88**(22).
57. Allia, P., et al., *Magnetic hysteresis in granular CuCo alloys.* Journal of Applied Physics, 1999. **85**(8): p. 4343-4345.
58. Sun, G.B., et al., *Controlled synthesis of nanorods/nanorings of a novel Co-Cu complex in microemulsion at room temperature.* Chemical Communications, 2005(13): p. 1740-1742.

59. Du, Y.S., et al., *One-step synthesis of magnetically recyclable rGO supported Cu@Co core-shell nanoparticles: highly efficient catalysts for hydrolytic dehydrogenation of ammonia borane and methylamine borane.* New Journal of Chemistry, 2013. **37**(10): p. 3035-3042.
60. Elkalkouli, R., R. Morel, and J.F. Dinhut, *Microstructure and magnetic hysteresis of Co80Cu20 mechanically alloyed powders.* Nanostructured Materials, 1997. **8**(3): p. 313-320.
61. Yadavali, S., M. Khenner, and R. Kalyanaraman, *Pulsed laser dewetting of Au films: Experiments and modeling of nanoscale behavior.* Journal of Materials Research, 2013. **28**(13): p. 1715-1723.
62. Qi, Y., L. Wang, and T. Fang, *Demixing behaviour in binary Cu-Co melt.* Physics and Chemistry of Liquids, 2013. **51**(6): p. 687-694.
63. Egry, I., et al., *Surface tension, phase separation, and solidification of undercooled cobalt-copper alloys.* Advanced Engineering Materials, 2003. **5**(11): p. 819-823.
64. Turchanin, M.A., et al., *Mixing Enthalpies of Liquid Alloys and Thermodynamic Assessment of the Cu-Fe-Co System.* Powder Metallurgy and Metal Ceramics, 2011. **50**(1-2): p. 98-116.
65. Straumal, B.B., et al., *Contact angles by the solid-phase grain boundary wetting (coverage) in the Co-Cu system.* Journal of Materials Science, 2010. **45**(16): p. 4271-4275.
66. Diaz-Barriga-Arceo, L., et al., *Martensitic transformation in nanostructured Cu-Co alloys.* Journal of Materials Science Letters, 2001. **20**(24): p. 2239-2241.
67. Gartley, S.K.G.a.M.G., *XRD and VSM Analysis of Nanostructured Cu-Co Alloys.* JCPDS-International Centre for Diffraction Data, 1999: p. 10.
68. Sedky, S., et al., *Microencapsulation of silicon cavities using a pulsed excimer laser.* Journal of Micromechanics and Microengineering, 2012. **22**(7).
69. Nahm, C., et al., *A simple template-free 'sputtering deposition and selective etching' process for nanoporous thin films and its application to dye-sensitized solar cells.* Nanotechnology, 2013. **24**(36).
70. Fowlkes, J.D., J.M. Fitz-Gerald, and P.D. Rack, *Ultraviolet emitting (Y1-xGdx)(2)O3-delta thin films deposited by radio frequency magnetron sputtering; structure-property-thin film processing relationships.* Thin Solid Films, 2007. **515**(7-8): p. 3488-3498.
71. Spinelli, P., et al., *Plasmonic light trapping in thin-film Si solar cells.* Journal of Optics, 2012. **14**(2).
72. Pillai, S., et al., *Surface plasmon enhanced silicon solar cells.* Journal of Applied Physics, 2007. **101**(9).
73. Chantana, J., et al., *Localized surface plasmon enhanced microcrystalline-silicon solar cells.* Journal of Non-Crystalline Solids, 2012. **358**(17): p. 2319-2323.
74. Atwater, H.A. and A. Polman, *Plasmonics for improved photovoltaic devices (vol 9, pg 205, 2010).* Nature Materials, 2010. **9**(10): p. 865-865.
75. Zhang, J.H., et al., *Preparation and optical properties of silica@Ag-Cu alloy core-shell composite colloids.* Journal of Solid State Chemistry, 2007. **180**(4): p. 1291-1297.
76. Magruder, R.H., J.E. Wittig, and R.A. Zuhr, *Wavelength Tunability of the Surface-Plasmon Resonance of Nanosize Metal Colloids in Glass.* Journal of Non-Crystalline Solids, 1993. **163**(2): p. 162-168.

VITA

Shaofang Fu was born in Shandong, China on September 27, 1988. She graduated from Zhaoyuan No. 1 Middle School in Shandong Province in 2007 and entered the Materials Chemistry program at Wuhan University of Technology, Hubei at the same year. She obtained her Bachelor's Degree in 2011. She joined Professor Philip Rack's group in Department of Materials Science and Engineering at the University of Tennessee, Knoxville in August 2011.